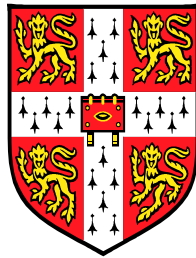


# **SPIN POLARISED TUNNEL JUNCTIONS BASED ON HALF-METALLIC MANGANITES**

Moon-Ho Jo

Downing College

Cambridge



A Dissertation Submitted for the Doctor of Philosophy Degree  
at University of Cambridge

August  
2001

## Abstract

This dissertation describes an experimental study on spin polarised tunnel (SPT) junctions based on mixed valence manganites,  $\text{La}_{1-x}\text{Ca}_x\text{MnO}_3$  ( $0 < x < 1$ ).

The interfacial magnetism of  $\text{La}_{0.7}\text{Ca}_{0.3}\text{MnO}_3$  (LCMO) was initially investigated with heteroepitaxial LCMO/SrTiO<sub>3</sub> multilayers. This work had implications for barrier optimization in SPT junctions: it suggested a strong electron-lattice coupling and inhomogeneous interfacial magnetic order due to significant lattice-mismatch. The coherent growth of LCMO on lattice-matched NdGaO<sub>3</sub> demonstrated perfect layer-by-layer growth and the films exhibit a weaker electron-lattice coupling showing the bulk LCMO-like behavior.

The SPT devices incorporating the NdGaO<sub>3</sub> barrier showed an unprecedentedly high tunnel magnetoresistance {TMR,  $(R_{\text{ap}}-R_{\text{p}})/R_{\text{ap}}$ } of 86% at 77K, and coherent switching. The electronic polarisation deduced from the TMR at 77K was higher than the directly measured value at 4.2K. However it was observed that the TMR decays rapidly at high temperatures. It was suggested that an active tunnelling mechanism based on percolative phase separation could account for the temperature dependence of the TMR and the high spin polarisation of LCMO.

Another type of all-manganites SPT junction, LCMO/ $\text{La}_{0.45}\text{Ca}_{0.55}\text{MnO}_3$ /LCMO was also studied, where the ground state of the  $\text{La}_{0.45}\text{Ca}_{0.55}\text{MnO}_3$  barrier is an antiferromagnetic insulator. Although the junction conductance is likely to be influenced by the potential coexistence of mesoscopic metallic and insulating phases in the  $\text{La}_{0.45}\text{Ca}_{0.55}\text{MnO}_3$ , the TMR of the device shows a maximum of 16.7%, with coherent switching at low temperatures. Interestingly, the TMR persists up to a relatively higher temperature ( $T/T_{\text{C}} \leq 0.75$ ) compared with equivalent non-manganite NdGaO<sub>3</sub> barrier junctions ( $T/T_{\text{C}} \leq 0.5$ ). A systematic investigation of interface magnetism such as asymmetric magnetization reversal and enhanced coercivity reveals the existence of a magnetic coupling at the LCMO/ $\text{La}_{0.45}\text{Ca}_{0.55}\text{MnO}_3$  interface, which serves to increase the stability of the interfacial magnetic order in the LCMO electrodes.

Lastly, magnetization reversal processes in the SPT junctions were studied by two-dimensional angular SPT measurements. The highly sensitive TMR of the present junctions to local magnetic fluctuations in the LCMO establishes a one-to-one correlation between magnetization reversal and SPT. The observed coherent magnetization reversal was assessed using the Stoner-Wohlfarth's coherent rotation model. The systematic angular variations of the observed SPT features in the resistance-field curves reveals other important information about magnetization reversal and edge-domain pinning is suggested to play a crucial role in the magnetization reversal

## Preface

This dissertation is submitted for the degree of Doctor of Philosophy in the University of Cambridge. Except where specific reference is made, this work is entirely the result of my own work and includes nothing that is the outcome of work done in collaboration. No part of this work has been or is being submitted for any other qualification at this or any other university. This dissertation does not exceed the limit of length.

Some of the work contained in this dissertation has been published and presented as listed below.

## Publications

- "Inhomogeneous transport in heteroepitaxial  $\text{La}_{0.7}\text{Ca}_{0.3}\text{MnO}_3/\text{SrTiO}_3$  multilayers",  
Moon-Ho Jo, N.D. Mathur, J.E. Evetts, M.G. Blamire, M. Bibes and J. Fontcuberta,  
*Appl. Phys. Lett.* **75**, 3689 (1999).
- "Magnetotransport and interface magnetism in manganite heterostructures: implications for spin polarized tunneling",  
Moon-Ho Jo, N.D. Mathur, J.E. Evetts and M.G. Blamire,  
*Mater. Res. Soc. Symp. Proc.* **602**, 3 (1999).
- "Very large magnetoresistance and coherent switching in half-metallic manganite tunnel junctions",  
Moon-Ho Jo, N.D. Mathur, N.K. Todd and M.G. Blamire,  
*Phys. Rev. B. (Rapid Communications)* **61**, R14905 (2000).
- "Coherent magnetic reversal in half metallic manganites tunnel junctions",  
Moon-Ho Jo, N.D. Mathur, J.E. Evetts and M.G. Blamire,  
*Appl. Phys. Lett.* **77**, 3803 (2000).
- "Spin and charge modulated magnetic tunnel junction:  $\text{La}_{0.7}\text{Ca}_{0.3}\text{MnO}_3/\text{La}_{0.45}\text{Ca}_{0.55}\text{MnO}_3/\text{La}_{0.7}\text{Ca}_{0.3}\text{MnO}_3$ ",  
Moon-Ho Jo, N.D. Mathur and M.G. Blamire, D. Ozkaya and A. K. Petford-Long,  
*Phys. Rev. B.*, (in publication).
- "Magnetization reversal probed by spin-polarized tunneling",  
Moon-Ho Jo, N.D. Mathur and M.G. Blamire,  
*Appl. Phys. Lett.*, (to be published)

- "Magnetic anisotropy of thin film  $\text{La}_{0.7}\text{Ca}_{0.3}\text{MnO}_3$  on untwinned paramagnetic  $\text{NdGaO}_3$  (001)",  
N.D. Mathur, Moon-Ho Jo, J.E. Evetts and M.G. Blamire,  
*J. Appl. Phys.* **89**, 338 (2001).
- "Structure and chemistry of manganite based tunnel junctions",  
D. Ozkaya, A. K. Petford-Long, Moon-Ho Jo and M. G. Blamire,  
*J. Appl. Phys.* **89**, 6757 (2001).

## Presentations

- '99 OXSEN (OXide Spin Electronics Network) Meeting (Barcelona, Spain, 1999):  
"La<sub>0.7</sub>Ca<sub>0.3</sub>MnO<sub>3</sub>/SrTiO<sub>3</sub> multilayers: strain and transport",  
Moon-Ho Jo, N.D. Mathur, J.E. Evetts and M.G. Blamire
- '99 Materials Research Society Fall Meeting (Boston, USA, 1999) in Session JJ:  
"Magnetotransport and interface magnetism in manganite heterostructures: implications for spin polarized tunneling",  
Moon-Ho Jo, N.D. Mathur, N.K. Todd, J.E. Evetts and M.G. Blamire
- Workshop on Strongly Correlated Electron Systems: Physics and Chemistry of Colossal Magnetoresistance (Isaac Newton Institute for Mathematical Sciences, Cambridge, 2000):  
"Spin polarised tunnelling in the CMR manganites",  
Moon-Ho Jo and M.G. Blamire
- 2000 Symposium on Spin-Electronics (Max Planck Institute of Microstructure Physics, Halle, Germany, 2000):  
"Lattice and charge engineered magnetic tunnel junctions with half metallic manganites",  
Moon-Ho Jo, N.D. Mathur, N.K. Todd and M.G. Blamire
- The Annual March Meeting 2001 of The American Physical Society (Seattle, USA, 2001):  
"Charge modulated trilayer-magnetic-junction:  $\text{La}_{0.7}\text{Ca}_{0.3}\text{MnO}_3/\text{La}_{0.45}\text{Ca}_{0.55}\text{MnO}_3/\text{La}_{0.7}\text{Ca}_{0.3}\text{MnO}_3$ ",  
Moon-Ho Jo, N.D. Mathur, M.G. Blamire, D. Ozkaya and A. K. Petford-Long.

## Moon-Ho Jo

Device Materials Group, Department of Materials Science, University of Cambridge,  
August 2001.

## Acknowledgements

I have benefited from a number of people during the study towards this dissertation. I must first thank my supervisor, Mark Blamire for his unwavering support and encouragements for me to carry out the project through the years in Cambridge. I have always enjoyed the inspiring discussion with him and his daily mentoring helped me in many critical stages of the project. I thank the head of the Device Materials Group, Jan Evetts, who always amazed me with his deep insights for material physics. Special thanks go to Neil Mathur who has been sharing the enthusiasm on manganite physics with me through invaluable discussions. He also patiently proofread several chapters of this dissertation. I also thank Zoe Barber, Bartek Glowacki and Ed Tarte and Nadia Stelmashenko for their helpful advice with their expertise. I thank Pak-Kin Wong for his advice on device fabrication in the early stage of the project. Thanks are also extended to Neil Todd and Gavin Burnell for their endeavoring contribution to the device measurement set-ups. Dae-Joon Kang deserves particular thanks for the stimulating discussion on various device issues. Outside the Group, I thank Dogan Ozkaya and Amanda Petford-Long at University of Oxford for their TEM works on my samples.

I thank my office-mates, Mike Hogg, Yee-Siau Cheng, Cliff Elwell and Ashish Garg who helped me to survive both the highs and lows of the last few years. I also acknowledge other colleagues in the Group who have enriched my life in Cambridge by listing their names, but in no particular order; Bernard Zeimetz, Jose Prieto, Robert Hadfields, Rachael Speaks, James Ransley, Dennis Leung, Debbie Morecroft, Maria Glew, Chris Bell, Davis Ansell, James Loudon and Brian Pang as well as the former Group members, Wilfred Booi, Richard Moseley, Robert Kinsey, Phil McBrien, Noel Rutter and John Durrell.

Finally, but not in the least, my sincere thanks go to my family for their unreserved support. Particularly, I express my utmost gratitude to my mother, Un-Hee Jung and my wife, Ji-Wan Ha for their unconditional love and support throughout the years.

I have been supported financially by grants from the Engineering and Physical Sciences Research Council and the Cambridge Overseas Trust.

**For my mother  
and  
my wife**

# Contents

<b>Abstract</b> .....	ii
<b>Preface</b> .....	iii
<b>Acknowledgements</b> .....	v
<b>Chapter 1</b>	
<b>Introduction</b> .....	1
1.1 Magneto-electronics (Spintronics) .....	2
1.2 Magnetoresistance .....	3
1.3 Overview of the Dissertation .....	7
<b>Chapter 2</b>	
<b>Background reviews</b> .....	9
2.1 Spin polarised electron tunnelling .....	10
2.1.1 Quantum mechanical electron tunnelling .....	10
2.1.2 Definitions of spin polarisation .....	14
2.1.3 Spin polarised tunnel junctions .....	17
2.1.4 Experimental aspects of spin polarised tunnelling .....	21
2.1.4.1 Inelastic spin tunnelling .....	21
2.1.4.2 Interfacial band structures .....	25
2.1.5 Spin polarised tunnelling based on half-metallic manganites .....	28
2.2 Half-metallic manganites .....	35
2.2.1 Historical background .....	35
2.2.2 Interplay among the electronic, magnetic and crystal structures .....	37
2.2.2.1 Crystal and electronic structures .....	37
2.2.2.2 Electron-electron interactions and Magnetism .....	39
2.2.2.3 Electron-lattice interaction .....	40
2.2.3 Narrow bandwidth manganite: $\text{La}_{1-x}\text{Ca}_x\text{MnO}_3$ .....	45
2.2.4 Half-metallicity in manganites .....	47
2.2.5 Multi-phase coexistence .....	50
2.3 Magnetization processes in spin polarised tunnel junctions .....	57
2.3.1 Magnetic energetics (Micromagnetics) .....	57

2.3.2 Magnetic anisotropy .....	58
2.3.2.1 Crystalline anisotropy .....	58
2.3.2.2 Induced anisotropy .....	59
2.3.3 Domains and domain walls .....	62
2.3.4 Magnetization reversal of a single domain: Coherent rotation.....	63

### **CHAPTER 3**

<b>Experimental methods .....</b>	<b>68</b>
3.1 Deposition of heteroepitaxial structure .....	68
3.2 Device microfabrication .....	71
3.3 Characterizations and Measurements .....	74
3.3.1 Structural characterization .....	74
3.3.2 Magnetic measurements .....	77
3.3.3 Electrical transport measurements .....	77

### **CHAPTER 4**

<b>Interfacial magnetism in manganite heterostructures: Implication for spin polarised tunnelling.....</b>	<b>81</b>
4.1 Motivations.....	82
4.2 Lattice-mismatched heteroepitaxial $\text{La}_{0.7}\text{Ca}_{0.3}\text{MnO}_3/\text{SrTiO}_3$ multilayers .....	82
4.3 Inhomogeneous transport of $\text{La}_{0.7}\text{Ca}_{0.3}\text{MnO}_3$ .....	84
4.4 Interfacial magnetism in $\text{La}_{0.7}\text{Ca}_{0.3}\text{MnO}_3/\text{SrTiO}_3$ multilayers .....	86
4.5 Lattice-matched heteroepitaxy with $\text{NdGaO}_3$ .....	89

### **CHAPTER 5**

<b>Lattice engineered <math>\text{La}_{0.7}\text{Ca}_{0.3}\text{MnO}_3/\text{NdGaO}_3/\text{La}_{0.7}\text{Ca}_{0.3}\text{MnO}_3</math> tunnel junctions .....</b>	<b>95</b>
5.1 Motivations .....	96
5.2 Lattice engineered $\text{La}_{0.7}\text{Ca}_{0.3}\text{MnO}_3/\text{NdGaO}_3/\text{La}_{0.7}\text{Ca}_{0.3}\text{MnO}_3$ .....	96
5.3 Very high magnetoresistance and coherent switching .....	99
5.4 Bias and temperature dependence of the TMR .....	101
5.5 Surface and interface of manganites .....	105
5.6 The role of phase-separation .....	106

## **CHAPTER 6**

<b>Spin and charge modulated <math>\text{La}_{0.7}\text{Ca}_{0.3}\text{MnO}_3/\text{La}_{0.45}\text{Ca}_{0.55}\text{MnO}_3/\text{La}_{0.7}\text{Ca}_{0.3}\text{MnO}_3</math> tunnel junctions</b> .....	<b>111</b>
6.1 Motivations .....	112
6.2 Heteroepitaxy of $\text{La}_{0.7}\text{Ca}_{0.3}\text{MnO}_3/\text{La}_{0.45}\text{Ca}_{0.55}\text{MnO}_3/\text{La}_{0.7}\text{Ca}_{0.3}\text{MnO}_3$ .....	113
6.3 TMR of $\text{La}_{0.7}\text{Ca}_{0.3}\text{MnO}_3/\text{La}_{0.45}\text{Ca}_{0.55}\text{MnO}_3/\text{La}_{0.7}\text{Ca}_{0.3}\text{MnO}_3$ .....	116
6.4 Interfacial magnetism of $\text{La}_{0.7}\text{Ca}_{0.3}\text{MnO}_3/\text{La}_{0.45}\text{Ca}_{0.55}\text{MnO}_3/\text{La}_{0.7}\text{Ca}_{0.3}\text{MnO}_3$ .....	119

## **CHAPTER 7**

<b>Magnetization reversal processes in spin polarised tunnel junctions</b> .....	<b>127</b>
7.1 Introduction .....	128
7.2 Two-dimensional angular TMR measurements .....	129
7.3 Coherent magnetization reversal processes .....	133
7.4 Edge domains pinning effect .....	135

## **CHAPTER 8**

<b>Summary and Outlook</b> .....	<b>144</b>
----------------------------------	------------

---

---

# **CHAPTER 1**

## **Introduction**

---

---

1.1 Magneto-electronics (Spintronics)

1.2 Magnetoresistance

1.3 Overview of the Dissertation

---

## 1.1 Magneto-electronics (Spintronics)

The modern microelectronics has utilized the '*charge*' degree of freedom of an electron by manipulating the collective flow of electronic charges in metals or semiconductors in solid-state devices. The electronic charges in such devices, e.g. in field effect transistors, are controlled with external electric fields. But electrons are also characterized by another quantum parameter of their own, the '*spin*', i.e. the spin angular momentum. The electronic spin confers a magnetic moment on electrons, which can then be manipulated by magnetic fields as well as by electrical fields. The latest discipline of electronics, 'magneto-electronics<sup>1</sup>' or 'spintronics<sup>2</sup>' exploits the spin degree of freedom and attempts to find unique possibilities for use in new functional microelectronic devices.

Manifestations of the electronic spin are most notably found in ferromagnetic metals, where an imbalance of spin populations near the Fermi level is responsible for spin-dependent electrical transport properties, i.e. the charge carriers are net spin-polarised. In fact, the modulation of a spin-polarised current in ferromagnetic metals as a function of magnetic field has received intensive interest both for magneto-electronics applications and because of fundamental physics. More recently magnetoresistive effects in semiconductors, which would be compatible with the existing semiconductor technology, have also been attracting booming interests. Spin manipulation in these magnetic semiconductors could involve not just magnetic fields but also some other types of spin dynamics controlled by polarised light or electric fields.<sup>3,4</sup> This nascent field could open up novel quantum mechanical functionalities such as spin transistors or quantum computers.<sup>5</sup> Nevertheless, up to now, the manipulation of the spin states in such semiconductors is only prototypical, mainly due to low spin injection and detection, and the spin decoherence of the carriers.

The basic principles of magneto-electronic devices rely on a variety of magnetoresistive (MR) effects that come from various physical origins. Historically, MR effects have been discovered in various materials systems and their physical bases have implications for technological developments. Particularly the recent revolutionary inventions of new MR effects have led to intense theoretical and experimental studies of an extraordinary range of solid-state structures, e.g. magnetic multilayers and tunnel junctions. They have also boosted widespread interest in the magnetic storage industry. In the following section, the main features of the various MR effects are selectively reviewed in brief.

---

## 1.2 Magnetoresistance

Magnetoresistance (MR) can be defined by the change of a material's resistivity under the influence of a magnetic field. The MR effects have been discovered in a variety of materials systems, for which various physical origins are responsible. In technological applications, the MR effect has been progressively developed to enlarge its magnitude. Particularly the recent discovery of large magneto-resistance in synthetic solid-state systems has provided the most important impetus to magnetoelectronics.

In the following, a brief overview of the various MR effects, including ordinary MR, anisotropy MR, giant MR, colossal MR and tunnel MR, is given. Their schematic features are compiled in Table 1.1.

### *Ordinary Magnetoresistance (OMR)*

When a magnetic field is applied to a metal or a semiconductor perpendicular to an electrical field, the Lorentz force affects the trajectories of the conduction electrons giving rise to a change of the transverse resistivity,  $\Delta\rho_{\perp}$ . A similar effect is also found when a magnetic field is applied in parallel to the electrical field, i.e. a change of the longitudinal resistivity,  $\Delta\rho_{\parallel}$ . According to the electronic orbital structures at the Fermi surface in a given material, various features in the resistivity - (magnetic) field relations are observed.<sup>6</sup> The change in resistivity in a non-magnetic metal is usually positive, i.e.  $\Delta\rho$  in In, Al and Na is proportional to the magnetic field. The MR effect however is very small at a moderate magnetic field, where  $\{\rho(H)-\rho(0)\}/\rho(0)$  is  $\leq 1\%$  except for in some semiconductors.<sup>7</sup>

### *Anisotropy Magnetoresistance (AMR)*

The resistance of ferromagnetic metals or alloys under a magnetic field is anisotropic and changes according to the relative orientation of the magnetization to the measuring current.<sup>8,9</sup> The resistivity for the current parallel to the magnetic field increases with field, and for the current perpendicular to the field, it decrease with field. The physical origin of this anisotropy magnetoresistance (AMR) can be found in the asymmetric scattering cross-section of the conduction electrons due to the spin-orbit coupling in the magnetic field – see, Table 1-1 (b).

The magnitude of AMR is typically a few percent in low fields (less than a few tens of Oe), i.e.  $\{\rho(H) - \rho(0)\} / \rho(0) \sim 5\%$  at room temperature (RT) for a  $\text{Ni}_{70}\text{Fe}_{30}$  alloy. This moderate MR effect at low field found an application in magnetic read-heads that are commonly available in some computer hard drives today.

### *Giant Magnetoresistance (GMR)*

In 1988, a large magnetoresistance of up to  $\{\rho(H) - \rho(0)\} / \rho(0)$  of  $\sim 50\%$  at 4.2K dubbed giant magnetoresistance (GMR)<sup>10</sup> was discovered by Baibich *et al.* in artificial metallic multilayers, i.e.  $(\text{Fe}/\text{Cr})_n$ , where ferromagnetic Fe layers are antiferromagnetically coupled through the non-magnetic Cr interlayers. In fact the interlayer coupling between magnetic layers can oscillate between ferromagnetic and antiferromagnetic exchange depending on the thickness of the non-magnetic layers (the RKKY-like interaction).<sup>11</sup> This large effect has been subsequently found in other multilayer systems and granular systems, and now an MR of  $>10\%$  can be observed at RT. The physical origin of GMR can be qualitatively understood based on a two spin-currents model where the conduction electrons are divided into two spin sub-systems: those whose spins are parallel to the magnetization and those whose spins are antiparallel. When there is a dissimilar spin scattering rate in the spin sub-channels, the total scattering rate depends on the relative orientation of the magnetization in the ferromagnetic layers, which can be tuned by the external magnetic field – see Table. 1.1(c).

From the applications point of view, the GMR effect is particularly important not only because the effect is substantial but also because it is an extrinsically engineerable effect. Indeed GMR found its way into real technological applications within a decade of its discovery, when IBM introduced a novel read-head based on an advanced GMR device, called “spin valves”, in 1997.

### *Colossal Magnetoresistance (CMR)*

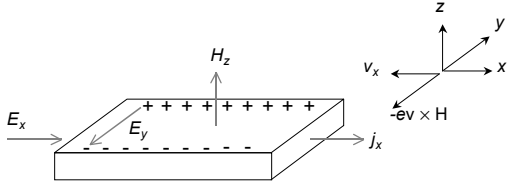
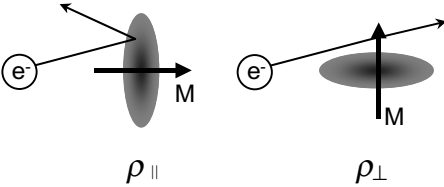
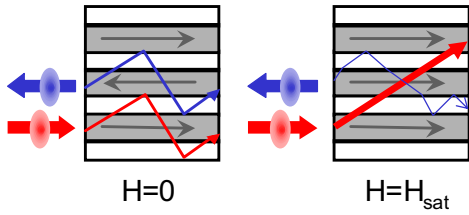
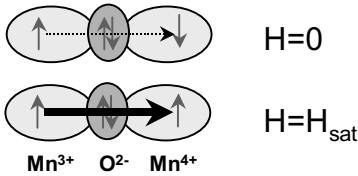
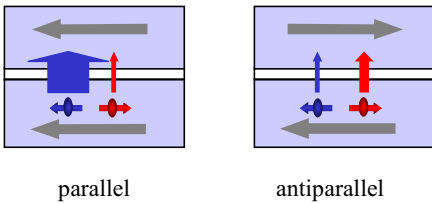
More recently a much larger magnetoresistance effect was discovered in mixed-valence manganites with a perovskite structure,  $\text{Re}_{1-x}\text{Ae}_x\text{MnO}_3$  where *Re* is a rare earth ion and *Ae* is a divalent alkaline. In 1993 von Helmlolt *et al.*<sup>12</sup> observed an  $\{R(7T) - R(0)\} / R(0)$  of 60% at room temperature in  $\text{La}_{0.67}\text{Ba}_{0.33}\text{MnO}_3$  thin films. In the following year, Jin *et al.*<sup>13</sup> reported an MR effect in excess of a million percent at 77K in a  $\text{La}_{0.67}\text{Ca}_{0.33}\text{MnO}_3$  thin film. This was dubbed colossal magnetoresistance (CMR). Later, similar large MR effects were observed in other

complex oxides such as layered perovskites<sup>14</sup>, double perovskites  $\text{Sr}_2\text{FeMoO}_6$ <sup>15</sup> and pyrochlores  $\text{Ti}_2\text{Mn}_2\text{O}_7$ <sup>16,17</sup>. The CMR effect in the  $\text{Re}_{1-x}\text{Ae}_x\text{MnO}_3$  is believed to arise from the close correlation between the magnetic phase transition and the electronic phase transition near the Curie temperature ( $T_C$ ), though the fundamental physics is yet to be understood. Because the CMR effect usually requires a large magnetic field, typically in the range of several Teslas near the  $T_C$ , the imminent technological application of the CMR is largely limited so far. CMR materials are known to possess a uniquely high spin-polarisation of conduction electrons, and this has an important implication in the study of spin-polarised transport, e.g. spin-polarised tunnelling in this dissertation. The main issues related to the CMR effect are further discussed in more detail in the following chapter.

### *Tunnelling magnetoresistance (TMR)*

Tunnelling magnetoresistance (TMR) exploits the quantum mechanical tunnelling process between ferromagnetic metals separated by a thin insulating barrier. The TMR effect can be understood based on the two spin sub-channels model that is used to explain GMR. However it is qualitatively different in that TMR is due to a dissimilar tunnelling conductance between asymmetric spin sub-bands, while GMR is due to the spin-dependent electron scattering during diffusive transport. In principle, the magnitude of TMR is strongly dependent on the degree of asymmetry in the density of states at Fermi level of each spin sub-band, i.e. the spin polarisation of the conduction electrons. Ever since the large TMR of  $\sim 13\%$  at RT was reported in the  $\text{CoFe}/\alpha\text{-Al}_2\text{O}_3/\text{Co}$  junctions by Moodera *et al.*<sup>18</sup> in 1995, TMR performance has become significantly improved and nowadays TMR values of  $\sim 20\%$  at RT are routinely reproduced in advanced device architectures.<sup>19</sup> It is foreseen that a possible practical application in magneto-electronics of the TMR effect is not limited to the recording head industry, but also extends to non-volatile memory elements, i.e. magnetic random access memory (MRAM).<sup>2</sup>

Table 1.1. Schematic features of the various MR effects.

The types of MR	Origins	MR(%) <sup>1)</sup>	(Possible) Applications
<p>OMR</p> 	<p>Lorentz force, Orbital structures (<i>Intrinsic</i>)</p>	<p>&lt;1% (<i>positive MR</i> <i>up to high</i> <i>field</i>)</p>	<p>Field sensors (some semiconductors)</p>
<p>AMR</p> 	<p>Spin-orbit coupling (<i>Intrinsic</i>)</p>	<p>~5% (<i>positive or</i> <i>negative MR</i> <i>at low field</i>)</p>	<p>Read-heads</p>
<p>GMR</p> 	<p>Spin- dependent scattering (<i>Extrinsic</i>)</p>	<p>~10-20% (<i>negative MR</i> <i>at low field</i>)</p>	<p>Read-heads</p>
<p>CMR</p> 	<p>Double exchange and Jahn-Teller effect (<i>Intrinsic</i>)</p>	<p>~10<sup>6</sup>% (<i>negative MR</i> <i>at high field</i>)</p>	<p>Bolometric applications (non-magnetic application)</p>
<p>TMR</p> 	<p>Spin- dependent tunnelling (<i>Extrinsic</i>)</p>	<p>~10<sup>3</sup>% (<i>negative at</i> <i>low field</i>)</p>	<p>Read-heads and MRAM</p>

MR<sup>1)</sup> is defined as  $(R_{\max} - R_{\min}) / R_{\min}$ .

---

## 1.3 Overview of the Dissertation

The main theme of the dissertation is an experimental study of spin-polarised tunnel junctions exploiting the half-metallicity of  $\text{La}_{0.7}\text{Ca}_{0.3}\text{MnO}_3$ . The work addresses some issues on the materials physics of mixed valence manganites  $\text{La}_{1-x}\text{Ca}_x\text{MnO}_3$  ( $0 < x < 1$ ), and magnetism in magnetic tunnel junctions, both of which are studied by tunnelling experiments.

Chapter 2 gives a brief review of the general background, particularly on the experimental situation of the field, in order to set this work in context. Three different subjects that are directly related to the following chapters are touched upon: (1) the recent experimental aspects of spin-polarised electron tunnelling, (2) the basic physics of mixed valence manganites particularly on the half-metallicity in the optimally doped manganite, and the tendency towards phase-separation, and (3) the magnetization reversal processes in ferromagnetic thin films. Experimental methods of this work including heteroepitaxial film growth, and the microfabrication processes are summarized in Chapter 3.

In Chapter 4, interfacial magnetism of  $\text{La}_{0.7}\text{Ca}_{0.3}\text{MnO}_3$  in lattice-mismatched epitaxial multilayers with  $\text{SrTiO}_3$  is addressed. The role of strain arising from lattice-mismatch is extended to the coherent growth of the heterostructures.

In the following chapters, the main experimental results of spin-polarised tunnelling junctions based on  $\text{La}_{0.7}\text{Ca}_{0.3}\text{MnO}_3$  are discussed around the role of the tunnel barrier. In Chapter 5, a study of lattice-engineered  $\text{La}_{0.7}\text{Ca}_{0.3}\text{MnO}_3/\text{NdGaO}_3/\text{La}_{0.7}\text{Ca}_{0.3}\text{MnO}_3$  junctions is presented. A phenomenological tunnelling mechanism based on percolative phase separation in  $\text{La}_{0.7}\text{Ca}_{0.3}\text{MnO}_3$  is proposed to account for the temperature dependence of the tunnelling magnetoresistance. Chapter 6 discusses a spin and charge modulated tunnel junction,  $\text{La}_{0.7}\text{Ca}_{0.3}\text{MnO}_3/\text{La}_{0.45}\text{Ca}_{0.55}\text{MnO}_3/\text{La}_{0.7}\text{Ca}_{0.3}\text{MnO}_3$  in which the various ground states of the mixed valence manganites are exploited. An active role of the magnetic barrier is also proposed.

Chapter 7 describes the magnetization reversal processes in the magnetic tunnel junctions investigated by two-dimensional angular junction measurements. The edge-domain pinning effect is suggested to play a crucial role in the coherent magnetization reversal in the present junctions.

Finally this dissertation ends with summary and some outlook in the field in Chapter 8.

---

---

**REFERENCES**

- 
- <sup>1</sup> For example see, G.A. Prinz, *Phys. Today* April., 58 (1995).
- <sup>2</sup> For example see, G.A. Prinz, *Science* **282**, 1660 (1998) and P. Ball, *Nature* **404**, 918 (2000).
- <sup>3</sup> J.M. Kikkawa and D.D. Awschalom, *Nature* **397**, 139 (1999).
- <sup>4</sup> H. Ohno, D. Chiba, F. Matsukura, T. Omiya, E. Abe, T. Dieti, Y. Ohno and K. Ohtani, *Nature* **408**, 944 (2000).
- <sup>5</sup> For example see, D.P. Divincenzo, *Science* **270**, 255 (1995).
- <sup>6</sup> A.B. Pippard, “Magnetoresistance in metals”, Cambridge University Press, Cambridge (1989).
- <sup>7</sup> J.P. Heremans, *Mat. Res. Soc. Symp. Proc.* **475**, 63 (1997).
- <sup>8</sup> T.R. McGuire and R.I. Potter, *IEEE Trans. Magn.* **MAG-11**, 1018 (1975).
- <sup>9</sup> I.A. Campbell and A. Fert, “Transport properties in ferromagnets” in “Ferromagnetic materials”, Vol. 3, ed. by E.P. Wohlfarth, North-Holland, Amsterdam (1982).
- <sup>10</sup> M.N. Baibich, J.M. Broto, A. Fert, F. Nguyen van Dau, F. Petroff, P. Etienne, G. Creuzet, A. Friederich and J. Chazelas, *Phys. Rev. Lett.* **61**, 2472 (1988).
- <sup>11</sup> S. S. P. Parkin, N. More, and K. P. Roche, *Phys. Rev. Lett.* **64**, 2304 (1990).
- <sup>12</sup> R. von Helmholt, J. Singleton, D.A. Keen, R. McGreevy and K. Samwer, *Phys. Rev. Lett.* **71**, 2331 (1993).
- <sup>13</sup> S. Jin, T.H. Tiefel, M. McCormack, R.A. Fastnach, R. Ramesh and L.H. Chien, *Science* **264**, 413 (1994) and M. McCormack, S. Jin, T. H. Tiefel, R. M. Fleming, Julia M. Phillips, and R. Ramesh, *Appl Phys. Lett.* **64**, 3045 (1994).
- <sup>14</sup> Y. Moritomo, A. Asamitsu, H. Kuwahara and Y. Tokura, *Nature* **380**, 141 (1996).
- <sup>15</sup> K.-I. Kobayashi, T. Kimura, H. Sawada, K. Terakura and Y. Tokura, *Nature* **395**, 677 (1998).
- <sup>16</sup> Y. Shimakawa, Y. Kubo and T. Manako, *Nature* **379**, 53 (1996).
- <sup>17</sup> H.Y. Hwang and S.-W Cheong, *Nature* **389**, 942 (1997).
- <sup>18</sup> J.S. Moodera, L.R. Kinder, T.M. Wong, R. Meservey, *Phys. Rev. Lett.* **74**, 3273 (1995).
- <sup>19</sup> W.J. Gallagher, S.S.P. Parkin, Y. Lu, X.P. Bian, A.C. Marley, K.P. Roche, R.A. Altman, S. Rishton, C. Jahnes, T.M. Shaw and G. Xiao, *J. Appl. Phys.* **81**, 3741 (1997).
-

---

## **CHAPTER 2**

### **Background Reviews**

---

2.1 Spin Polarised Electron Tunnelling

2.2 Half-metallic Manganites

2.3 Magnetization Processes in Spin Polarised Tunnel Junctions

## 2.1 Spin Polarised Electron Tunnelling

### 2.1.1 Quantum mechanical electron tunnelling<sup>1</sup>

Quantum mechanical electron tunnelling is the movement of electrons through energy barriers that, on classical theory, they would have insufficient energy to surmount. Tunnelling processes are fundamental to quantum mechanics, following directly from the nature of the solutions  $\Psi(x)$  of Schrödinger's equation and the probability interpretation of  $\Psi^*\Psi$ . The rate at which such processes occur is dependent on an evanescent wave function that decays exponentially in a tunnel barrier where the barrier potential  $U(x, V)$  varies by the distance from the metal surface ( $x$ ) and an applied voltage ( $V$ ). For a square potential barrier, the transmission coefficient ( $T$ ) for an electron of kinetic energy  $E$  ( $U > E$ ) can be adequately estimated from the Wentzel-Kramers-Brillion (WKB) approximation as

$$T = \exp\left[-2 \int_{x_1}^{x_2} \sqrt{\frac{2m\{U(x, V) - E\}}{\hbar^2}} dx\right], \quad [2.1]$$

where  $x_1$  and  $x_2$  are the classical turning points.

One useful way to look at electron tunnelling in solid-state structures is via the so-called transfer Hamiltonian calculations. This concept was first proposed by Oppenheimer in his work on the field ionization of hydrogen<sup>2</sup>, and then was extended by Bardeen to the mathematical explanation<sup>3</sup> for the first demonstration of tunnelling in the metal-insulator-metal structures. In this picture, the system can be described as a barrier (I) that separates the system into two nearly independent metallic parties ( $M_1$  and  $M_2$ ). The probability of tunnelling through the barrier is related to the weak coupling of the two attenuating wave functions in the barrier,  $\Psi_1$  and  $\Psi_2$ , as illustrated in Fig. 2.1. The Hamiltonian of the system can be then expressed as

$$\hat{H} = \hat{H}_1 + \hat{H}_2 + \hat{H}^T, \quad [2.2]$$

where  $H^T$ , the residual coupling in the barrier is treated with a perturbation theory. According to Fermi's Golden rule the transition from one side ( $M_1$ ) to the other ( $M_2$ ) is given by

$$w_{21} = \left(\frac{2\pi}{\hbar}\right) |M|^2 \rho(U_2) \delta(U_2 - U_1), \quad [2.3]$$

where  $|M| = |\langle \Psi_{M2} | \hat{H}^T | \Psi_{M1} \rangle|$  and is independent of the initial and final states, and  $\rho$  is the density of states (DOS). The explicit appearance of the DOS in the transmission rate is particularly useful for understanding the expression.

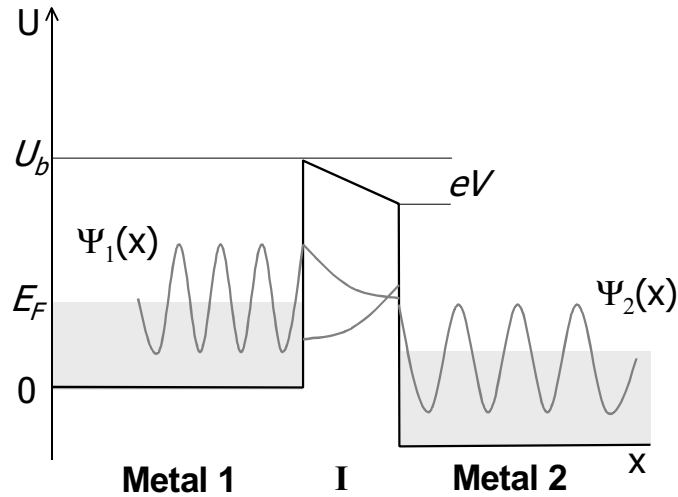


**Fig. 2.1.** The transfer Hamiltonian picture for quantum electron tunnelling between two metals across a barrier (I) under a small bias voltage.

In an actual tunnelling experiment the physical quantity usually measured is either the current density ( $J$ ) or its derivative (the conductance  $G = \partial J / \partial V$ ) under a bias voltage  $V$ . An intuitive expression for the tunnelling conductance in the low temperature ( $T \ll E_F$ ) in the low voltage limit ( $eV \ll E_F$ ), where  $E_F$  is the Fermi level, can be derived as follows.

The potential difference due to an applied voltage  $V$  causes the chemical potential in metal 1 to be,  $\mu_1 = \mu_2 + eV$ . The DOS at  $E$  in metal  $i$  is  $\rho(U - \mu_i)$ , where  $E_i = U - \mu_i$ , i.e. the energy measured with respect to  $\mu_i$ . The rate of tunnelling into metal 1 for an electron in metal 2 with energy  $E$  can be given by Fermi's Golden rule as

$$w_{21} \propto |M|^2 \rho(E), \quad [2.4]$$

where the value of  $\rho(E)$  is the DOS multiplied by the probability that the states are

*(continued)*

unoccupied, i.e.

$$[1 - f(U - \mu_1)] \rho(U - \mu_1) = [1 - f(E)] \rho_1(E), \quad [2.5]$$

where  $f(E)$  is the Fermi function. Thus

$$w_{21} \propto |M|^2 [1 - f(E)] \rho_1(E). \quad [2.6]$$

The total number of electrons at  $E$  in metal 2 that might tunnel as described above is  $\rho_2(E+eV)f(E+eV)$  and the tunnelling current can be given by integrating over  $E$  as

$$J_{2-1} = -eK \int_{-\infty}^{\infty} |M|^2 \rho_2(E+eV) f(E+eV) \rho_1(E) [1 - f(E)] dE, \quad [2.7]$$

where  $K$  is a constant which depends on the geometry of the junction. In the same way

$$J_{1-2} = -eK \int_{-\infty}^{\infty} |M|^2 \rho_1(E) f(E) \rho_2(E+eV) [1 - f(E+eV)] dE, \quad [2.8]$$

and the net current density is given by  $J_{net} = J_{2-1} - J_{1-2}$

$$J_{net} = eK \int_{-\infty}^{\infty} |M|^2 \rho_1(E) \rho_2(E+eV) [f(E) - f(E+eV)] dE. \quad [2.9]$$

The factor  $[f(E) - f(E+eV)]$  in the  $T \rightarrow 0$  limit becomes a delta function. Because the potential difference  $eV$  is much smaller than  $E_F (\approx \mu_i)$ ,  $\rho_1$  and  $\rho_2$  do not change very much in the region in which this factor (and thus the integral) is non-zero. Therefore with

$$[f(E) - f(E+eV)] \approx -eV (df/dE) \quad [2.10]$$

one can derive from Eq [2.9],

$$J_{net} = K |M|^2 \rho_1(E_F) \rho_2(E_F) e^2 V, \quad [2.11]$$

which gives the conductance

$$G = e^2 K |M|^2 \rho_1(E_F) \rho_2(E_F). \quad [2.12]$$

This expression of tunnelling conductance, which is proportional to the product of the DOS at  $E_F$  of the two metals is useful to envisage the concept of spin polarised.

The development of analytical solutions of tunnelling conductance in the MIM structures were refined notably by Simmons<sup>4</sup> and Stratton<sup>5</sup> by careful consideration of the transmission factors as

$$J(V) = J_0 \{ \bar{\phi} \exp(-A \bar{\phi}^{1/2}) - (\bar{\phi} + eV) \exp[-A(\bar{\phi} + eV)^{1/2}] \} \quad (\text{Simmons}), \quad [2.13]$$

where  $\bar{\phi}$  is the average barrier height (i.e.  $\bar{\phi} = \frac{1}{t} \int_{x_1}^{x_2} \phi(x) dx$ ), and  $t$  is the barrier width,

$$J_0 = \frac{e}{2\pi\hbar(\beta t)^2} \quad \text{and} \quad A = \left(\frac{4\pi\beta t}{\hbar}\right)(2m)^{1/2}. \quad [2.14]$$

Alternatively

$$J(V) = \left(\frac{4\pi me}{\hbar^3 c_1^2}\right) \exp(-b_1) [1 - \exp(-c_1 V)] \quad (\text{Stratton}), \quad [2.15]$$

where the barrier height  $\phi$  is an arbitrary function including the effect of applied voltage,

$$\text{i.e., } \phi_1(x, V) = \phi(x) - \frac{eVx}{t} \quad [2.16]$$

$$\text{and } b_1(V) = \frac{\sqrt{8m}}{\hbar} \int_{x_{11}}^{x_{21}} \phi_1(x)^{1/2} dx, \quad c_1(V) = \frac{\sqrt{2m}}{\hbar} \int_{x_{11}}^{x_{21}} \phi_1(x)^{-1/2} dx. \quad [2.17]$$

Although a different approximation was adopted for symmetric barriers in Eq. [2.13] and [2.15], the results arrive at the very similar contexts. Typically for very small  $V$  and  $T$  both expressions can be expanded in a power series as

$$J(V) = \alpha V + \gamma V^3 + \dots, \quad \text{or} \quad [2.18]$$

$$G(V) = \alpha + 3\gamma V^2 + \dots, \quad [2.19]$$

and they show a cubic term  $V^3$  in addition to the basic linear term  $V$  in  $J(V)$ , and a parabolic term  $V^2$  in  $G(V)$ . A typical parabolic behaviour in the low voltage ranges of  $G(V)$  in the MIM junctions is shown in Fig. 2.2.

Simmons's formula for the  $J$ - $V$  tunnelling characteristics are often used to extract  $t$  and  $\phi$  by fitting the experimental data. However in actual tunnel junctions there is likely to be a deviation from a perfect tunnelling due to pin-holes and defects in the barrier. The apparently measured  $J(V)_{\text{meas}}$  can involve a parasitic conductance due to such barrier imperfections and can be written as

$$J(V)_{\text{meas}} = (1-q)J(V) + qP(V) \quad [2.20]$$

where  $J(V)$  is defined in Eq. [2.18] and  $P(V)$  is a parasitic conductance. The term  $q$  is the weight of the parasitic conductance, so  $q = 0$  represents perfect tunnelling. The functional form of  $P(V)$  can then be anything between linear ohmic functions and more complex non-linear ones according to the nature of the imperfection, i.e. the size and distribution of defects in the barrier. Therefore meticulous care should be taken when estimating the barrier height and width by fitting experimental data.

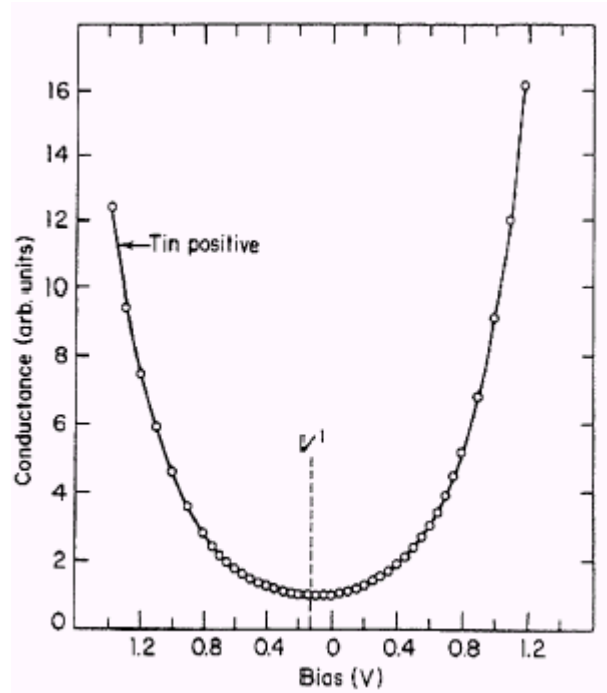


**Fig. 2.2.** Typical experimental tunnelling conductance (Al/I/Sn junction at 4.2K). Note that the conductance is relatively flat at low voltage (400mV) and the variation becomes parabolic at a higher voltage bias. (After Ref. [6].)

### 2.1.2 Definitions of spin polarisation

The degree of spin polarisation,  $P$  is a quantity of fundamental interest for both physics and applications in spin polarised tunnelling. In metallic ferromagnets, it is defined as the degree of DOS asymmetry between spin sub-bands at  $E_F$ , and originates from the exchange energy ( $\mu_B H$ ). It can be written as

$$P \equiv \frac{n_{\uparrow} - n_{\downarrow}}{n_{\uparrow} + n_{\downarrow}}, \quad [2.21]$$

where  $n_i$  ( $i = \uparrow$  and  $\downarrow$ ) is the DOS of the spin sub-bands at  $E_F$  and it is generally proportional to the bulk magnetization ( $M$ ). It is conventional to determine the sign of  $P$  to be positive (negative) when the spin-quantized axis of majority (minority) spins is parallel (anti-parallel) to the bulk magnetization. In most elemental ferromagnets the DOS of minority spins exceeds that

of majority spins and thus one can expect a negative polarisation. It should, however, be noted that there is no general correlation between the sign of  $P$  and  $M$ :  $P$  is a function of the DOS at the Fermi surface, and thus depends on the shape of the DOS at  $E_F$ , whereas  $M$  is subject to the integrated DOS in the Fermi sea and localized moments if there are any.<sup>7,8</sup>

Meservey and Tedrow pioneered the systematic measurement of  $P$  of metallic ferromagnets in superconductor–insulator–ferromagnet (S/I/F) tunnel junction systems, where they used superconductors as a spin analyzer exploiting the Zeeman-split quasiparticle DOS in the superconductors.<sup>9</sup> The measured  $P$  of representative elemental ferromagnetic metals by their method is summarized in Table 2.1.

Table 2.1 Spin polarisation of several ferromagnets measured by Meservey and Tedrow. (After Ref. [9].)

Ferromagnetic metals	Polarisation (%)
Fe	$+ 40 \pm 2$
Co	$+ 35 \pm 3$
Ni	$+ 23 \pm 3$
Gd	$+ 14 \pm 3$
Ho	$+ 7.5 \pm 1$
Tb	$+ 6.5 \pm 1$
Er	$+ 5.5 \pm 1$
Dy	$+ 7.0 \pm 1$
Tm	$+ 2.7 \pm 1$

There have been several other sophisticated methods employed for the measurement of  $P$  such as spin-resolved photoemission, field emission, Andreev reflection and spin polarised scanning tunnelling measurements. However, strictly speaking, the measured quantity  $P$  in

dissimilar measurement techniques does not necessarily have unanimously the same physical origins (nevertheless all values are intimately related to  $n_i$ ) because each technique probes slightly different physical entities with different energy scales.<sup>3,4</sup> That is, the measured P does not necessarily represent the DOS of spin sub-bands at  $E_F$  alone. Andreev reflection<sup>4</sup> probes the ratio of the spin currents in the superconducting and the normal states, namely

$$\begin{aligned} P &= \frac{J_{\uparrow} - J_{\downarrow}}{J_{\uparrow} + J_{\downarrow}} = \frac{\langle nv^2 \rangle_{\uparrow} - \langle nv^2 \rangle_{\downarrow}}{\langle nv^2 \rangle_{\uparrow} + \langle nv^2 \rangle_{\downarrow}} \\ \text{or} &= \frac{\langle nv \rangle_{\uparrow} - \langle nv \rangle_{\downarrow}}{\langle nv \rangle_{\uparrow} + \langle nv \rangle_{\downarrow}} \end{aligned} \quad [2.22]$$

where the weights  $\langle nv^2 \rangle_i$  and  $\langle nv \rangle_i$  are for the diffusive and ballistic limit at the S/F interface ( $n$  is the number of conduction electrons and  $v$  is the Fermi velocity). Photoemission measurement probes the population of excited electrons from few eV below  $E_F$  in the band at the F/vacuum interface. In the S/I/F tunnel junctions, it measures direct tunnelling conductance under typically a few mV of bias via the height variations in the conductance peaks.

In contrast to the direct measurement techniques mentioned above, the  $F_1/I/F_2$  tunnel junction measurements indirectly give P from the tunnelling magnetoresistance (TMR). A simple expression of the relation between the TMR and P was first put forward by Jullière<sup>10</sup> as

$$\text{TMR} = \frac{G_p - G_{ap}}{G_p} = \frac{R_{ap} - R_p}{R_{ap}} = \frac{2P_1P_2}{1 + P_1P_2} \quad [\text{I}], \quad [2.23]$$

$$= \frac{G_p - G_{ap}}{G_{ap}} = \frac{R_{ap} - R_p}{R_p} = \frac{2P_1P_2}{1 - P_1P_2} \quad [\text{II}], \quad [2.24]$$

where  $G_i$  and  $R_i$  are the conductance and the resistance with parallel ( $G_p \propto n_{1\uparrow}n_{2\uparrow} + n_{1\downarrow}n_{2\downarrow}$ ) and anti-parallel ( $G_{ap} \propto n_{1\uparrow}n_{2\downarrow} + n_{1\downarrow}n_{2\uparrow}$ ) magnetization between  $F_1$  and  $F_2$ , and  $P_i$  is the inferred P of  $F_i$ . Note that the magnitude of TMR is insensitive to the relative sign of  $P_1$  and  $P_2$ , and the sign of TMR is always positive regardless of the sign of P.

It should be noted that TMR can be normalized with either the parallel or anti-parallel resistance (conductance), where TMR [I] ranges between 0 and 100% whereas TMR [II] between 0 and infinity. The definition [II] will be quoted throughout this Chapter unless explicitly mentioned otherwise simply because it is frequently adopted in the literature, although definition [I] will be used in the main results of this thesis work. Jullière's model involves oversimplifications such as no spin mixing between the two spin current channels, and no spin scattering. However it is still readily accepted mainly because the relation between TMR and P is straightforward and the inferred P agrees fairly well with the value from other direct measurements.

### 2.1.3 Spin polarised tunnel junctions

Spin polarised tunnel junctions involve two similar or dissimilar ferromagnetic metals separated by a very thin insulator. They exploit asymmetric tunnelling conductances between asymmetric spin sub-bands. The concept of spin dependent tunnelling can be postulated assuming two sub-spin conductance channels without no spin-mixing as presented in Fig. 2.3.

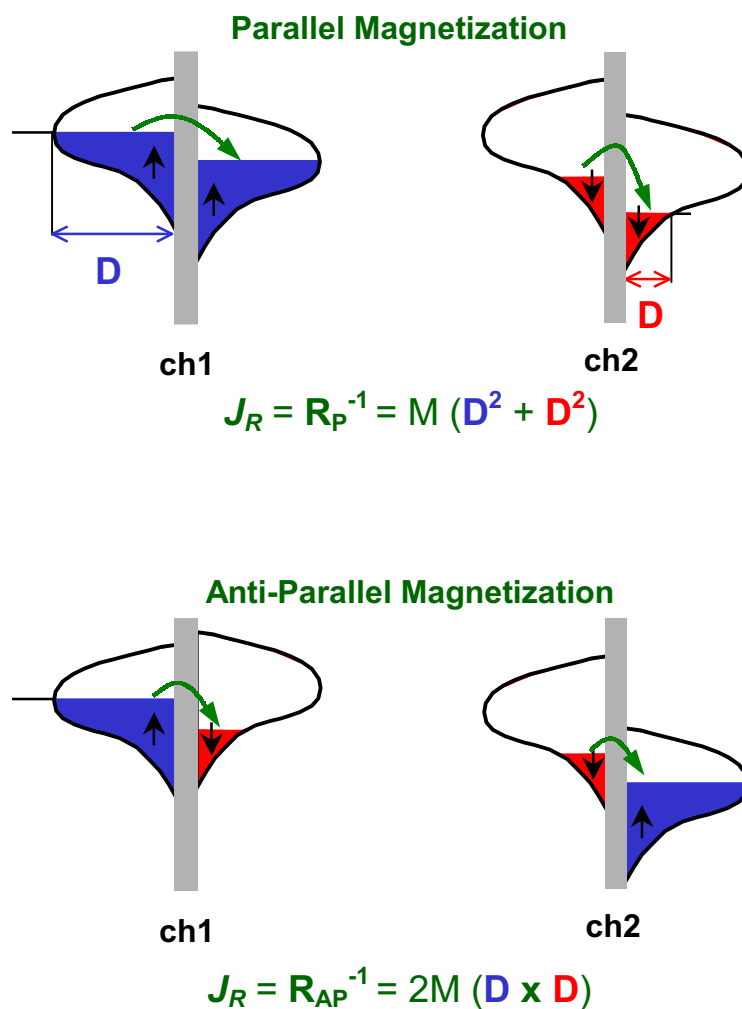


**Fig. 2.3.** Conceptual representation of spin polarised tunnelling. The conductance ( $J_R$ ) for parallel magnetization is greater than the one for the anti-parallel case due to the asymmetry of the DOS ( $D$ ) of majority and minority sub-spin bands.  $M$  stands for the matrix element for tunnelling.

In 1975 Jullière demonstrated the first experimental spin polarised tunnelling with a Fe/Ge/Co system,<sup>10</sup> where the Ge barrier was 10-15nm thick, and he observed a TMR of 14% in the zero bias limit at 4.2K, although later it became controversial because a semiconducting Ge barrier turned out to produce negligible polarisation due to significant spin scattering in other experiments; for example the TMR is only < 0.1% in the junctions of the same composition. Then few years later Maekawa and Gäfvert<sup>11</sup> measured a TMR of ~2% at 4.2K in a Ni/NiO/Co system where the relative orientations of the magnetizations are well correlated with the coercivities of Ni and Co films as in Fig. 2.4. Note that in their junction the barrier NiO is an antiferromagnetic insulator.

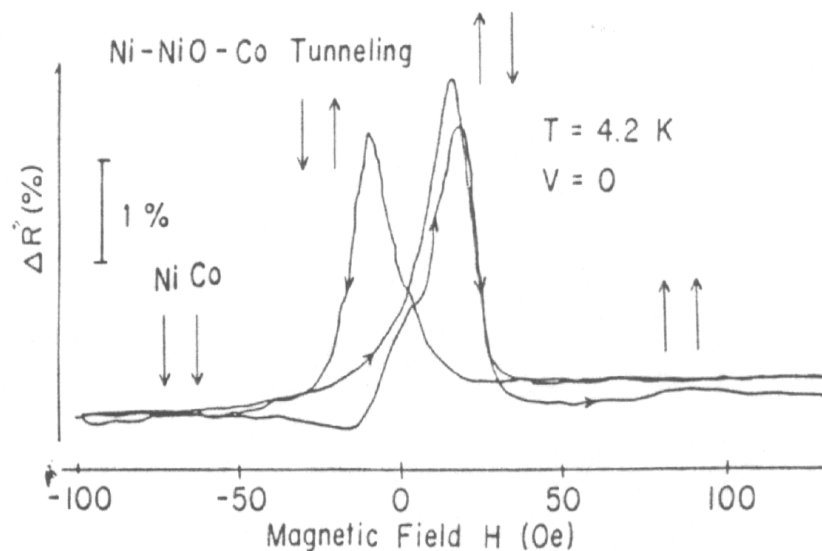


**Fig. 2.4.** Magnetoresistance ( $\Delta R/R$ ) of Ni/NiO/Co junctions at 4.2 K. Arrows represent the relative orientation of magnetization of Ni and Co. (After Ref. [11].)

Although there have been continuous efforts towards better junction quality, particularly with barriers such as NiO<sup>12</sup>, GdO<sub>x</sub><sup>13</sup> and CoO<sup>14</sup>, it was not until 1995 that a large and reproducible TMR of 13.4% (31.6% at 4.2K) at room temperature (RT) was reported by Moodera *et al.*<sup>15</sup> – see Fig. 2.5. They used an *in-situ* oxidized amorphous Al<sub>2</sub>O<sub>3</sub> tunnel barrier ( $\phi \sim 1.9\text{eV}$ ) in CoFe/ $\alpha$ -Al<sub>2</sub>O<sub>3</sub>/Co junctions. Until now  $\alpha$ -Al<sub>2</sub>O<sub>3</sub> has been known as the most reproducible barrier in standard tunnel junctions. Nowadays a TMR of ~20% at RT with thinner  $\alpha$ -Al<sub>2</sub>O<sub>3</sub> barriers (1-2nm) can be routinely reproduced with low coercivity materials: Advanced device architectures such as exchange-biased tunnel junctions<sup>16</sup> are shown in Fig. 2.6. Their prototypical applications are commercially available such as magnetic random-access memories.<sup>17</sup>

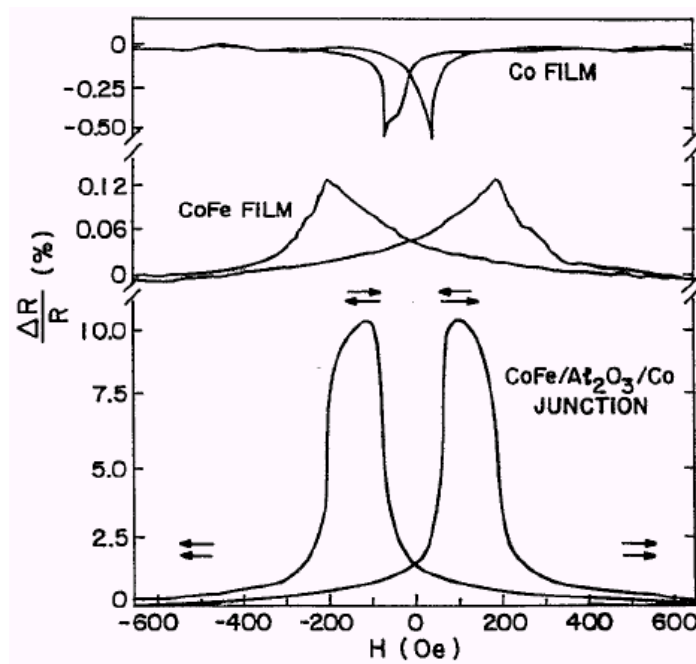


**Fig. 2.5.** Tunnelling magnetoresistance in a CoFe/ $\alpha$ - $\text{Al}_2\text{O}_3$ /Co junction at RT. Also shown are the resistances of individual electrodes in which the peaks are related to the relative configuration of magnetization in the electrodes. (After Ref. [15].)

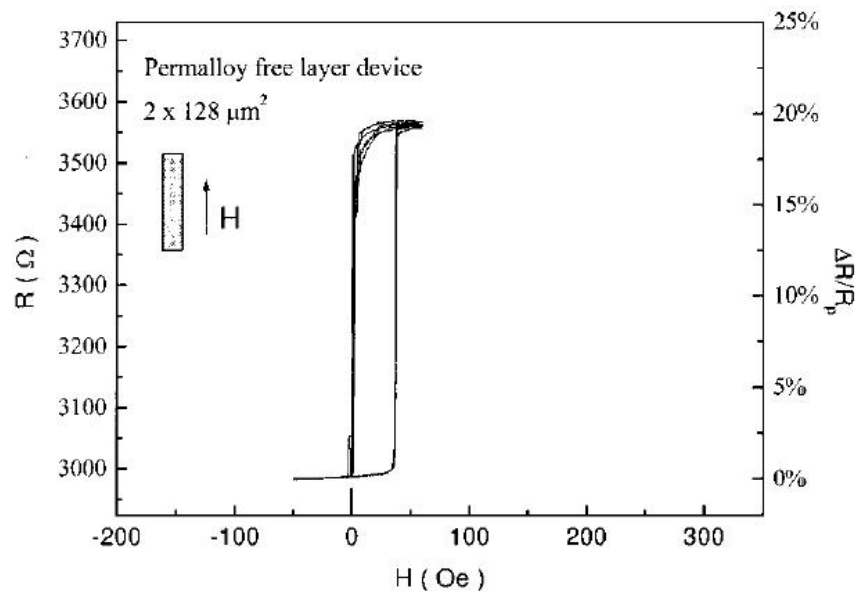


**Fig. 2.6.** Tunnelling junction resistance and magnetoresistance versus magnetic field of exchange biased  $\text{Ni}_{81}\text{Fe}_{19}/\alpha$ - $\text{Al}_2\text{O}_3$ /Co//MnFe at RT. Two stable resistive states (high and low) exist at zero field. (After Ref. [16].)

It is evident from the relation between TMR and polarisation in Eq. [2.23] and [2.24] that the highest possible TMR can be achieved by employing ferromagnetic metals of the highest spin polarisation as is graphically shown in Fig. 2.7. There have been extensive world-wide research efforts to explore such high polarisation materials, i.e. the conduction electrons are fully spin-polarised, namely half-metals.<sup>18</sup> So far several complex compounds are predicted to be half-metals such as the spinels  $\text{CuCr}_2\text{S}_4$  and  $\text{Fe}_3\text{O}_4$ ; Heusler alloys  $\text{NiMnSb}$  and  $\text{Co}_2\text{MnSi}$ ; and rutile  $\text{CrO}_2$ . There are even more complicated oxides; perovskite manganites  $\text{La}_{0.7}\text{Ca}_{0.3}\text{MnO}_3$  and  $\text{La}_{0.7}\text{Sr}_{0.3}\text{MnO}_3$ ; double perovskites  $\text{Sr}_2\text{FeMoO}_6$  and  $\text{Sr}_2\text{ReMoO}_6$ ; and pyrochlore  $\text{Tl}_2\text{Mn}_2\text{O}_7$ . However large TMR at room temperature has not been reported to date, partly because of relatively low  $T_C$  values and partly because of the genuine difficulty in high quality materials syntheses.

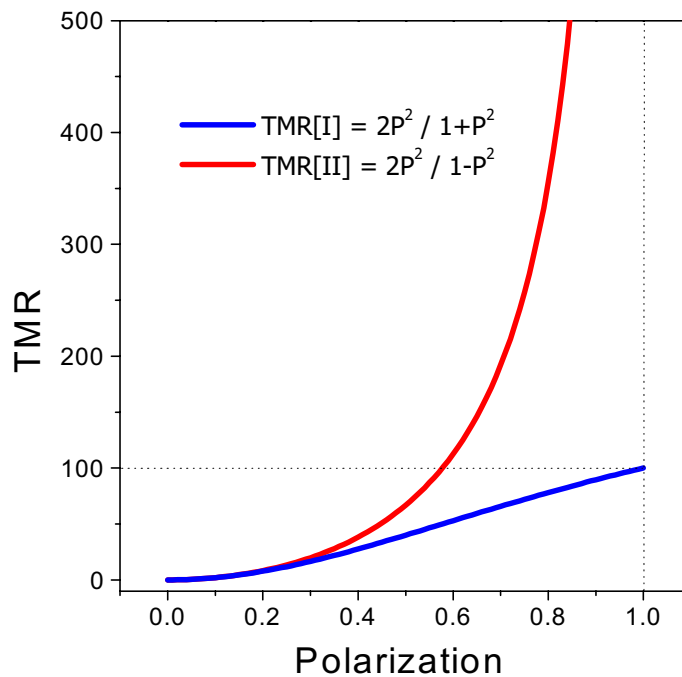


**Fig. 2.7.** Calculated TMR dependence on spin polarisation from Eq. [2.23] and [2.24].

Among such materials, mixed valence manganites have received considerable attention, mainly because of their intrinsic large-magnetoresistance (up to 10<sup>6</sup>% in a few T), dubbed colossal magnetoresistance (CMR) since its discovery in 1994.<sup>19</sup> In fact the major motivation for researching the mixed valence manganites is rather different and arises because of

---

fundamental physics<sup>20</sup> of strong electron correlations such as CMR, charge/orbital ordering and the explicit half-metallicity, and the readiness of materials synthesis. Spin polarised tunnelling based on these materials is separately discussed in the last section of this Chapter.

### 2.1.4 Experimental aspects of spin polarised tunnelling

There are strict requirements for achieving high quality of magnetic tunnel junctions such as, most notably, perfectly smooth and sharp (structurally, chemically and electronically) interfaces between electrodes and barriers, a defect free barrier and separately tunable magnetization states in each ferromagnetic electrode. It was only until recently that one could be successful in fabricating such well-defined tunnel junction systems with the aid of the current developments in vacuum technology. Since then many important issues on spin polarised tunnelling have been addressed both from the theoretical and experimental points of view.

Here in this section, several experimental points of view, which are most notable in recent years, are selectively discussed. First the common features of magnetic tunnel junctions are reviewed and then in addition junctions based on manganites are discussed separately.

#### 2.1.4.1 Inelastic spin tunnelling

Electron tunnelling is a non-linear element and tunnelling conductance ( $G$ ) versus applied bias shows a nearly quadratic dependence. Experimentally the junction conductance in spin polarised tunnel junctions often shows dissimilar bias dependence in the parallel and anti-parallel configurations. However the TMR is significantly suppressed with increasing bias voltage as shown in Fig. 2.8(a)<sup>21</sup>. Note that the simple Jullière model based on the two current-channel assumption does not explicitly take into consideration the effects of conduction band structure, tunnelling transmission, and spin-flip excitations and thus, predicts no bias voltage dependence for the TMR. Due to the influence of the applied electric field on the barrier shape, the TMR was predicted to decrease with increasing bias, however the simple models were quantitatively unsuccessful to account for such a large suppression as in Fig. 2.8(b).<sup>21</sup>

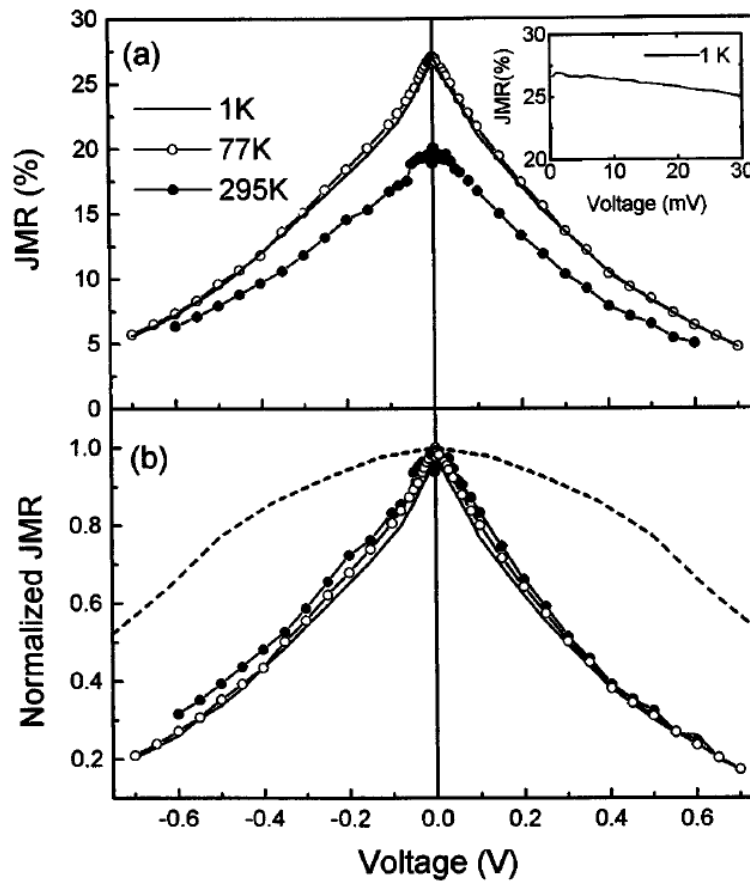


**Fig. 2.8.** TMR versus dc bias at three temperatures for a Co/Al<sub>2</sub>O<sub>3</sub>/Ni<sub>80</sub>Fe<sub>20</sub> junction. Data shown are (a) the actual percentages and (b) normalized at zero bias. The inset shows the JMR in the low bias region displaying near constant JMR. The dashed line in (b) is the theoretically expected variation for a Fe/Al<sub>2</sub>O<sub>3</sub>/Fe junction with the barrier height of 3eV. (After Ref. [21].)

Lu *et al.*<sup>22</sup> also reported a similar bias dependence with a sharp cusp near zero bias at low temperatures (zero bias anomaly) as seen in Fig. 2.9, which had been previously referred to as a signature of metallic impurities in the barrier.<sup>23</sup>

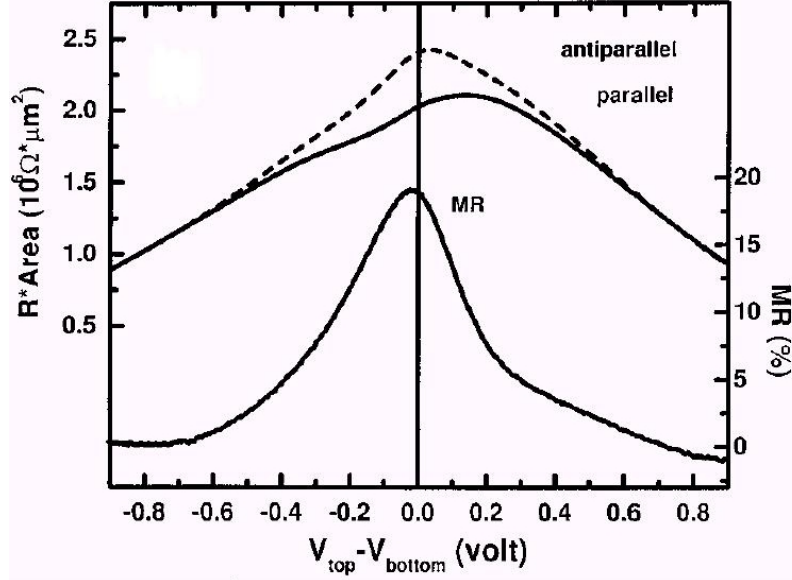


**Fig. 2.9.** Differential junction resistance-area product in parallel and anti-parallel magnetization and the corresponding TMR as a function of dc bias voltage on the junction. (After Ref. [22].)

Later Zhang *et al.*<sup>24</sup> attributed this bias dependence to an inelastic tunnelling process, i.e. spin wave excitations at the interfaces due to hot electrons. Moodera *et al.*<sup>21</sup> also proposed a similar argument based on their inelastic electron tunnelling spectroscopy measurements. Bratkovski<sup>25</sup> provided an improved model of bias dependence including interface phonon excitations to the interfacial spin scattering.

TMR also shows temperature dependence: in general TMR tends to decrease with increasing temperatures. Although most theoretical models of spin polarised tunnelling are based on the zero temperatures and the zero bias limits, the temperature dependence of spin polarised tunnelling has potentially both a spin independent and spin dependent component. Normal tunnelling conductance itself is temperature-dependent due to thermally activated conduction processes via defective states in the barrier, and thermal smearing of conduction electrons near  $E_F$ , i.e. as in Stratton's model<sup>5</sup>

$$\frac{G(V,T)}{G(V,0)} = \frac{\pi c k_B T}{\sin(\pi c k_B T)}. \quad [2.25]$$

In addition, the bulk magnetization (M) of ferromagnetic metals and thus the spin polarisation

of a ferromagnet is a function of temperature, i.e. below  $T_C$  using for spin  $S = 1/2$ ,  $M$  can be expressed as

$$M = N\mu \tanh\left(\frac{\mu H}{k_B T}\right), \quad [2.26]$$

with  $H$  being applied field. Therefore the TMR is bound to fall off with increasing temperature to a certain degree depending on the value of  $T_C$ .

Shang *et al.*<sup>26</sup> analyzed their experimental results of the TMR based on a phenomenological model of the temperature dependence as in Fig. 2.10, where they wrote the junction conductance as

$$G(\theta) = G_e[1 + P_1 P_2 \cos(\theta)] + G_{in} \quad [2.27]$$

where  $G_e$  is the prefactor for elastic tunnelling,  $\theta$  is the relative angle between the magnetization of the electrodes and  $G_{in}$  is the inelastic tunnelling component. They could successfully fit their data with three temperature-dependent variables,  $G_e(T)$ ,  $P(T)$  and  $G_{in}(T)$ . They found the dominant factor  $P(T)$  to be proportional to thermally excited spin waves (magnon), which follow the Bloch  $T^{3/2}$  law for  $M$ :

$$P(T) = P(T)(1 - \alpha T^{3/2}) \quad [2.28]$$

where  $\alpha$  is a material dependent constant.

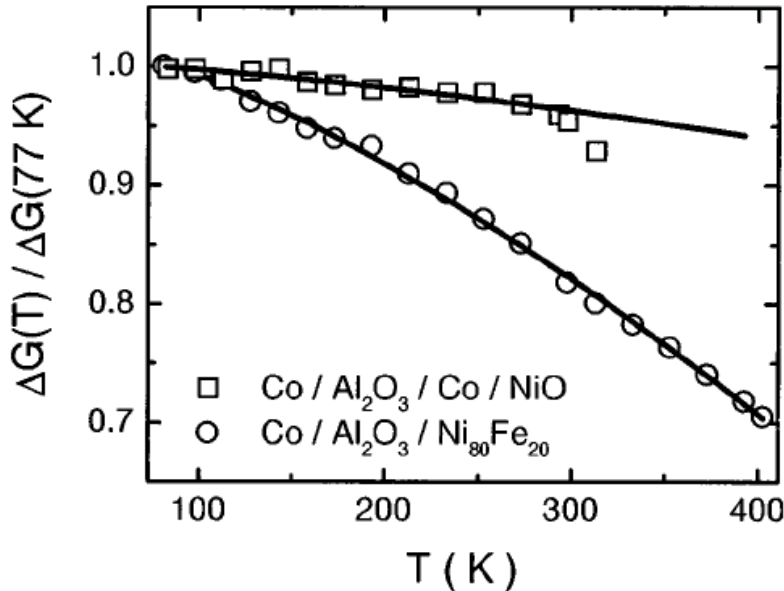


**Fig. 2.10.** Temperature dependence of the normalized conductance of two representative ferromagnetic junctions. The solid lines are the fits to the theory based on thermal spin-wave excitations. (After Ref. [26].)

### 2.1.4.2 Interfacial band structures

Electron tunnelling is a surface or interface phenomenon and typically in tunnelling junction experiments only electrons just below  $E_F$  at surfaces or interfaces are involved. Meanwhile electronic band structures of ferromagnets are often calculated based on the bulk symmetry of a given material. In this section, current issues on the influence of interfacial band structures on spin polarised tunnelling are reviewed.

#### *Crystal anisotropy of the TMR*

Yuasa *et al.*<sup>27</sup> studied the dependence of the TMR on the crystal orientation of *single crystal* Fe electrodes in Fe/Al<sub>2</sub>O<sub>3</sub>/Fe<sub>50</sub>Co<sub>50</sub> junctions. Note that most ferromagnets in the tunnel junctions mentioned above are polycrystalline. The results are as shown in Fig. 2.11.

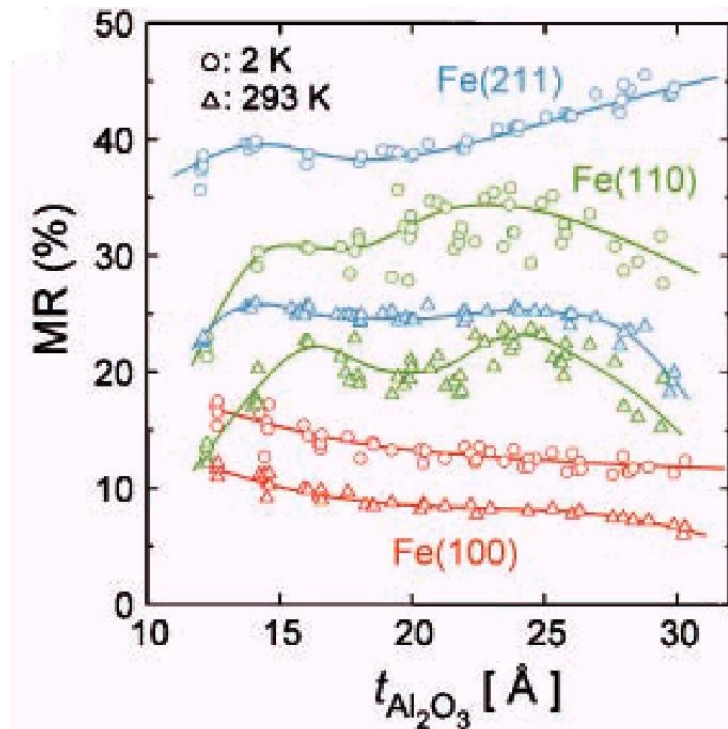


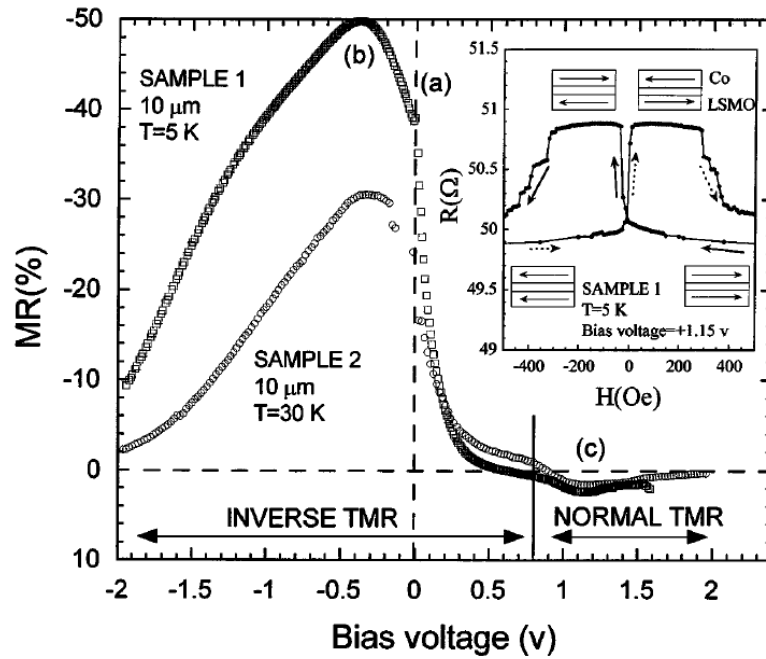
**Fig. 2.11.** TMR of Fe/Al<sub>2</sub>O<sub>3</sub>/Fe<sub>50</sub>Co<sub>50</sub> junctions as a function of barrier thickness, where the Fe layer is a single crystal oriented with (100), (110) and (211) surfaces of the interfaces. (After Ref. [27].)

They found a TMR of 13% for Fe(100), 32% for Fe(110) and 42% for Fe(211) at 2K and a similar variation at room temperature. In fact, the spin polarisation must reflect the crystal anisotropy of the incident Bloch wave,  $e^{ikx}$  in the Fermi surface, which enters the transmission probability term in the calculations. Indeed their calculations based on the layer Korringa-Kohn-Rostoker method of  $k$  (Bloch wave vector) resolved spin polarisation were consistent with the experimental data, although they did not consider the possible interfacial scattering from the contribution of the off-normal momentum.

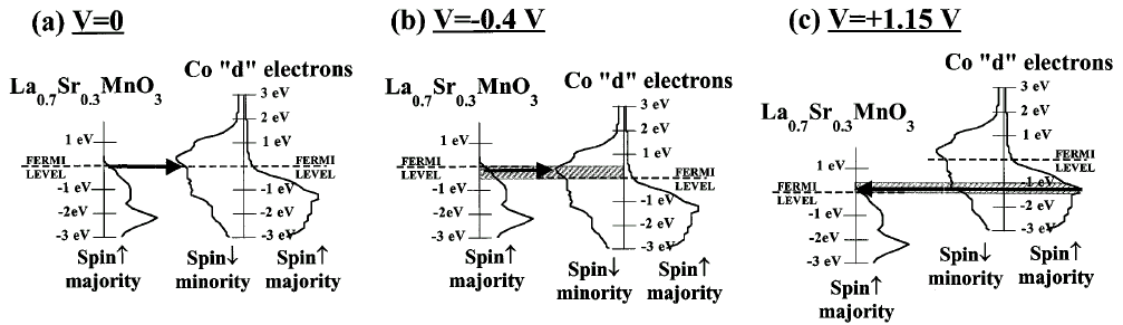
### *Interfacial hybrid band structures*

A significant role of interfacial hybrid band structures in spin polarised tunnelling was reported by Sharma *et al.*<sup>28</sup>, where they found an inversion of the TMR in  $\text{Ni}_{80}\text{Fe}_{20}/\text{Ta}_2\text{O}_5\text{-Al}_2\text{O}_3/\text{Ni}_{80}\text{Fe}_{20}$  junctions in a certain bias voltage range. Similarly De Teresa *et al.*<sup>29</sup> also reported a unusual bias voltage dependence of the TMR in  $\text{Co}/\text{SrTiO}_3/\text{La}_{0.7}\text{Sr}_{0.3}\text{MnO}_3$  junctions, in which they observed a variation in both the magnitude and the sign of the TMR – See Fig. 2.12(a). They both interpreted their observations in the context of the interfacial bonding character of the conduction electron band of the ferromagnets. For example de Teresa *et al.* attributed their results to the predominant  $d$ - $d$  bonding (Co-Ti or Sr) between Co and the barrier  $\text{SrTiO}_3$  and the detailed shape of the DOS of the conduction ( $d$ ) band as in Fig. 2.12(b).

They further examined the spin polarisation of Co, comparing it with a junction with an  $\text{Al}_2\text{O}_3$  barrier, where the dominant conduction electrons are believed to come from the  $s$ -band. It only shows a normal bias dependence with a positive TMR.<sup>30</sup> In other words, the sign (and the magnitude) of the polarisation of Co, which has both  $s$ - and  $d$ - electrons in the conduction band, is largely determined by the interfacial chemical bonding so the choice of the barrier can serve to add a further degree of freedom to construct the SPT junctions, i.e. interfacial conduction band structure engineering. Sharma *et al.* pointed out that the inverted TMR also depends on the barrier oxidation time (thus the barrier thickness) and it might be related to different decay lengths of evanescent waves of conduction electrons of different characters as proposed in the theoretical works by MacLaren *et al.*<sup>31</sup>



(a)



(b)

**Fig. 2.12. (a)** TMR as a function of the applied bias for Co/SrTiO<sub>3</sub>/La<sub>0.7</sub>Sr<sub>0.3</sub>MnO<sub>3</sub> junctions (the top Co layer is grown by sputtering and molecular beam epitaxy for sample 1 and sample 2). The inset is the normal TMR for a bias of 1.15V. **(b)** Relative positions of the *d* DOS in Co and La<sub>0.7</sub>Sr<sub>0.3</sub>MnO<sub>3</sub> for a bias of (a) 0V, (b) -0.4V and (c) +1.15V. The arrows indicate the route of higher tunnelling rate which occurs between majority states of La<sub>0.7</sub>Sr<sub>0.3</sub>MnO<sub>3</sub> and minority states of Co in the antiparallel configuration [(a) and (b)] or between majority states of La<sub>0.7</sub>Sr<sub>0.3</sub>MnO<sub>3</sub> and majority states of Co in the parallel configuration (After Ref. [29].)

### 2.1.5 Spin polarised tunnelling based on half-metallic manganites

Ever since the discovery of colossal magnetoresistance<sup>19</sup> in the mixed valence manganites in 1994, there has been intensive world-wide interest these materials in the condensed matter community. The research into spin polarised tunnel junctions based on manganites was initially motivated by utilizing the intrinsically high spin polarisation of the materials. In the beginning the development of tunnel junctions based on manganites were mainly initiated by researchers in IBM Laboratories. These trilayer oxide junctions are epitaxial heterostructures grown on single crystal substrates by pulsed laser deposition (PLD) systems and thus more stringent prerequisites, such as the epitaxial heterostructures and the choice of the barriers, are required. The first successful demonstration of TMR was realized in micron-scale  $\text{La}_{0.7}\text{Sr}_{0.3}\text{MnO}_3/\text{SrTiO}_3/\text{La}_{0.7}\text{Sr}_{0.3}\text{MnO}_3$  junctions (Lu *et al.*<sup>32</sup> and Sun *et al.*<sup>33</sup>) in 1996, where they reported up to 80-100% TMR (to 40-50% by TMR [II]) at 4.2K. Although they were only measurable at low temperatures, those values were indeed far greater than the performances (30-40%) reported from junctions based on elemental ferromagnets – see Fig. 2.13.

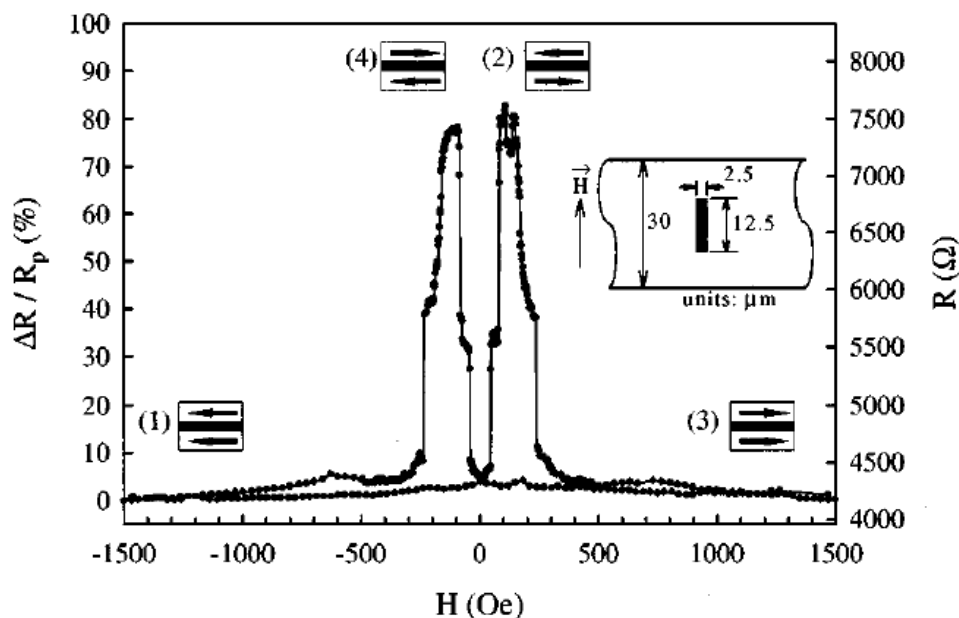


**Fig. 2.13.** TMR and junction resistance of a  $\text{La}_{0.7}\text{Sr}_{0.3}\text{MnO}_3/\text{SrTiO}_3/\text{La}_{0.7}\text{Sr}_{0.3}\text{MnO}_3$  junction at 4.2 K with a rectangular  $2.5 \times 12.5 \mu\text{m}^2$  top electrode. The field is applied along the easy axis of the top electrode. (After Ref. [32].)

In 1997, Viret *et al.*<sup>34</sup> reported a larger TMR in LSMO based junctions employing several barriers such as SrTiO<sub>3</sub>, PrBa<sub>2</sub>Cu<sub>2.8</sub>Ga<sub>0.2</sub>O<sub>7</sub> and CeO<sub>2</sub>, although they failed to show a distinct switching between the parallel and anti-parallel resistance states. Although the IBM group continued to enhance the TMR to over few hundred %, the junction performance was unstable and not routinely reproducible, and they attributed this to interfacial particulates<sup>35</sup> (see Fig. 2.14), i.e. the high energy PLD process involves some particle (10-100nm) formation on the film surface, due to randomly ablated parties from the target. Sun *et al.* claimed that the local high density of such particles can dominate the total conduction of the junction and it can often cause a unstable spin-current induced magnetic switching<sup>36</sup> by spin-momentum transfer, which can account for their observed interfacial instability.

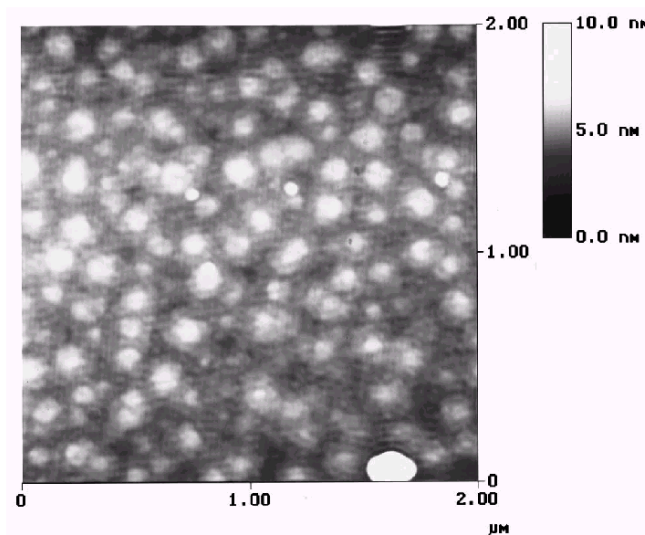


**Fig. 2.14.** AFM surface image of a typical La<sub>0.7</sub>Sr<sub>0.3</sub>MnO<sub>3</sub> film grown by PLD in IBM showing a three dimensional island growth with particulates (typical density = 10<sup>6</sup>/cm<sup>3</sup>). (After Ref. [35].)

Nevertheless, the effort to make better heteroepitaxial manganites junctions, i.e. employing other barrier materials or an alternative film growth methods such as molecular beam epitaxy (MBE) has continuously improved the junction performances. Obata *et al.*<sup>37</sup> demonstrated a TMR of 150% at 5K in La<sub>0.8</sub>Sr<sub>0.2</sub>MnO<sub>3</sub>/SrTiO<sub>3</sub>/La<sub>0.8</sub>Sr<sub>0.2</sub>MnO<sub>3</sub> as shown in Fig. 2.15 and O'Donnell *et al.*<sup>38</sup> showed a TMR of 450% at 14K in a MBE grown La<sub>0.7</sub>Sr<sub>0.3</sub>MnO<sub>3</sub>/CaTiO<sub>3</sub>/La<sub>0.7</sub>Sr<sub>0.3</sub>MnO<sub>3</sub> junction.

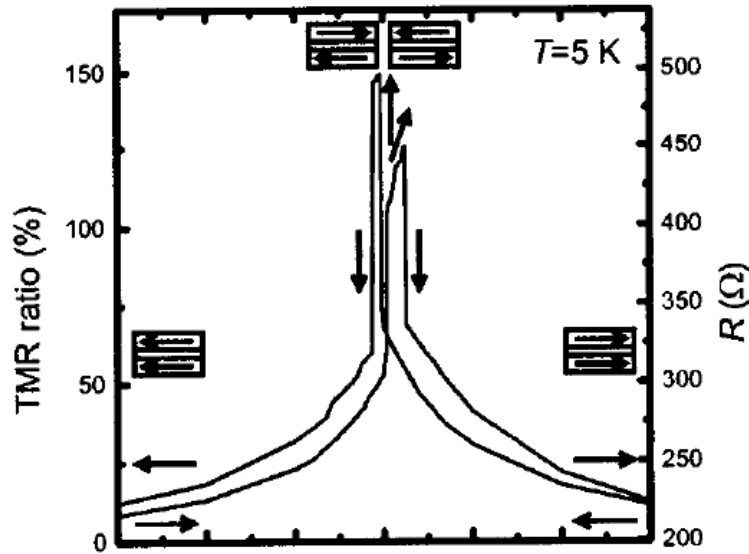


**Fig. 2.15.** TMR and junction resistance of a  $\text{La}_{0.8}\text{Sr}_{0.2}\text{MnO}_3/\text{SrTiO}_3/\text{La}_{0.8}\text{Sr}_{0.2}\text{MnO}_3$  junction at 5 K with a rectangular  $5 \times 30 \mu\text{m}^2$  top electrode. (After Ref. [37].)

Although the tunnel junctions based on manganites demonstrated a large TMR effect, which is, in a sense, natural considering their half metallic nature, there are several common features worth mentioning. First the temperature dependence of the TMR is rather disappointing in that the TMR falls off rapidly with increasing temperature even well below  $T_C$  as seen, for example, in Fig. 2.16. Note that the  $T_C$  for the bottom  $\text{La}_{0.7}\text{Sr}_{0.3}\text{MnO}_3$  electrode is  $\sim 350\text{K}$ . Secondly, for such a large TMR effect, the field sensitivity of junction switching between the parallel and anti-parallel magnetizations:  $R^{-1}(dR/dH)$ , where  $R$  is the junction resistance and  $H$  is applied magnetic field, were rather small indicating that complex domain reversal processes might be involved. Lastly the TMR value itself even at the lowest temperature is rather small considering the full polarisation of materials, which would have led an infinite TMR.

There are many studies devoted to explain the issues addressed above, particularly the temperature dependence. Here several specific arguments for the manganites junctions are selectively summarized as follows.

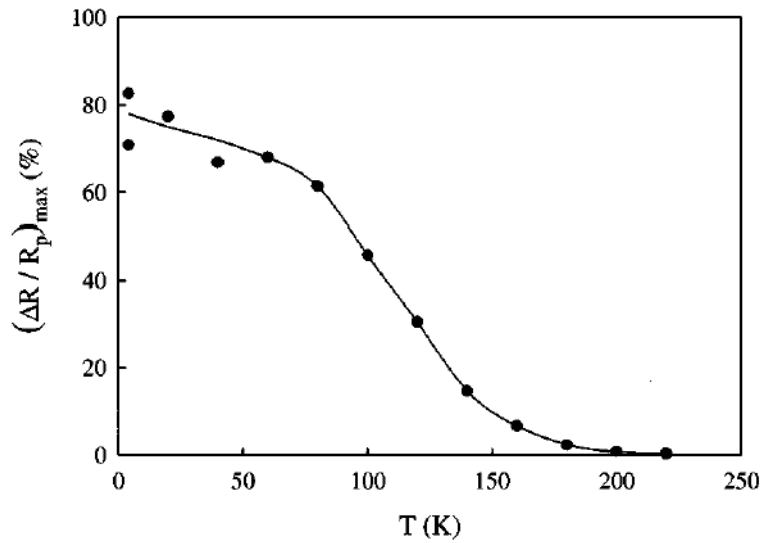


**Fig. 2.16.** Temperature dependent TMR from the junction in Fig. 2.13. Note that the  $T_C$  of the  $\text{La}_{0.7}\text{Sr}_{0.3}\text{MnO}_3$  electrode is  $\sim 350\text{K}$ . (After Ref. [32].)

It seems that in the oxide barrier junctions there is commonly a thermally activated shunting resistance via defective states in the oxide barrier, particularly at high temperatures. In fact, rough calculations of the  $\text{SrTiO}_3$  barrier heights from fitting experimental data yield much lower values, 0.5-0.7eV (Sun *et al.*<sup>39</sup>) and 0.1-0.2eV (Obata *et al.*<sup>37</sup>) compared with the known value of  $\sim 3\text{eV}$ . Sun *et al.*<sup>40</sup> suggested the existence of “magnetic dead layers” of  $\sim 5\text{nm}$  at the interfaces from their systematic resistivity measurements of plain films of different thickness. This can again find its origin in structural imperfections and can account for the low TMR and its temperature dependence. Viret *et al.*<sup>34</sup> suggested a spin-canted interface due to oxygen deficiency to explain the intermediate resistance maxima. Sun *et al.*<sup>35</sup> also observed a cusp near the zero bias limit in the  $J$ - $V$  characteristics at low temperatures, which is similar to the junctions based on elemental ferromagnets. However the energy scale involved was unusually high and they proposed the existence of metallic clusters of 1-2nm in size at the interfaces. Although the nature of features on this kind of microscopic length scale is not well understood, it can be related to a localization of charge carriers in the manganites itself rather than interfacial effects.

As discussed above the manganites tunnel junctions show more complex features than metallic tunnel junctions and clearly a full physical understanding is lacking.

In Table 2.1 the main features of the development of such junctions to date were summarized, including the work of this dissertation.

Table 2.2 Major features of the magnetic tunnel junctions with half-metallic oxides.

<b>Junction Systems</b>	<b>TMR</b>	<b>H<sub>c</sub></b>	<b>T<sub>c</sub></b>	<b>T<sub>off</sub></b>	<b>Researchers</b>
LSMO/STO/LSMO, <sup>32</sup> STO (3-6 nm), 2x12 $\mu$ m	83% at 4.2K	~100Oe	350K	200K	Brown U. and IBM, '96
LSMO/STO/LSMO, <sup>33</sup> STO (5 nm), 3x5.5 $\mu$ m	100% at 4.2K	200Oe	350K	200K	IBM, '96
LSMO/STO/LSMO, <sup>39</sup> STO (3-5 nm), 1x2 $\mu$ m	400% at 4.2K	200Oe	350K	200K	IBM, '97
LSMO/STO/LSMO, <sup>34</sup> STO (3 nm), 6x6 $\mu$ m	450% at 4.2K	~100Oe	350K	150K	CNRS, '97
LSMO/STO/LSMO, <sup>41</sup> ramp edge junction	23% at 100K	~300Oe	350K	300K	Los Alamos Nat' Lab., '98
LSMO/STO/LSMO, <sup>35</sup> STO (3-6 nm), 2x8 $\mu$ m	870% at 14K	~100Oe	350K	300K	IBM, '98
*LSMO/STO/*LSMO, <sup>37</sup> STO (1.6 nm), 5x30 $\mu$ m	150% <sup>2)</sup> at 5K	10Oe	290K	300K	NEC, '99
LSMO/CTO/LSMO, <sup>38</sup> CTO (2-3 nm), 70x50 $\mu$ m	450% at 14K	200Oe	360K	250K	U. of Illinios, '00
<b>LCMO/NGO/ LCMO,<sup>42</sup></b> <b>NGO (3-5 nm), 6x6<math>\mu</math>m</b>	<b>630%</b> <b>at 77K</b>	<b>~200Oe</b>	<b>260K</b>	<b>170K</b>	<b>U. of Cambridge, '00</b>

TMR is defined as  $TMR = (R_{ap} - R_p)/R_p$

LSMO; La<sub>0.67</sub>Sr<sub>0.33</sub>MnO<sub>3</sub>, \*LSMO; La<sub>0.8</sub>Sr<sub>0.2</sub>MnO<sub>3</sub>, STO; SrTiO<sub>3</sub>, CTO; CaTiO<sub>3</sub>, NGO ; NdGaO<sub>3</sub>

T<sub>c</sub> = Curie temperature, H<sub>c</sub> = switching field, T<sub>off</sub> = the temperature at which the TMR disappears

1) Verwey transition at 120 K and calculated polarisation is 40 %.

2) persists up to 290 K (2 %)

---

**REFERENCES**

- 
- <sup>1</sup> For a review, see “Principles of electron tunnelling spectroscopy”, E.L. Wolf, Oxford University Press (1989).
- <sup>2</sup> J.R. Oppenheimer, *Phys. Rev.* **31**, 66 (1928).
- <sup>3</sup> J. Bardeen, *Phys. Rev. Lett.* **6**, 57 (1961).
- <sup>4</sup> J.G. Simmons, *J. Appl. Phys.* **34**, 238, 1793, 2581 (1963) and **35**, 2655 (1964).
- <sup>5</sup> R. Stratton, *J. Phys. Chem. Solids* **23**, 1177 (1962).
- <sup>6</sup> J.M. Rowell and W.L. McMillan and W.L. Feldman, *Phys. Rev.* **178**, 897 (1969).
- <sup>7</sup> D. C. Worledge and T. H. Geballe, *Phys. Rev. Lett.* **85**, 5182 (2000).
- <sup>8</sup> I.I. Mazin, *Phys. Rev. Lett.* **83**, 1427 (1999).
- <sup>9</sup> For a review, see R. Meservey and P. M. Tedrow, *Phys. Rep.* **238**, 173 (1994).
- <sup>10</sup> M. Jullière, *Phys. Lett. A*, **54**, 225 (1975).
- <sup>11</sup> S. Maekawa and D. Gäfvert, *IEEE Trans. Magn.* **18**, 707 (1982).
- <sup>12</sup> R. Kabani, J.S. Moodera, R. Meservey and P. M. Tedrow, *MRS Proc. Symp.* **B**, 177 (1990).
- <sup>13</sup> J. Nowak and J. Rauluszkiewicz, *J. Magn. Magn. Mater.* **109**, 79 (1992).
- <sup>14</sup> T. Yaoi, S. Ishiro, T. Miyajaki, *J. Magn. Magn. Mater.* **126**, 430 (1993).
- <sup>15</sup> J.S. Moodera, L.R. Kinder, T.M. Wong, R. Meservey, *Phys. Rev. Lett.* **74**, 3273 (1995).
- <sup>16</sup> W.J. Gallagher, S.S.P. Parkin, Y. Lu, X.P. Bian, A.C. Marley, K.P. Roche, R.A. Altman, S. Rishton, C. Jahnes, T.M. Shaw and G. Xiao, *J. Appl. Phys.* **81**, 3741 (1997).
- <sup>17</sup> P. Ball, *Nature* **404**, 918 (2000) and Jo de Boeck and Gustaaf Borghs, *Physics World* **APR**, 27 (1999).
- <sup>18</sup> For a review, see W.E. Pickett and J.S. Moodera, *Physics Today* **MAY** (2001).
- <sup>19</sup> S. Jin, T.H. Tiefel, M. McCormack, R.A. Fastnach, R. Ramesh and L.H. Chien, *Science*, **264** 413 (1994) and M. McCormack, S. Jin, T. H. Tiefel, R. M. Fleming, Julia M. Phillips and R. Ramesh, *Appl. Phys. Lett.* **64**, 3045 (1994).
- <sup>20</sup> For a review, see M. Imada, A. Fujimori, and Y. Tokura, *Rev. Mod. Phys.* **70**, 1039 (1998) and J.M.D. Coey, M. Viret and S. von Molnár, *Adv. Phys.* **48**, 167 (1999).
- <sup>21</sup> J.S. Moodera, J. Nowak and R.J.M. van de Veerdonk, *Phys. Rev. Lett.* **80**, 2941 (1998).
- <sup>22</sup> Y. Lu, X.W. Li, G. Xiao, R.A. Altman, W.J. Gallagher, A. Marley, K. Roche and S.S.P. Parkin, *J. Appl. Phys.* **83**, 6515 (1998).
- <sup>23</sup> E.L. Wolf, “Principles of electron tunnelling spectroscopy”, pp. 395-408, Oxford University Press (1989).
- <sup>24</sup> S. Zhang, P.M. Levy, A.C. Marley and S.S.P. Parkin, *Phys. Rev. Lett.* **79**, 3744 (1997).
-

- 
- <sup>25</sup> A.M. Bratkovsky, *Phys. Rev. B* **56**, 2344 (1997) and *Appl. Phys. Lett.* **72**, 2334 (1998).
- <sup>26</sup> C.H. Shang, J. Nowak, R. Jansen and J.S. Moodera, *Phys.Rev. B* **58**, R2917 (1998).
- <sup>27</sup> S. Yuasa, T. Sato, E. Tamura, Y. Suzuki, H. Yamamoi, K. Ando and T. Katayama, *Europhys.Lett.* **52**, 344 (2000).
- <sup>28</sup> M. Sharma, X.W. Wang, and J.H. Nickel, *Phys. Rev. Lett.* **82**, 616 (1999).
- <sup>29</sup> J.M. De Teresa, A. Barthelemy, A. Fert, J.P. Contour, R. Lyonnet, F. Montaigne, P. Seneor and A. Vaures, *Phys. Rev. Lett.* **82**, 4288 (1999).
- <sup>30</sup> J.M. De Teresa, A. Barthelemy, A. Fert, J.P. Contour, F. Montaigne and P. Seneor, *Science* **286**, 507 (1999).
- <sup>31</sup> J.M. MacLaren, X.-G. Zhang and W.H. Butler, *Phys. Rev. B* **56**, 11827 (1997).
- <sup>32</sup> Y. Lu, X.W. Li, G.Q. Gong, G. Xiao, A. Gupta, P. Lecoeur, J.Z. Sun, Y.Y. Wang and V.P. Dravid, *Phys. Rev. B* **54**, 8357 (1996).
- <sup>33</sup> J.Z. Sun, W.J. Gallagher, P.R. Duncombe, L. Krusin-Elbaum, R.A. Altman, A. Gupta, Y. Lu, G.Q. Gong and G. Xiao, *Appl. Phys. Lett.* **69**, 3266 (1996).
- <sup>34</sup> M. Viret, M. Drouet, J. Nassar, J.P. Coutour, C. Fermon, and A. Fert, *Europhys. Lett.* **39**, 545 (1997).
- <sup>35</sup> J.Z. Sun, D.W. Abraham, K. Roche and S.S.P. Parkin, *Appl. Phys. Lett.* **73**, 1008 (1998).
- <sup>36</sup> J.Z. Sun, *J. Magn. Magn. Mater.* **202**, 157 (1999).
- <sup>37</sup> T. Obata, T. Manako, Y. Shimakawa and Y. Kubo, *Appl. Phys. Lett.* **74**, 290 (1999).
- <sup>38</sup> J. O'Donnell, A.E. Andrus, S. Oh, E.V. Collar and J.N. Eckstein, *Appl. Phys. Lett.* **76**, 1914 (2000).
- <sup>39</sup> J.Z. Sun, D.W. Abraham, R.A. Rao and C.B. Eom, *Appl. Phys. Lett.* **74**, 3017 (1999).
- <sup>40</sup> J.Z. Sun, L. Krusin-Elbaum, P. R. Duncombe, A. Gupta and R. B. Laibowitz. *Appl. Phys. Lett.* **70**, 1769 (1997).
- <sup>41</sup> C. Kwon, Q. X. Jia, Y. Fan, M. F. Hundley, D. W. Reagor, J. Y. Coulter, and D. E. Peterson, *Appl. Phys. Lett.* **72**, 486 (1998).
- <sup>42</sup> This dissertation work, M.-H. Jo, N.D. Mathur, N.K. Todd and M.G. Blamire, *Phys. Rev. B.* **61**, R14905 (2000).
-

## 2.2 Half-metallic Manganites

### 2.2.1 Historical background

The research of mixed valence manganites can be dated back to 1950 when Jonker and Van Santen<sup>1</sup> reported their works on mixed poly-crystals of  $\text{La}_{1-x}\text{Ae}_x\text{MnO}_3$ , where *Ae* is a divalent alkaline such as Ca, Sr, Ba, Pb, etc. They found ferromagnetism along with a large increase of electrical conductivity for the mixed valence ratio,  $\text{Mn}^{4+}/\text{Mn}^{3+}$  of 25-40%, particularly in the  $\text{La}_{1-x}\text{Ca}_x\text{MnO}_3$  series. Later in 1955, Wollan and Koehler<sup>2</sup> further probed diverse magnetic ground states in  $\text{La}_{1-x}\text{Ca}_x\text{MnO}_3$  as a function of  $x$  ( $0 \leq x \leq 1$ ) with X-ray and neutron diffraction: antiferromagnetism (AFM), ferromagnetism (FM) and sometimes the simultaneous occurrence of AFM and FM.

The renaissance in the field of mixed valence manganites began with the experimental observations of large magnetoresistance (MR) in the 1990's. In 1993 von Helmolt *et al.*<sup>3</sup> observed an  $\{R(7\text{T})-R(0)\}/R(0)$  of 60% at room temperature in  $\text{La}_{0.67}\text{Ba}_{0.33}\text{MnO}_3$  thin films. In the following year, Jin *et al.*<sup>4</sup> reported an MR larger of  $\{R(6\text{T})-R(0)\}/R(0)$  in excess of one thousand at 77K in a  $\text{La}_{0.67}\text{Ca}_{0.33}\text{MnO}_3$  thin film as in Fig. 2.17 and Fig. 2.18. This effect was dubbed colossal magnetoresistance (CMR) and it has led to the recent upsurge of interest in both the underlying physics and the potential applications in magnetoelectronics. The CMR is an intrinsic MR effect and is qualitatively different from the giant magnetoresistance (GMR)<sup>5</sup> effect, which comes extrinsically from the spin scattering in the synthetic structures of metallic multilayers (for example Co/Cu). Particularly in the avenue of technological application, it received intensive interest mainly because the large MR effect can be potentially realized in the low-field exploiting the high electron-polarisation of the CMR materials. The key feature in the fundamental physics of CMR was readily recognized from an intimate correlation between the magnetic phase transition and the electronic phase transition, i.e. a simultaneous paramagnetic to ferromagnetic and insulating to metallic transition near the Curie temperature ( $T_C$ ). In fact, the CMR is now known to be a result of the delicate balance between spin, charge, orbital and lattice degree of freedom, which have been exhaustively investigated along with other related collective states, e.g. charge ordering, in the condensed matter physics community with a popularity comparable to high  $T_C$  superconductors.<sup>6</sup>

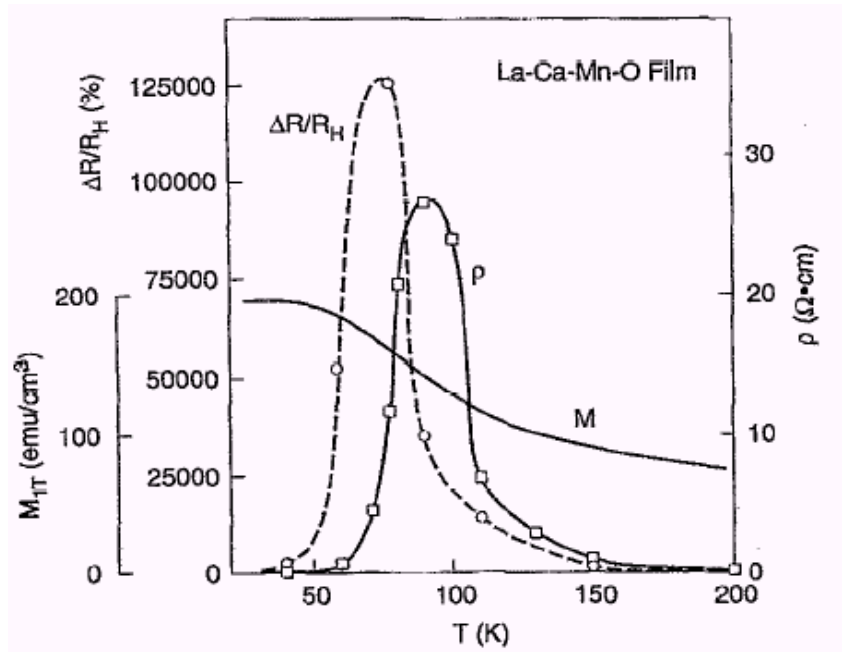


Fig. 2.17. Temperature dependent resistivity, magnetoresistance  $\{\rho(6T) - \rho(0)\}/\rho(0)$  and magnetization in a La-Ca-Mn-O<sub>3</sub> film. (After Ref. [4].)

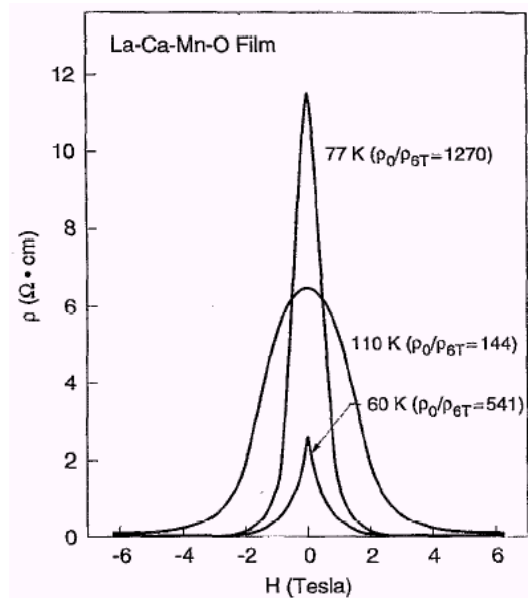


Fig. 2.18. Magnetic field dependent resistance,  $\{\rho(H) - \rho(0)\}/\rho(0)$  at various temperatures in a La-Ca-Mn-O<sub>3</sub> film. (After Ref. [4].)

## 2.2.2 Interplay among the electronic, magnetic and crystal structures<sup>7</sup>

### 2.2.2.1 Crystal and Electronic structures

Mixed valence manganites,  $Re_{1-x}Ae_xMnO_3$  where  $Re$  is a rare earth ion, are solid solutions based on  $ReMnO_3$  and  $AeMnO_3$  parent compounds. In the perovskite structure ( $ABO_3$ ), the Mn ions occupy the  $B$ -site with octahedral oxygen coordination and the  $MnO_6$  building blocks share corners to form a three-dimensional network. The interstitial  $A$ -site ions do not fit to maintain cubic symmetry for the  $MnO_6$  octahedra and this leads to lower crystal symmetry, e.g. orthorhombic, with the distortion of the octahedron as shown in Fig. 2.19. As in other perovskite materials, the fundamental electronic and magnetic features in perovskite manganites comes from the overlap between Mn-3d orbitals and O-2p orbitals which can potentially form bands.

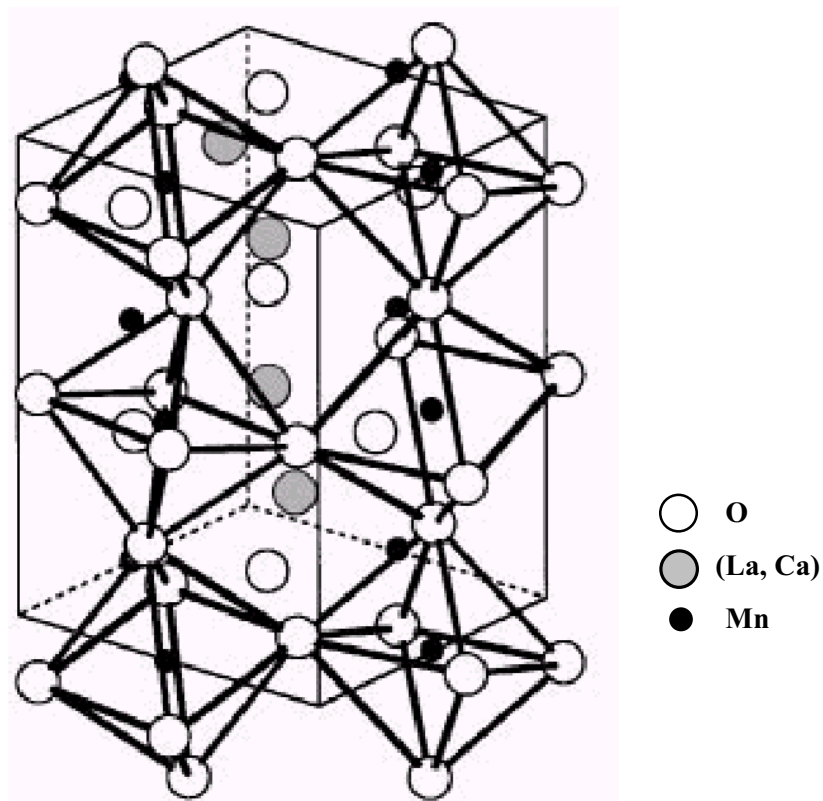
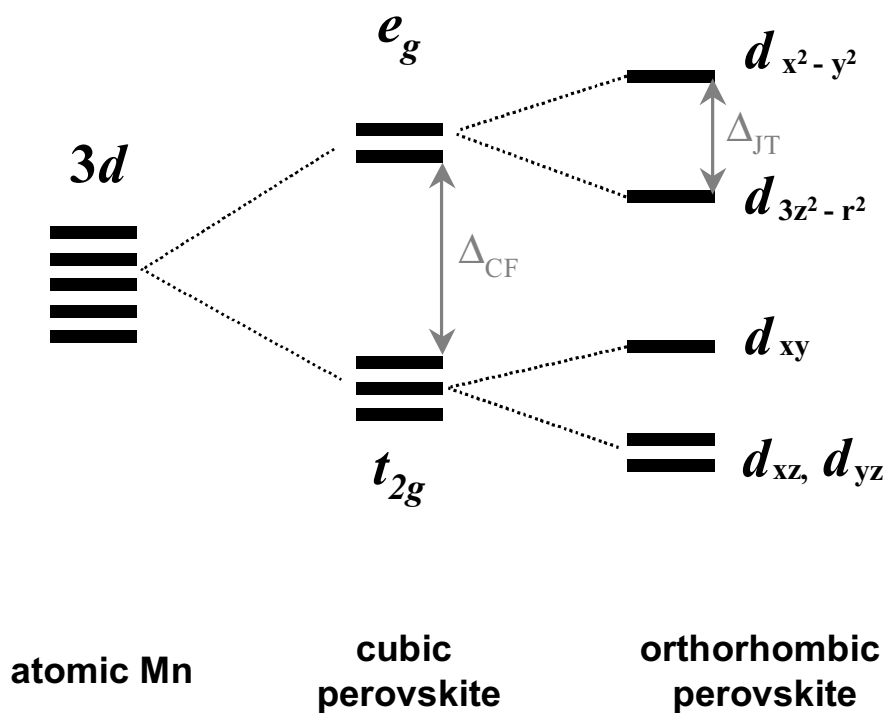


Fig. 2.19. Crystal structure of orthorhombic perovskite  $La_{1-x}Ca_xMnO_3$ . (After Ref. [6].)

The spherical symmetry of isolated Mn ions with 5-fold Mn 3d-orbitals is reduced in the octahedral surroundings of the cubic perovskite and consequently the orbital degeneracy is split by the octahedral crystal field to form lower lying triplet  $t_{2g}$  levels ( $S=3/2$ ) and higher lying doublet  $e_g$  levels ( $S=1/2$ ) as shown in Fig. 2.20. In octahedral surroundings the  $e_g$  orbitals have wave functions extending towards negatively charged  $O^{2-}$  ions and thus they experience stronger Coulomb repulsion and consequently the  $e_g$  orbitals raise their energy and are potentially itinerant compared to the localised  $t_{2g}$  orbitals. There is a further orbital degeneracy that may be lifted by the Jahn-Teller effect which will be further discussed in the section 2.2.2.3.



**Fig. 2.20.** The Mn 3d orbital levels for up-spins in different local surroundings; i.e. the same picture is repeated for down-spins at a higher energy level due to a large Hund splitting.  $\Delta_{CF}$  is the crystal field in a cubic perovskite and  $\Delta_{JT}$  is a Jahn-Teller splitting in an orthorhombic perovskite.

### 2.2.2.2 Electron-electron interactions and Magnetism

When there is one electron in each  $e_g$  orbital, i.e. at  $x = 0$  in  $\text{La}_{1-x}\text{Ae}_x\text{MnO}_3$ , the  $3d$  levels of  $\text{Mn}^{3+}$  are occupied with four electrons and double occupancy of the  $3d$  orbitals is strongly suppressed due to a large Hund coupling. The  $t_{2g}$  electrons behave as localized spins due to a weak overlap between the  $t_{2g}$  orbitals and the O-2p and the localized  $t_{2g}$  electrons interact each other due to virtual hopping onto the O-2p sites by the energy gain when their relative spin orientation is anti-parallel resulting in an indirect antiferromagnetic (AFM) order (*superexchange interaction*): the spin direction in basal planes, within which the spins are ferromagnetically aligned, are alternating along the c-axis. Meanwhile the hopping of the itinerant  $e_g$  electrons is suppressed both by the on-site Coulomb repulsion and the strong Hund coupling and consequently  $\text{LaMnO}_3$  is an antiferromagnetic insulator. In mixed valence states ( $x > 0$ ), the  $\text{Mn}^{4+}$  ions with vacant states are introduced and the  $e_g$  electrons can be potentially mobile as long as the Hund coupling is not violated. For example when the  $t_{2g}$  electron spins of  $\text{Mn}^{3+}$  and  $\text{Mn}^{4+}$  are parallel the hopping of the  $e_g$  electrons is possible at the expense of AFM interaction energy loss. Therefore the charge transfer of the conduction  $e_g$  electron between  $\text{Mn}^{3+}$  and  $\text{Mn}^{4+}$  via O ions favours and is favoured by the parallel alignment of the neighboring (localized)  $t_{2g}$  core spins and this process is named *double exchange*. As the number of  $\text{Mn}^{4+}$  increase in  $0.2 < x < 0.5$ , the kinetic energy gain of the  $e_g$  electrons overwhelms the AFM interaction and the ground state becomes a ferromagnetic metal.

The basic concept of double exchange to denote the interplay between ferromagnetism and metallicity in these material systems was first proposed by Zener<sup>8</sup> and further theoretical grounds were founded by Anderson and Hasegawa<sup>9</sup> and by De Gennes.<sup>10</sup> Large Hund coupling ( $J_H$ ) aligns the spin of the itinerant  $e_g$  electron to the core  $t_{2g}$  spin and consequently the transfer integral of the  $e_g$  electrons between neighboring Mn sites (via an intermediate quantum state involved with O ions) is modulated by the relative orientation of the core spins (see Fig. 2.21) as expressed by

$$t_{ij} \rightarrow t_{eff} = t \cos \frac{\theta_{ij}}{2} \quad \text{for } J_H/t \gg 1, \quad [2.29]$$

where  $\theta_{ij}$  is the angle between the core spins of the  $i$  and  $j$  sites. The kinetic energy of the the  $e_g$  electrons (which is proportional to  $t$ ) term is tunable by either temperature (T) or magnetic field (H).

In a simple one band model the carrier conduction can be defined by two parameters, band-filling and bandwidth ( $W$ ) as shown in Fig. 2.21. The band-filling varies according to  $x$ , and the

doping level and the bandwidth can be altered by several factors, typically electron-lattice interaction as discussed below.

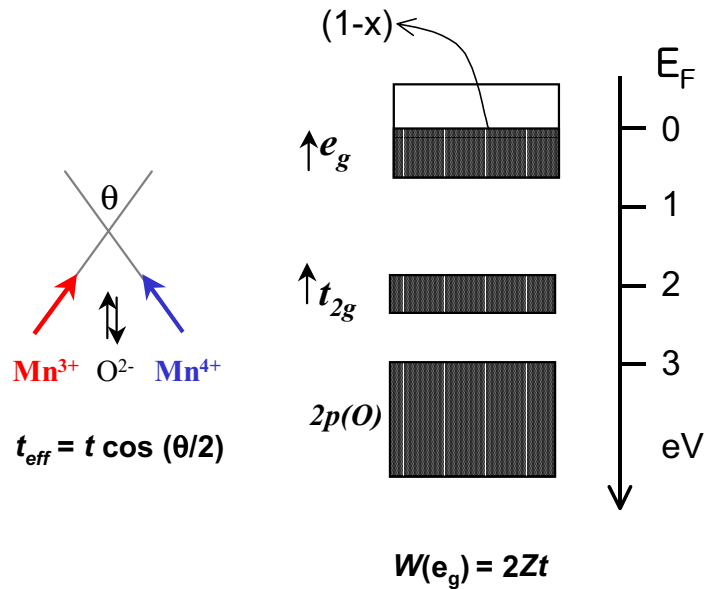


**Fig. 2.21.** Schematic diagram of the spin orientation and the hopping of an  $e_g$  electron via O ion between the neighboring  $Mn^{3+}$  and  $Mn^{4+}$  sites within the double exchange model. The transfer integral  $t_{eff}$  between the neighboring Mn sites and thus the bandwidth  $W$  is modulated by the relative orientation of the core spins within the double exchange model. (After Ref. [7].)

### 2.2.2.3 Electron-lattice interaction

The consequences of double exchange have been revisited to explain CMR in mixed valence manganites. However it has turned out to be insufficient to account for the physics of the CMR materials. Most notably within the framework of double exchange the magnitude of the resistivity of the insulating state in  $T > T_C$  is much too small to give rise the CMR effect. It has been argued that additional interactions must be involved, i.e. the electron-lattice interaction.<sup>11</sup>

There are at least two different kinds of electron-lattice interaction in manganite

perovskites arising from the crystal deformation related to  $\text{MnO}_6$  octahedra. Since the energy band originates from the overlap of the  $\text{Mn-}3d$  (the  $e_g$  orbitals) and  $\text{O-}2p$ , the hopping element of the conduction  $e_g$  electron is subject to the angle and the distance of the  $\text{Mn-O-Mn}$  bond. First the generic size difference between mixed cations, i.e.  $\text{Re}^{3+}$  and  $\text{Ae}^{2+}$  in  $\text{Re}_{1-x}\text{Ae}_x\text{MnO}_3$  introduce the buckling of the  $\text{MnO}_6$  octahedra and thus the bending of  $\text{Mn-O-Mn}$  bonding. The hopping  $e_g$  electron is sensitive to this bending and its amplitude decreases with the increase of the bending angle. The systematic change in average hopping amplitude as a function of the  $\text{Mn-O-Mn}$  bond angle by varying the average  $\text{Re}$  radius have been experimentally investigated by several groups and a typical example<sup>12</sup> is shown in Fig. 2.22.

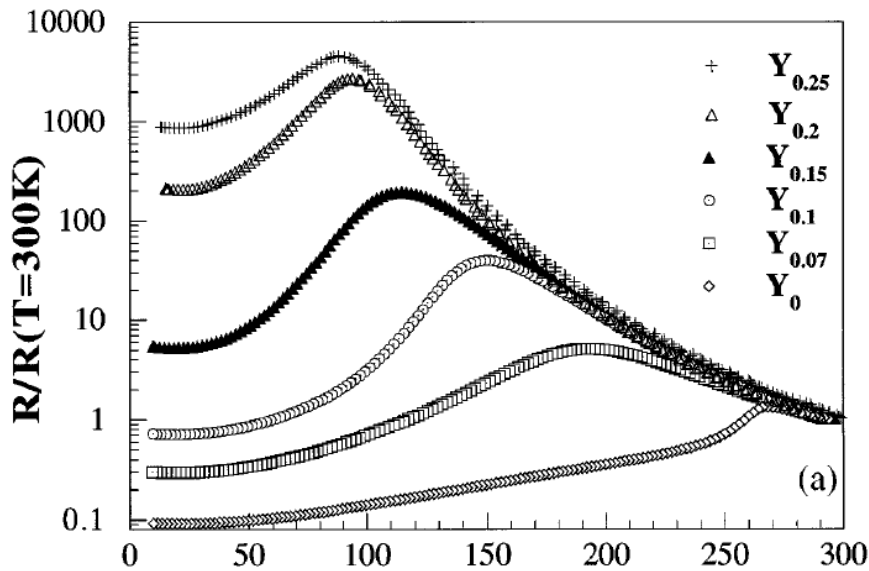


**Fig. 2.22.** Normalized resistivity,  $[R(T)/R(300\text{K})]$  of a series of samples  $\text{La}_{0.7-x}\text{Y}_x\text{Ca}_{0.3}\text{MnO}_3$  ( $x = 0, 0.07, 0.10, 0.15, 0.20,$  and  $0.25$ ) where the bond angle is further deviated from  $180^\circ$  with increasing  $x$ . (After Ref. [12].)

The other kind of electron-lattice interaction can be understood by considering the deformation of a regular octahedron, i.e. the  $\text{Mn-O}$  distances, driven by cooperative Jahn-Teller (J-T) distortion of the  $\text{Mn}^{3+}$  ion, whereas the  $\text{Mn}^{4+}$  orbital preserves the cubic symmetry environment. It can be seen that the local elongation or compression of  $\text{MnO}_6$  octahedra along their  $z$  axes gives rise to cooperative displacements in the  $x$ - $y$  plane and lifts the orbital degeneracy as schematized in Fig. 2.20.

These lattice deformations help to lower the cubic symmetry of the  $3d$  orbitals towards orthorhombic symmetry. Because an electron in a given  $e_g$  orbital causes a local lattice distortion that produces a local potential minimum, this electron-lattice interaction can localize conduction electrons. In the mixed valence state, because of the varying presence-and-absence of the J-T distortion in the  $\text{Mn}^{3+}$  and  $\text{Mn}^{4+}$  orbital, every  $e_g$  conduction hopping between  $\text{Mn}^{3+}$  and the  $\text{Mn}^{4+}$  has to carry a local J-T distortion as schematized in Fig. 2.23. Millis *et al.*<sup>11</sup> first proposed the principal role of the dynamic J-T distortion, which is temporally and spatially fluctuating, to account for insulating phases above  $T_C$  and later such a type of oxygen displacement was experimentally verified as in Fig. 2.24, where the temperature dependent variance of Mn-O bond lengths closely resembles the resistivity of corresponding compounds.

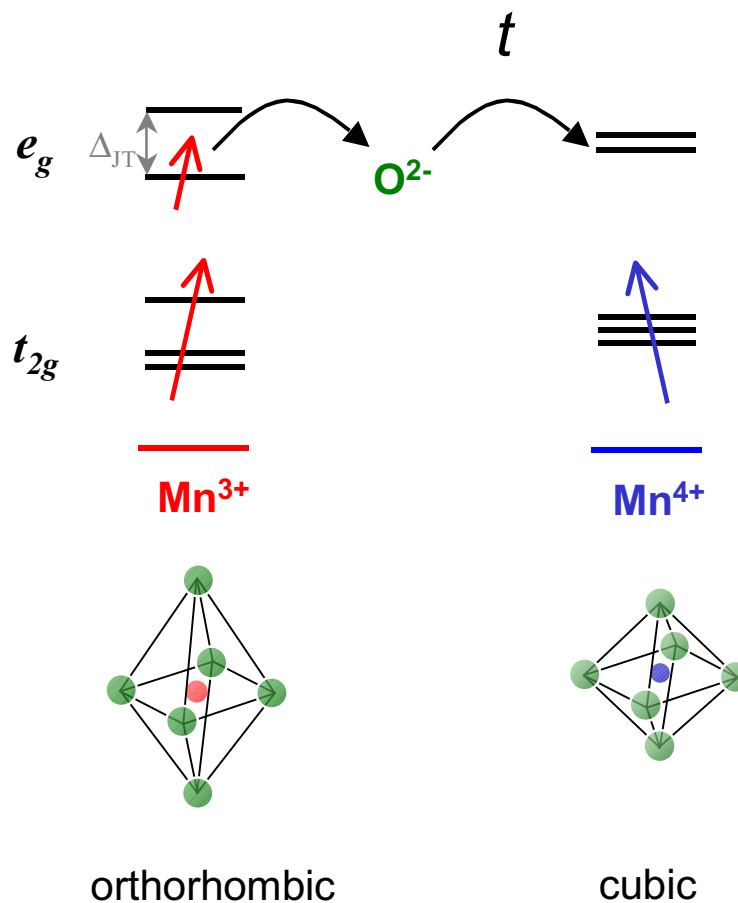


**Fig. 2.23.** Schematic diagram of the spin occupation and the hopping via an O ion between neighboring  $\text{Mn}^{3+}$  and  $\text{Mn}^{4+}$  sites in  $\text{La}_{1-x}\text{Ca}_x\text{MnO}_3$ . For an  $e_g$  electron on a  $\text{Mn}^{3+}$  site there is competition between Jahn-Teller localization and kinetic energy,  $t$ .

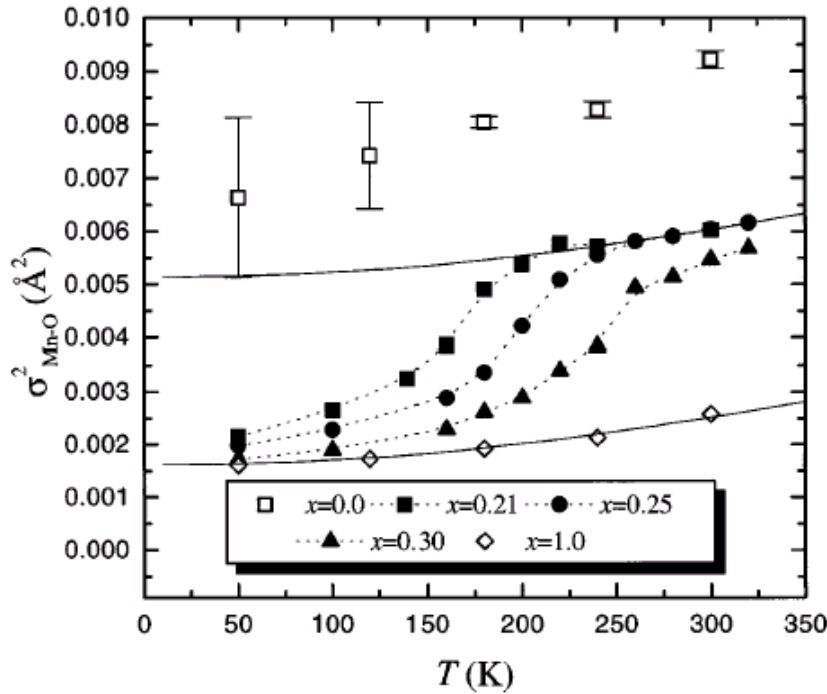


**Fig. 2.24.** Temperature dependence of variance ( $\sigma^2$ ) of Mn-O bond lengths for  $\text{La}_{1-x}\text{Ca}_x\text{MnO}_3$ . Solid lines show a fit to a correlated-Debye model ( $\Theta_D=940\text{K}$ ) for  $\text{CaMnO}_3$ . (After Ref. [13].)

More recently Rodríguez-Martínez and Attfield<sup>14</sup> investigated the dependence of the metal-insulator transition temperatures ( $T_m$ ) upon  $A$ -cation distribution, i.e. by parameterizing both the average  $A$ -cation radius  $\langle r_A \rangle$  and its variance,  $\sigma^2 = \langle r_A^2 \rangle - \langle r_A \rangle^2$  in  $AMnO_3$  manganite perovskites, where  $\langle r_A \rangle$  is related to the static distortion and  $\sigma^2$  is related to orbital order with long-range cooperative Jahn-Teller distortions. They proposed a chemical window of  $T_m$  in a phase diagram for  $x = 0.3$  of  $\text{Re}_{1-x}\text{Ae}_x\text{MnO}_3$  in the  $\langle r_A \rangle - \sigma^2$  plane and empirically estimated the maximum possible  $T_m$  of  $\sim 520\text{K}$  for an ideal perovskite,  $\langle r_A \rangle = 1.30\text{\AA}$  and  $\sigma^2 = 0$  as shown in Fig. 2.25.

In the case of thin film epitaxial manganites, this electron-lattice coupling is particularly important because the epitaxial film growth involves significant biaxial strain (either compressive or tensile) imposed from lattice-mismatch between substrates and films, which

serves as an additional source of electron-lattice coupling. An earlier theory<sup>15</sup> predicted that the effect of this types of biaxial strain is so large that a 1% biaxial strain would cause a 10% shift of  $T_C$ . In practice the lattice-mismatch between manganites films and perovskite substrates is often larger than 1% and the effect is known to be drastic not only in the shift of  $T_C$  (can vary typically from 70K to 265K depending on the substrates and the coherency of strain) and the hopping amplitude (resistivity) but also it can vary other physical properties such as magnetic anisotropy<sup>16</sup> and sometimes the ground state itself<sup>17</sup>.

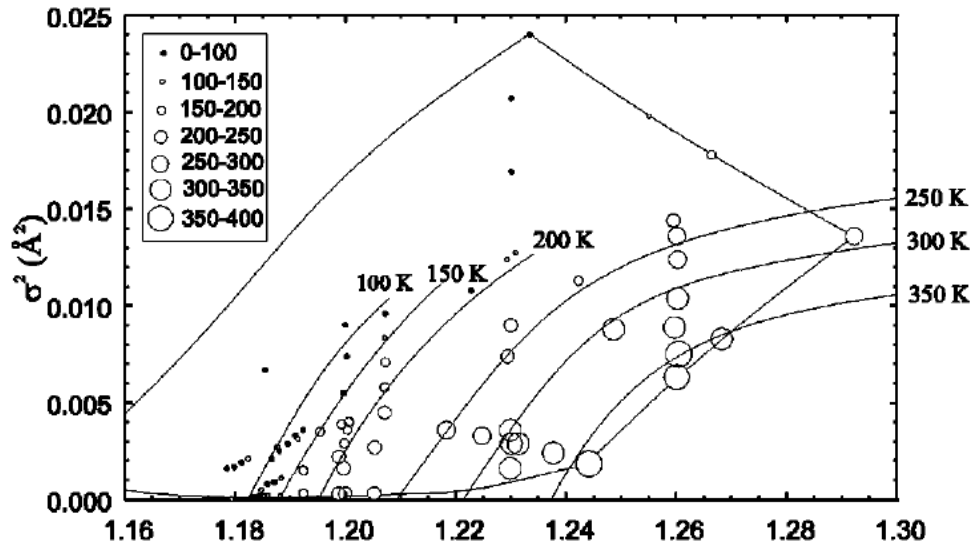


**Fig. 2.24.** Phase diagrams for  $Re_{1-x}Ae_xMnO_3$  plotted on the  $\langle r_A \rangle - \sigma^2$  plane. The bounded region shows the chemical window within which all compositions for  $Re$  one or more of La, Pr, Nd, (Pm), Sm, and  $Ae$  one or more of Ca, Sr, Ba lie. Values of the metal-insulator transition (in 50 K intervals) and approximate isotherms are shown. The ideal perovskite  $Re_{1-x}Ae_xMnO_3$  (with  $\langle r_A \rangle = 1.30 \text{ \AA}$  and  $\sigma^2 = 0$ ) lies at the bottom right corner of this plot and has estimated  $T_m \sim 520 \text{ K}$ . (After Ref. [14].)

### 2.2.3 Narrow bandwidth manganite: $\text{La}_{1-x}\text{Ca}_x\text{MnO}_3$

In the  $Re_{1-x}Ae_x\text{MnO}_3$  series, the hopping amplitude in the  $e_g$  band and thus the bandwidth can be tuned by the choice of  $Re$  and  $Ae$  cations as discussed above. Among several compounds such as  $\text{La}_{1-x}\text{Sr}_x\text{MnO}_3$ ,  $\text{La}_{1-x}\text{Ca}_x\text{MnO}_3$  and  $\text{Pr}_{1-x}\text{Ca}_x\text{MnO}_3$ , a large fraction of the work on mixed valence manganites has focused on  $\text{La}_{1-x}\text{Ca}_x\text{MnO}_3$  mainly because an intermediate bandwidth makes this compound exhibit a distinct transition between both magnetic and electronic phases, i.e. a paramagnetic insulator to a ferromagnetic metal near  $T_C$  and consequently the most noticeable CMR effect. In  $\text{La}_{1-x}\text{Sr}_x\text{MnO}_3$ , with a larger bandwidth, a transition from a paramagnetic metal to a ferromagnetic metal is often observed (more precisely it is referred as metals due to  $\partial\rho/\partial T > 0$ ) and in the  $\text{Pr}_{1-x}\text{Ca}_x\text{MnO}_3$  with a narrower bandwidth, a ferromagnetic metal phase is not easily stabilized. In this dissertation work,  $\text{La}_{1-x}\text{Ca}_x\text{MnO}_3$  is chosen as a spin polarised metal for the similar reasons.

The phase diagram as a function of  $\text{Ca}^{2+}$  doping ( $x$ ) and temperature ( $T$ ) is represented in Fig. 2.26.

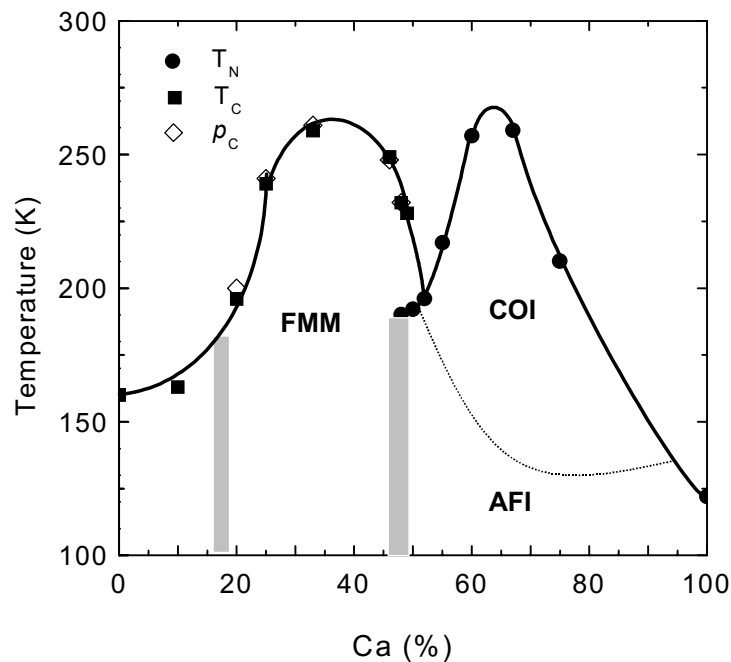


**Fig. 2.26.** Phase diagram of  $\text{La}_{1-x}\text{Ca}_x\text{MnO}_3$  as a function of doped Ca content.  $T_N$  and  $T_C$  denote Néel temperature and Curie temperature, and  $\rho_C$  denotes the resistivity peak temperature. (After Ref. [18].)

At the lower doping level of  $x < 0.2$ , it was understood that the ground state is insulating but the magnetic order evolves largely from canted antiferromagnetism to ferromagnetism although the detailed complication is yet unknown. For  $0.2 < x < 0.5$  the ground state remains metallic and ferromagnetic, and the usual CMR effect is maybe achieved. When the  $\text{Ca}^{2+}$  is further doped, for  $x > 0.5$ , the ground state is insulating and antiferromagnetic and in some cases the ordering of mixed valence states is often observed as a periodic pattern of  $\text{Mn}^{3+}/\text{Mn}^{4+}$ , which is referred to as charge ordering. For example, the charge ordering at  $x = 1/2$  or  $2/3$  shows unique stripe modulation phases consisting of regular arrays of  $\text{Mn}^{3+}/\text{Mn}^{4+}$  as seen in Fig. 2.27. However at a sufficiently high temperature ( $T > T_C$ ) for the entire doping range, the magnetic order is randomized by the entropy gain of the core spins and the system enters the paramagnetic state.

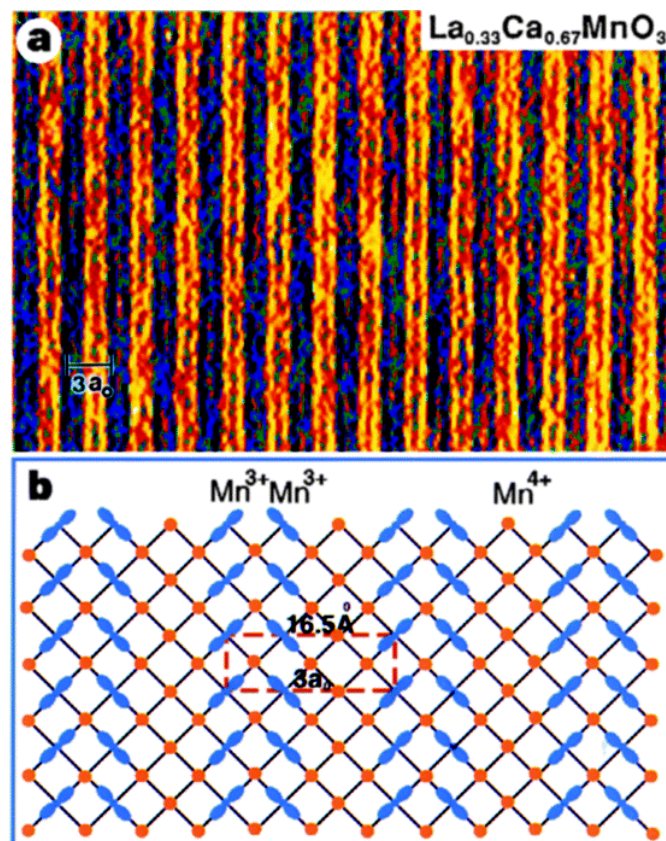


**Fig. 2.27.** Pairing of charge ordered stripes in  $\text{La}_{0.33}\text{Ca}_{0.67}\text{MnO}_3$ . **(a)** The high-resolution electron microscopy image, which shows pairing of stripes with a period of three times the lattice constant. **(b)** Schematic model of periodic ordering of  $\text{Mn}^{3+}$  and  $\text{Mn}^{4+}$  ions with the occupied  $d$  orbitals shown in blue and orange respectively. (After Ref. [19].)

### 2.2.4 Half-metallicity in manganites

In a  $d$ -band ferromagnetic metal, e.g. Ni, assuming the minimum  $s$ - $d$  band hybridization a relatively small exchange interaction ( $2\mu_H \sim 0.6\text{eV}$ ) splits a wide conduction band ( $\sim 4.5\text{eV}$ ) into the sub-bands of majority and minority carriers and thus leads to a partial spin polarisation of conduction electrons at Fermi level ( $E_F$ ). The concept of half-metallicity is where one spin sub-band completely vanishes at  $E_F$  and thus leads to a full spin polarization, as first introduced by de Groot *et al.*<sup>20</sup> from band structure calculations in Heusler alloys. In mixed valence manganites, e.g.  $\text{La}_{0.7}\text{Ae}_{0.3}\text{MnO}_3$ , a relatively narrow conduction band of typically  $\sim 1.5\text{eV}$  can be totally split due to the strong Hund coupling (typically  $\sim 2.5\text{eV}$ ), leading to a full spin polarization at  $E_F$ . See Fig. 2.28.

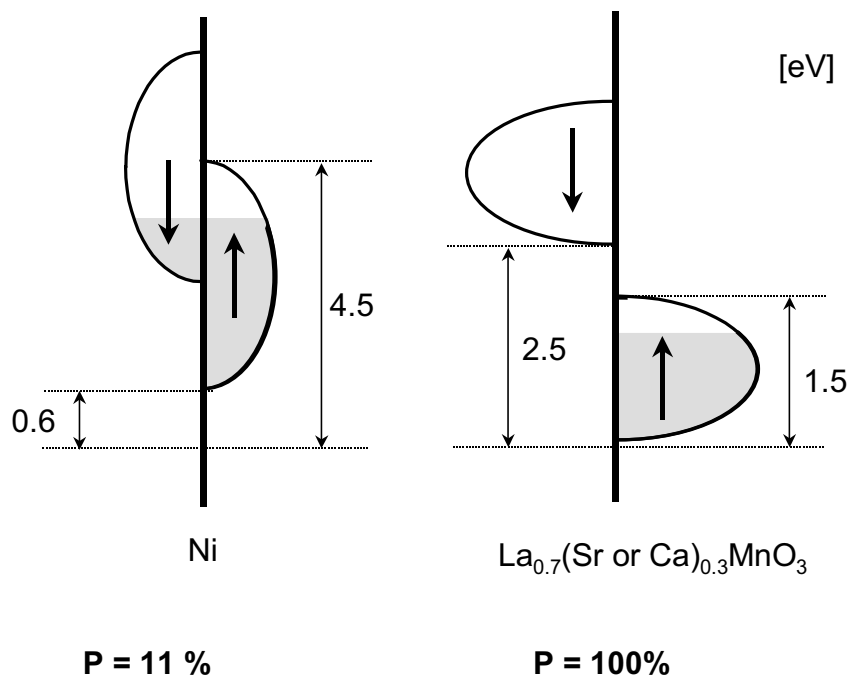


**Fig. 2.28.** Electronic density of states of Ni and  $\text{La}_{0.7}\text{Ae}_{0.33}\text{MnO}_3$  at  $T=0$  showing different degrees of spin polarization. (After Ref. [21].)

Although there are several definitions of spin polarization according to the physical quantity involved in the measurements or calculations, it seems that there is general agreement in the literature that the carriers near  $E_F$  in the optimally doped manganites are fully polarised well below the  $T_C$  as discussed below.

Full spin polarisation in the doped manganites at low temperatures is implicit in the double exchange model. In fact even in the earliest literature<sup>1</sup> the saturation magnetization of this class of materials at low temperatures was consistent with all of the Mn 3d electrons fully aligned to the same direction. Recently the half metallic nature of mixed valence manganites has been justified by more sophisticated methods, i.e. the *ab initio* band calculation on  $\text{La}_{1-x}\text{Ca}_x\text{MnO}_3$ .<sup>22</sup> Experimental measurements such as scanning tunnel spectroscopy<sup>23</sup> on  $\text{La}_{0.7}\text{Ca}_{0.3}\text{MnO}_3$  and spin-resolved photoemission<sup>24</sup> on  $\text{La}_{0.7}\text{Sr}_{0.3}\text{MnO}_3$  also confirmed the half metallicity at low temperatures. In Fig. 2.29 the spin-resolved photoemission spectrum of  $\text{La}_{0.7}\text{Sr}_{0.3}\text{MnO}_3$  for the minority carriers at 40K ( $T_C \sim 350\text{K}$ ) shows a Fermi cut-off indicating an insulating gap, while for the majority carriers the spectrum disappears near the  $E_F$  indicating no insulating gap. It shows the spin polarization is effectively 100% up to 0.4eV binding energy.

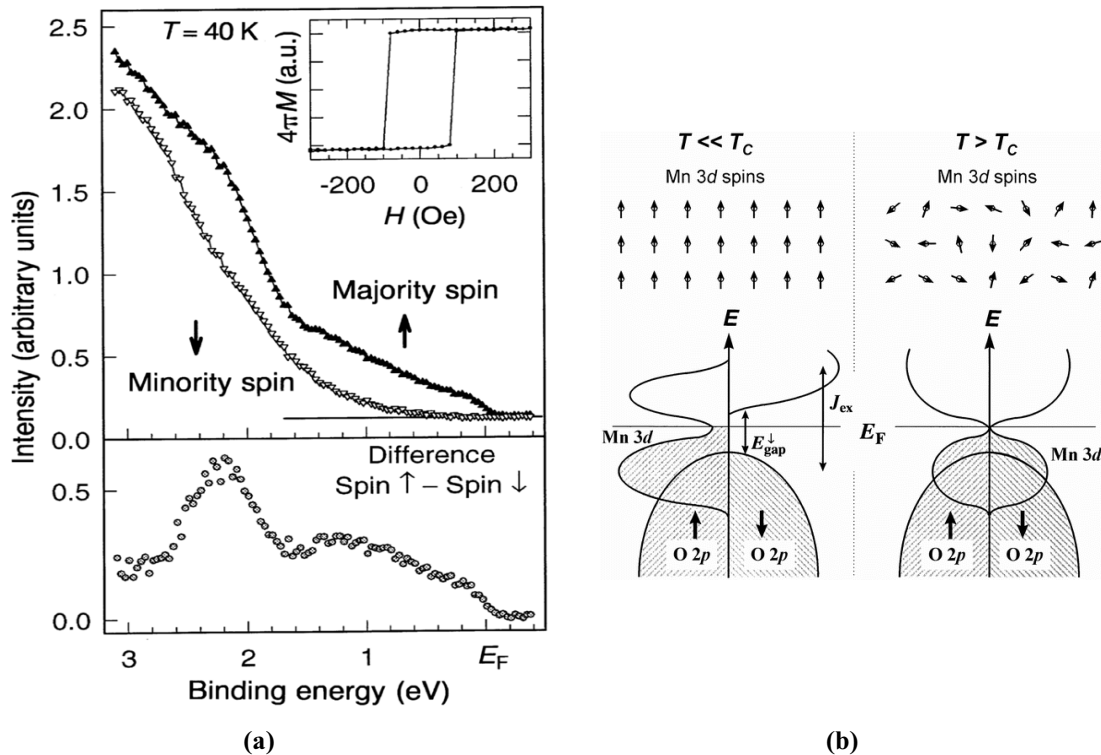


**Fig. 2.29.** (a) Spin-resolved photoemission spectra of a  $\text{La}_{0.7}\text{Sr}_{0.3}\text{MnO}_3$  thin film near the  $E_F$ . The majority ( $\uparrow$ ) and minority ( $\downarrow$ ) spins represent the spin directions parallel and anti-parallel to the magnetization direction respectively. The bottom panel shows the difference spectra between the majority-spin and the minority-spin spectra. (b) Schematic energy diagrams and the Mn 3d spin alignments at  $T \ll T_C$  and at  $T > T_C$ .  $J_{\text{ex}}$  is the Hund's rule exchange energy, and  $E_{\text{gap}\downarrow}$  denotes the insulating band-gap of the minority-spin states. (After Ref. [24].)

More quantitatively, several direct measurements (which are bound to measure a finite

value of polarisation) such as Andreev reflection point contact experiment and tunnel junctions with superconductors reported 72~78% spin polarisation in  $\text{La}_{0.7}\text{Sr}_{0.3}\text{MnO}_3$ . A compilation of spin polarization measured by the Andreev reflection experiment<sup>25</sup> is given in Fig. 2.30. By large the measured values agree fairly well from one measurement technique to another.

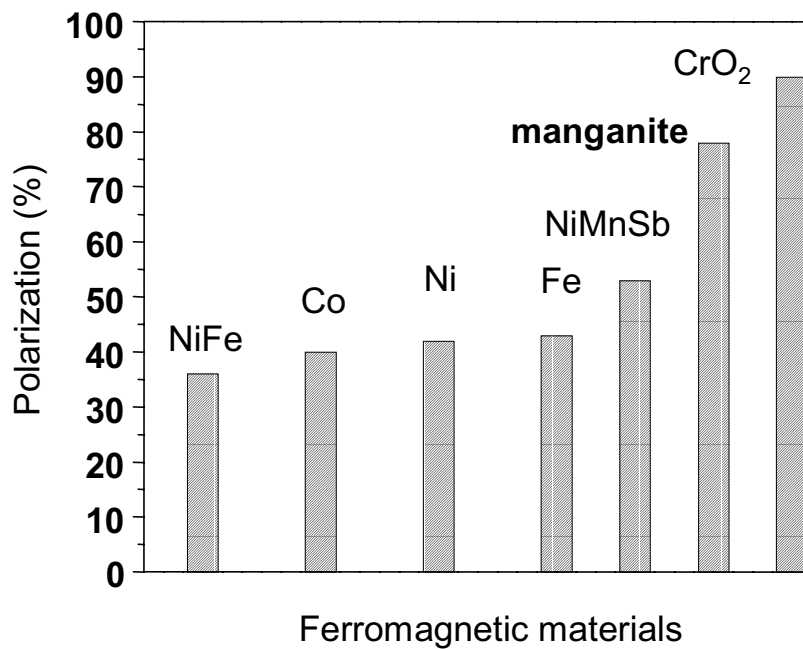


**Fig. 2.30.** Spin polarization of various ferromagnetic materials measured by Andreev reflection experiments. (After Ref. [25].)

### 2.2.5 Multi-phase coexistence

Intricate interplay among the spin, charge, orbital and lattice degrees of freedom in the mixed valence manganites make them develop various ground states, mainly a ferromagnetic metal, a charge ordered insulator and a paramagnetic insulator at different mixed valence ratios and temperatures. In recent years the question whether the spatial extent of these phases is homogeneous has been put forward from both theoretical and experimental considerations. In fact in mixed valence manganites the free energy of each distinct phase is surprisingly similar and the system may well be inhomogeneous by nature with competing multi-phases.

Among theoretical considerations at the microscopic level, Dagotto and Moreo<sup>26</sup> emphasized the key role of phase separation in the understanding of mixed valence manganites with intensive calculation studies based on several model Hamiltonians. They suggested that the ground states of the models tend to be intrinsically inhomogeneous due to the presence of strong tendencies toward phase separation, typically involving mixtures of ferromagnetic metals and antiferromagnetic (charge and orbital ordered) insulators. In their review articles on this particular subject they argued that the mixed phase tendencies have two phenomenological origins: electronic phase separation (electronic density modulation) that leads to nanometer scale phase segregation, and disorder-induced phase separation with percolative characteristics that leads to (up to) micrometer scale segregation. Mathur and Littlewood<sup>27</sup> proposed a different approach towards multi-phase coexistence by postulating a Landau theory for the various coupled order parameters (magnetism, charge-order and strain). They emphasized the role of strain in their model on multi phase coexistence and suggested the mesoscopic length scale inhomogeneity.

Experimental evidence on aforementioned phase separation is never exhaustive with omnidirectional studies such as transmission electron microscopy (TEM), scanning tunnelling spectroscopy (STS), neutron scattering, nuclear magnetic resonance (NMR) and electrical transport studies.<sup>28</sup> There is always a certain degree of controversy about the quality of the samples and the probing length scale in each experiment since any *extrinsic* physical discontinuities permitted during sample preparation and measurement can break the delicate *intrinsic* phase balance. Nevertheless, however, a variety of evidence is rapidly converging to a unanimous picture that the fundamental physical features of manganites are in practice governed by multi-phase coexistence.

*Here in this section only some evidence of the most notable observations, which have*

implications for the study of tunnel junction in the thesis work, are selectively presented for the  $La_{1-x}Ca_xMnO_3$  series among other evidence on other manganites.

Microscopic visual evidence is often most convincing and the dark field TEM images taken by Uehara *et al.*<sup>29</sup> on the  $(La_{5/8-y}Pr_y)Ca_{3/8-x}MnO_3$  series demonstrate such evidence as in Fig. 2.31. Figure 2.31(a) illustrates that the coexistence of charge-ordered (insulating) and charge-disordered (FM metallic) domains at 20 K for  $y = 0.375$  where the domain (dark area) inferred to be charge-disordered is highlighted with dotted lines for clarity. Figure 2.31(b) and (c) are obtained from the same area for  $y = 0.4$  at 17 K and 120 K and they clearly show the development of nano-scale charge-disordered domains at  $T > T_C$ .

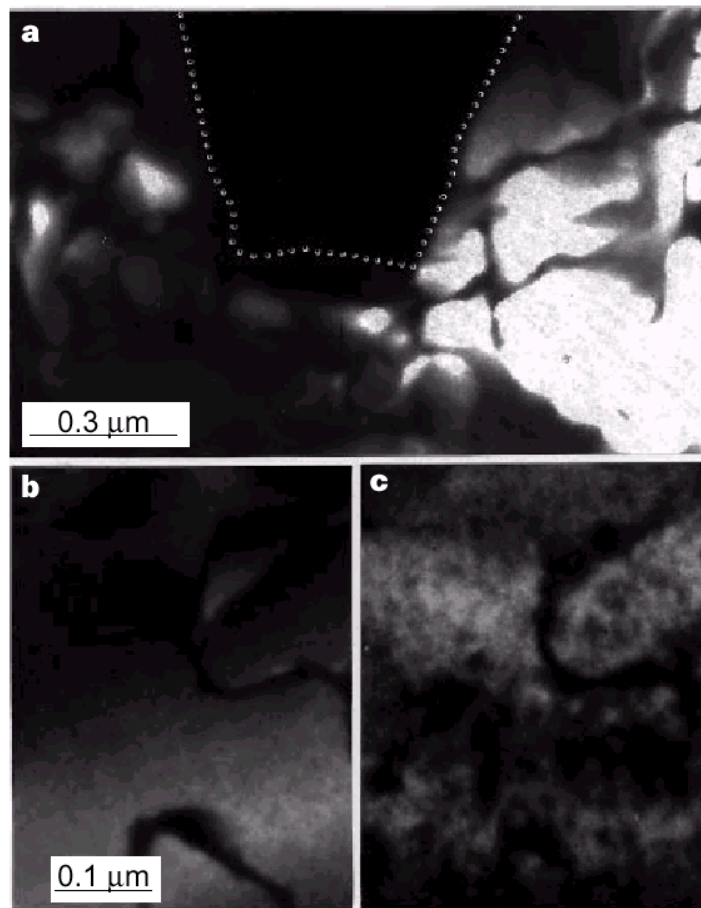


**Fig. 2.31.** (a) Dark-field images for  $La_{5/8-y}Pr_yCa_{3/8-x}MnO_3$  obtained by using a super-lattice peak caused by the  $x=1/2$ -type CO. The curved dark lines present in the CO regions are anti-phase boundaries. (b) and (c) are the images from the same area for  $y = 0.4$  at 17 K and 120 K ( $T_C \sim 45K$ ). The curved lines in (a), (b) and (c) signify the presence of antiphase boundaries of the CO domains. (After Ref. [29].)

The above observation agreed well with the corresponding transport (typically thermally hysteretic resistivity) and magnetic measurements. They proposed that the transition between the two phases when changing  $y$  or applying a magnetic field proceeds in a percolative fashion as presented in Fig. 2.32. Similar visual evidence of multi-phase characteristics was reported on the surface of  $\text{La}_{0.7}\text{Ca}_{0.3}\text{MnO}_3$  thin films from a STS study by Fäth *et al.*<sup>30</sup>, where they showed the relative volume fraction of the ferromagnetic metallic and the paramagnetic insulating clusters is dependent upon temperature ( $T < T_C$ ) and applied magnetic field. From the evidence mentioned above it seems that the length scale of phase inhomogeneity is much larger than the order of nanometer.

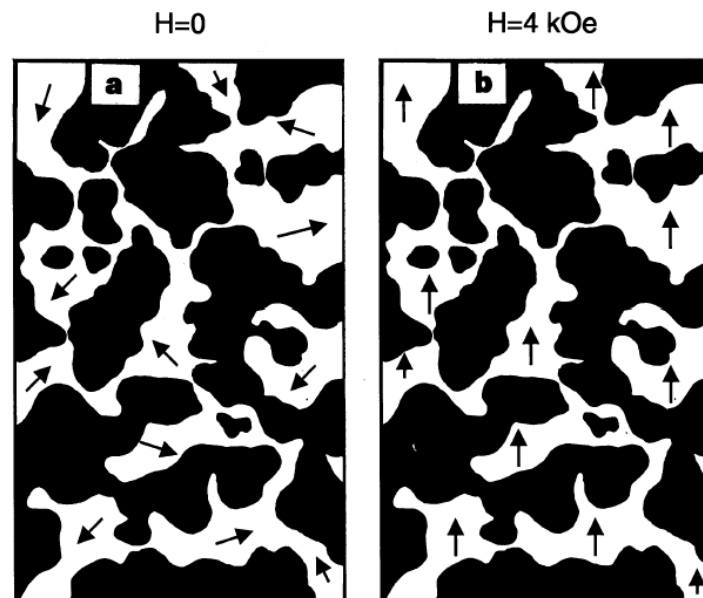


**Fig. 2.32.** Schematic illustration of the sub-micrometre-scale coexistence of the CO insulating (dark area) and FM metallic (white area) domains. The typical size of domains is  $\sim 0.5 \mu\text{m}$ . In zero field (a), the orientation of the magnetizations of FM domains are random, but all magnetizations of FM domains can be aligned by applying field of about 4 kOe (b). (After Ref. [29].)

Macroscopic evidence (as judged by the probing length scale in the experiments) is also consistently accumulating. Raquet *et al.*<sup>31</sup> reported a two-level fluctuator of resistance in a thin film  $\text{La}_{0.7}\text{Ca}_{0.3}\text{MnO}_3$  grown on  $\text{LaAlO}_3$  below  $T_C$  ( $T_C \sim 210\text{K}$ ) as shown in Fig. 2.33. They attributed the origin of this to a dynamic mixed-phase percolative conduction process, where segregated clusters switch back and forth between two different phases with the different

conductivities. Merithew *et al.*<sup>32</sup> also reported a similar resistance fluctuation in bulk and thin film  $\text{La}_{0.7}\text{Ca}_{0.3}\text{MnO}_3$  (grown on  $\text{SrTiO}_3$ ) and they further determined the size of region, which undergoes concerted fluctuation between more and less conducting, to be on the scale of microns. They found a larger size scheme in the thin film sample and suggested that the observed additional long-range order term, stabilizing larger mixed phase regimes in the film compared to the bulk sample could be due to substrate induced strain (from the lattice mismatch). The substrate-induced strain effect on multi-phase inhomogeneity was also addressed by Reutler *et al.*<sup>33</sup> from low frequency  $1/f$  noise measurements on  $\text{La}_{0.7}\text{Ca}_{0.3}\text{MnO}_3$  thin films on  $\text{NdGaO}_3$  (lattice mismatch,  $\Delta a/a \sim 0.08\%$ ) and  $\text{SrTiO}_3$  (lattice mismatch  $\sim 1.5\%$ , so highly strained). They found a significant suppression of the noise level in the resistance of the less strained film.

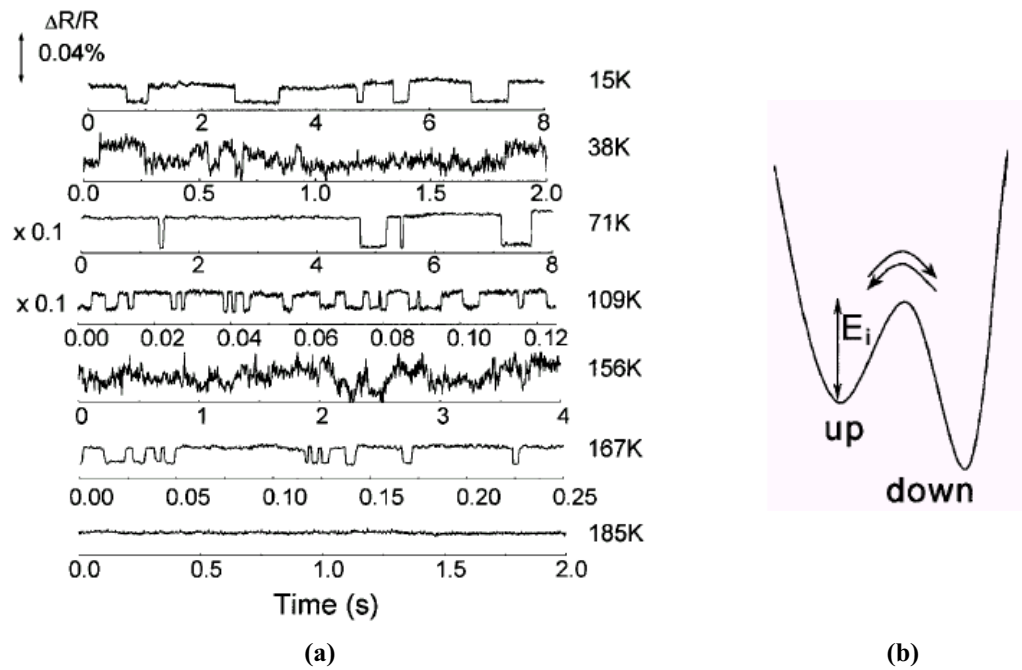


**Fig. 2.33. (a)** Resistance ( $R$ ) vs time at different temperatures in a  $\text{La}_{0.7}\text{Ca}_{0.3}\text{MnO}_3$  thin film. The noise alternates from a strongly non-Gaussian fluctuation-type to a random telegraph noise  $\Delta R$  ranging from 0.01% to 0.2%. The features observed in the traces recorded at 38 and 156 K are reminiscent of a superposition of “few” two level fluctuations processes with different characteristic lifetimes. At certain temperatures only a single fluctuator dominates, giving rise to the RTN at 15, 71, 109, and 167 K. There is no evidence for the RTN above 180 K. **(b)** Schematic representation of an asymmetric double-well model used to describe the fluctuation process. (After Ref. [31].)

Most recently Bibes *et al.*<sup>34</sup> reported a further complex mixed-phase feature in highly strained  $\text{La}_{0.7}\text{Ca}_{0.3}\text{MnO}_3$ . Figure 2.34 presents the  $^{55}\text{Mn}$  NMR experimental data measured on a series of  $\text{La}_{0.7}\text{Ca}_{0.3}\text{MnO}_3$  films on  $\text{SrTiO}_3$  varying thickness from 6 to 108 nm. A systematic NMR line deconvolution between  $\text{Mn}^{4+}$  (insulating) and  $\text{Mn}^{3+/4+}$  (metallic) peaks is observed. Further comparison with magnetization measurements suggests a third phase, a non-ferromagnetic insulator in addition to a ferromagnetic metal, a ferromagnetic insulator.

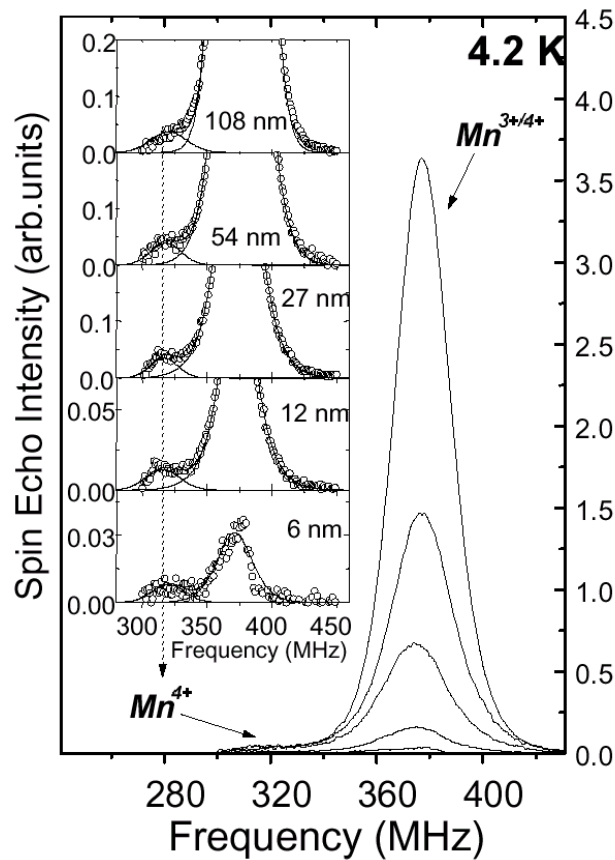


**Fig. 2.34.**  $^{55}\text{Mn}$  NMR spectra recorded for  $\text{La}_{0.7}\text{Ca}_{0.3}\text{MnO}_3$  films of varying thickness. Inset shows expanded views around the  $\text{Mn}^{4+}$  peak. (After Ref. [34].)

---

**REFERENCES**

---

- <sup>1</sup> G.H. Jonker and J.H. Van Santen, *Physica* **16**, 337 and 599 (1950).
  - <sup>2</sup> E.O. Wollen W.C. Koehler, *Phys. Rev.* **100**, 545 (1955).
  - <sup>3</sup> R. von Helmholtz, J. Singleton, D.A. Keen, R. McGreevy and K Samwer, *Phys. Rev. Lett.* **71**, 2331 (1993).
  - <sup>4</sup> S. Jin, T.H. Tiefel, M. McCormack, R.A. Fastnach, R. Ramesh and L.H. Chien, *Science* **264**, 413 (1994) and M. McCormack, S. Jin, T. H. Tiefel, R. M. Fleming, Julia M. Phillips and R. Ramesh, *Appl Phys. Lett.* **64**, 3045 (1994).
  - <sup>5</sup> M.N. Baibich, J.M. Broto, A. Fert, F. Nguyen van Dau, F. Petroff, P. Etienne, G. Creuzet, A. Friederich and J. Chazelas, *Phys. Rev. Lett.* **61**, 2472 (1988) and S. S. P. Parkin, N. More, and K. P. Roche, *Phys. Rev. Lett.* **64**, 2304 (1990).
  - <sup>6</sup> For a comprehensive review, see for example, Y. Tokura and Y. Tomioka, *J. Magn. Magn. Mater.* **200**, 1 (1999) and Y. Tokura (Ed.), *Colossal Magnetoresistive Oxides*, Gordon & Breach Science Publishers, London (1999).
  - <sup>7</sup> For a review, see for example, M. Imada, A. Fujimori, and Y. Tokura, *Rev. Mod. Phys.* **70**, 1039 (1998) and J.M.D. Coey, M. Viret and S. von Molnár, *Adv. Phys.* **48**, 167 (1999).
  - <sup>8</sup> C. Zener, *Phys. Rev.* **82**, 403 (1951).
  - <sup>9</sup> P.W. Anderson and H. Hasegawa, *Phys. Rev.* **100**, 67 (1955).
  - <sup>10</sup> P.-G. de Gennes, *Phys. Rev.* **118**, 141 (1960).
  - <sup>11</sup> A.J. Millis, P.B. Littlewood and B.I. Shraiman, *Phys. Rev. Lett.* **74** 5144 (1995) and A.J. Millis, *Nature* **392**, 147 (1998).
  - <sup>12</sup> J. Fontcuberta, B. Martínez, A. Seffar, S. Piñol, J. L. Garcia-Muñoz and X. Obradors, *Phys. Rev. Lett.* **76**, 1122 (1996).
  - <sup>13</sup> C. H. Booth, F. Bridges, G. H. Kwei, J. M. Lawrence, A. L. Cornelius, and J. J. Neumeier, *Phys. Rev. Lett.* **80**, 853 (1998).
  - <sup>14</sup> L.M. Rodríguez-Martínez and J.P. Attfield, *Phys. Rev. B* **63**, 024424 (2000) and the references therein.
  - <sup>15</sup> A.J. Millis, T. Darling and A. Migliori, *J. Appl Phys.* **83**, 1588 (1998).
  - <sup>16</sup> X. W. Wu, M. S. Rzchowski, H. S. Wang and Qi. Li, *Phys. Rev. B* **61**, 501 (2000).
  - <sup>17</sup> E. B. Nyeanchi , I. P. Krylov , X.-M. Zhu and N. Jacobs, *Europhys. Lett.* **48**, 228 (1999).
  - <sup>18</sup> P. Schiffer, A.P. Ramirez, W. Bao and S.-W. Cheong, *Phys. Rev. Lett.* **75**, 3336 (1995).
  - <sup>19</sup> S. Mori, C.H. Chen and S.-W. Cheong, *Nature* **392**, 473 (1998).
  - <sup>20</sup> R.A. de Groot, F.M. Muller, P.G. van Engen and K.H.J. Boschow, *Phys. Rev. Lett.* **50**, 2024 (1983).
-

- 
- <sup>21</sup> H.Y. Hwang, S.-W. Cheong, N.P. Ong and B. Batlogg, *Phys. Rev. Lett.* **77**, 2041 (1996).
- <sup>22</sup> E. Pickett and D.J. Singh, *Phys. Rev.* **B 53**, 1146 (1996) and the references therein, and S. Satpathy, Z.S. Popovic and F.R. Vukajlovic, *Phys. Rev. Lett.* **76**, 690 (1996).
- <sup>23</sup> J.Y.T. Wei, N.-C. Yeh and R.P. Vasquez, *Phys. Rev. Lett.* **79**, 5150 (1997).
- <sup>24</sup> J.-H. Park, C.T. Chen, S.-W. Cheong, W. Bao, G. Meigs, V. Chakarian and Y.U. Idzerda, *Phys. Rev. Lett.* **76**, 4215 (1996), J.-H. Park, E. Vescovo, H.-J. Kim, C. Kwon, R. Ramesh and T. Venkatesan, *Nature* **392**, 794 (1998) and *Phys. Rev. Lett.* **81**, 1953 (1998).
- <sup>25</sup> R.J. Soulen Jr., J.M. Byers, M.S. Osofsky, B. Nadgorny, T. Ambrose, S.F. Cheng, P.R. Broussard, C.T. Tanaka, J. Nowak, J.S. Moodera, A. Barry and J.M.D. Coey, *Science* **282**, 85 (1998).
- <sup>26</sup> A. Moreo, S. Yunoki and E. Dagotto, *Science* **283**, 2034 (1999) and E. Dagotto, T. Hotta and A. Moreo, cont-mat/0012117 and to be published in *Phys. Rep.*
- <sup>27</sup> N.D. Mathur and P.B. Littlewood, cont-mat/01024238 and to be published in *Solid State Comm.*
- <sup>28</sup> For a more comprehensive review, see for example, Ref. [25] and [26] and the references therein.
- <sup>29</sup> M. Uehara, S. Mori, C.H. Chen and S.-W. Cheong, *Nature* **399**, 560 (1999).
- <sup>30</sup> M. Fäth, S. Freisam, A.A. Menovski, Y. Tomioka, J. Aarts and J.A. Mydosh, *Science* **285**, 1540 (1999).
- <sup>31</sup> B. Raquet, A. Anane, S. Wirth, P. Xiong, and S. von Molnár, *Phys. Rev. Lett.* **84**, 4485 (2000).
- <sup>32</sup> R. D. Merithew, M. B. Weissman, F. M. Hess, P. Spradling, E. R. Nowak, J. O'Donnell, J. N. Eckstein, Y. Tokura, and Y. Tomioka, *Phys. Rev. Lett.* **84**, 3442 (2000).
- <sup>33</sup> P. Reutler, A. Bensaïd, F. Herbristrit, and C. Höfener, A. Marx and R. Gross, *Phys. Rev.* **B 62**, 11619 (2000).
- <sup>34</sup> M. Bibes, Ll. Barcells, S. Valencia, J. Fontcuberta, M. Wojcik, E. Jedryka and S. Nadolki, *Phys. Rev. Lett.*, to be published.
-

## 2.3 Magnetization processes in spin polarised tunnel junctions

Spin polarised tunnelling (SPT) exploits the dissimilar conductance of the conduction electrons between asymmetric spin sub-bands at Fermi level ( $E_F$ ). It is commonly assumed that there is a direct correlation between the bulk magnetization-vector and the spin-quantized axis of conduction electron in SPT. A full understanding of SPT should thus include the magnetization reversal process under the external magnetic field as well as the physics of electron tunnelling. If the ferromagnetic electrodes in SPT junctions are assumed to be spin sources or spin detectors, as in the Stern-Gerlach experiment of the spin-angular momentum measurement, one can find the SPT conductance as a function of the relative angle of the two magnetization-vectors.<sup>1</sup>

In this section, the basic magnetization processes such as magnetic anisotropy, domain structures and magnetization reversal in ferromagnetic thin films are selectively reviewed and their possible correlations in SPT junctions are discussed.

### 2.3.1 Magnetic energetics (Micromagnetics)

The total free energy of a ferromagnet of a finite size under a magnetic field is given by the sum of various free energy terms such as the Zeeman energy, exchange energy, anisotropy energies and magnetostatic energy as

$$E_{\text{tot}} = \int (E_{\text{Zee}} + E_{\text{ex}} + E_{\text{ani}} + E_{\text{stat}}) dV. \quad [2.30]$$

The first term, the Zeeman energy is an interaction that arises because the external field ( $\mathbf{H}$ ) interacts with the magnetization vectors ( $\mathbf{M}$ ). It is given by

$$E_{\text{Zee}} = -\mathbf{H} \cdot \mathbf{M}. \quad [2.31]$$

The second contribution, exchange energy can be given by using Heisenberg's expression:

$$E_{\text{ex}} = -2 \sum_{ij} J_{ij} \mathbf{S}_i \cdot \mathbf{S}_j, \quad [2.32]$$

where  $J_{ij}$  is the exchange constant between the two adjacent classical spins whose spin quantum number  $\mathbf{S}_i$  and  $\mathbf{S}_j$  at  $i$  and  $j$  sites. The crystalline anisotropy energy is due to spin-orbit coupling and depends on the direction of magnetization relative to the crystal axes. Lastly, magnetostatic energy, which comes from the self-energy created by free magnetic poles, is dependent on the shape and the size of the sample and thus leads to an additional anisotropy. The micromagnetics, a continuum theory of magnetic moments following the conditions of the total energy minimization, can describe magnetic microstructures such as the magnetization direction including their dynamic features, and domain formation.

In epitaxial thin film ferromagnets, where the crystallinity, size and shape of the sample are uniquely defined, the magnetic anisotropy plays a particularly significant role in the magnetization processes as well as the domain structures that will be discussed later.

## 2.3.2 Magnetic anisotropy

### 2.3.2.1 Crystalline anisotropy

The exchange interaction between neighboring spins, which is the origin of the spontaneous magnetization ( $\mathbf{M}$ ) in ferromagnetism, is in principle isotropic. In a given crystalline structure, the exchange interaction couples with the anisotropic crystal field (more precisely ligand field) of a crystalline ion – spin-orbit interaction –, resulting in the tendency of the spontaneous magnetization to lie along certain crystallographic axes. It is known as crystalline anisotropy and in general it exhibits a similar symmetry to the crystal symmetry. The tendency for the magnetization to lie along the easy axis can be quantitatively described using the crystalline anisotropy constant  $K_i$ . For example Co is hexagonal and the easy axis is uniaxial along the hexagonal c-axis. The anisotropy density ( $E_K$ ) can thus be given by

$$E_K = K_1 \sin^2 \theta + K_2 \sin^4 \theta + \dots \quad [2.33]$$

where the higher order terms of the expansion are usually very small and their values are not readily known ( $K_1 = 4.1 \times 10^6$  erg/cm<sup>3</sup>,  $K_2 = 4.1 \times 10^6$  erg/cm<sup>3</sup> for Co at room temperature). In the case of cubic symmetry, e.g. Fe, the cube edges are the easy axes and the anisotropy energy is

given by

$$E_K = K_1(\cos^2\theta_1\cos^2\theta_2 + \cos^2\theta_2\cos^2\theta_3 + \cos^2\theta_3\cos^2\theta_1) + K_2(\cos^2\theta_1\cos^2\theta_2\cos^2\theta_3) + \dots \quad [2.34]$$

where  $\cos\theta_i$  is the direction cosine with respect to the cube edges ( $K_1 = 4.7 \times 10^5 \text{ erg/cm}^3$ ,  $K_2 = -0.075 \times 10^5 \text{ erg/cm}^3$  for Fe at room temperature). In the cubic symmetry the sign of  $K_1$  determines whether the [100] or [111] directions are the easy axes, e.g. for Ni,  $K_1 = -5.7 \times 10^4 \text{ erg/cm}^3$ ,  $K_2 = -2.3 \times 10^4 \text{ erg/cm}^3$  at room temperature and the easy axis is along [111].

Consequently the crystalline anisotropy is particularly important when the sample is both a single crystal and a single domain; otherwise the magnetization is mainly dependent on other factors such as domain structures or shape anisotropy as discussed below. In this thesis work where the SPT junctions are based on single crystal manganites, the crystal anisotropy play a crucial role in magnetization processes.

### 2.3.2.2 Induced anisotropy

Induced anisotropy is due to extrinsic factors such as the magnetic surroundings and the size or shape of a magnetic object. Strictly speaking it is a question of asymmetric magnetostatic energy. However in the case of thin film specimens of finite size and anisotropic dimensions, its contribution to the total magnetic energy can be significant.

#### *Shape anisotropy*

When a sample of finite size is magnetized by an external field, the free magnetic poles at the ends produce an internal magnetic field directed opposite to the magnetization (i.e. a demagnetization field,  $H_d$ ), to minimize magnetostatic energy. The intensity of the demagnetization field, which is a function of the free pole density and the sample shape, can be calculated from the integral of the product of the pole density and the potential over the sample, the potential being that generated by the magnetization. In practice, it can be written as a function of the uniform magnetization as

$$H_d = \mathbf{D} \cdot \mathbf{M}, \quad [2.35]$$

where the term  $\mathbf{D}$  is called the demagnetization factor and for several simple geometries it can be calculated analytically. A thin film sample is often approximated as an oblate ellipsoid with two (in-plane) long axes  $a$  and  $b$  of the same order of magnitude and much greater than the short axis  $c$  (thickness) as in Fig. 2.33.

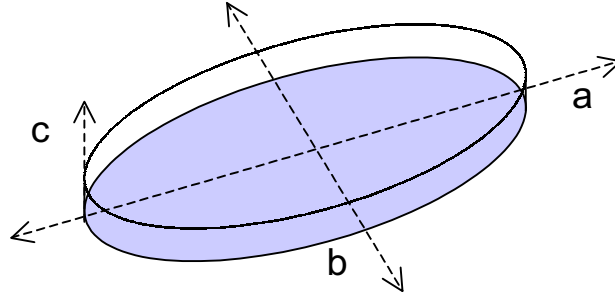


**Fig. 2.33.** An oblate ellipsoid with Cartesian axes taken to coincide with magnetic principal axes.

The demagnetization factors<sup>2</sup> are given by

$$D_a = \pi^2 \frac{c}{a} \left[ 1 - \frac{1}{4} \frac{(a-b)}{a} - \frac{3}{16} \left( \frac{a-b}{a} \right)^2 \right],$$

$$D_b = \pi^2 \frac{c}{a} \left[ 1 + \frac{5}{4} \frac{(a-b)}{a} - \frac{21}{16} \left( \frac{a-b}{a} \right)^2 \right],$$

$$D_c = 4\pi, \quad [2.36]$$

where the large  $D_c$  imposes a strong in-plane anisotropy. The tendency towards demagnetization to minimize stray field is facilitated by the formation of multi-domains and it will be further discussed in the next section along with a notion of a single domain.

#### *Exchange bias anisotropy*

When there is magnetic inhomogeneity within a magnetic sample, e.g. the coexistence of ferromagnetic (FM) and antiferromagnetic (AFM) domains, it often causes an asymmetrical magnetization hysteresis that is manifested in a coercivity enhancement due to the interfacial interaction between the FM and the AFM regions. This phenomenon, first discovered in Co(FM) - CoO(AFM) mixtures in 1956<sup>3</sup>, has attracted wide interest for applications in magnetic recording heads<sup>4</sup> and the SPT junctions<sup>5</sup> because it can stabilize the FM domains and further help to engineer the coercivity of the FM. Although up to now the detailed physics of exchange bias lacks a thorough understanding, the basic phenomenological principles are well known as follows.<sup>6</sup>

Consider a bilayer composed of a FM layer and an AFM layer. An exchange bias can be

qualitatively understood by assuming an (ferromagnetic) exchange interaction at the interface between the FM and the AFM. When the bilayer is cooled to  $T < T_N < T_C$  in the presence of a field, due to the interaction at the interface, the sub-lattice of the AFM interfacial spins adjacent to the FM align parallel to the spins of the FM, while the inner bulk spins of the AFM maintain AFM order (Fig. 2.34(ii)). When the reversed field rotates the FM spins, the AFM spins remain unchanged when the AFM anisotropy sufficiently large (Fig. 2.34(iii)). Therefore, the AFM spins at the interface exert a microscopic torque on the FM spins, to keep them in their original position (Fig. 2.34(iii)) and thus, the extra field is needed to reverse completely an FM layer to overcome the microscopic torque (Fig. 2.34(v)). The extra (internal) biasing field at the interface in one-direction causes the FM hysteresis loop to be shifted along the field axis and the resultant anisotropy is strongly “unidirectional”.

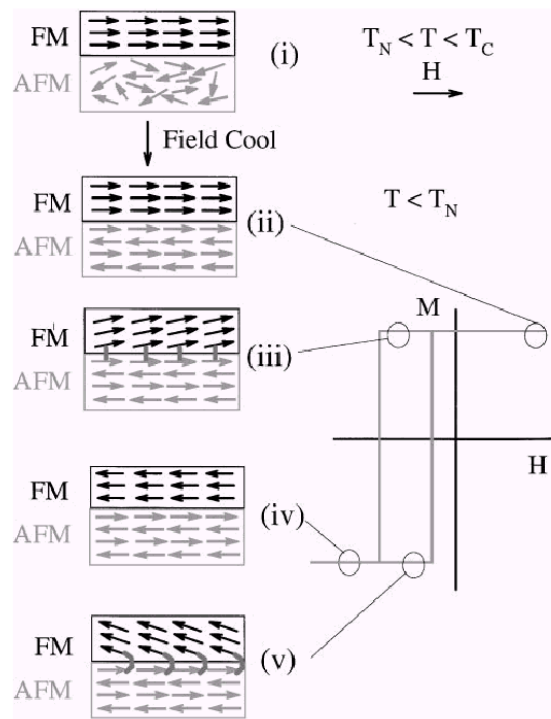


**Fig. 2.34.** Schematic representation of exchange bias in the FM-AFM bilayers. The spin configuration at each stage referred to the corresponding hysteresis loop. Note that this simple cartoon is not necessarily an accurate portrait of the actual rotation of the FM or AFM magnetizations. (After Ref. [6].)

### 2.3.3 Domains and Domain walls

The magnetization of a ferromagnetic sample at well below  $T_C$  is typically broken into several localized regions, namely domains, within each of which the magnetization is homogeneous. The concept of domains was proposed long ago in order to explain various magnetic phenomena and it is not limited to ferromagnetic materials, e.g. the theory applied to ferroelectric and superconducting materials. In 1935 Landau and Lifshitz<sup>7</sup> showed that a microscopic domain structure in a ferromagnetic material could be described by the minimization of the total energy that is a sum of various energy terms such as exchange interaction, anisotropy and magnetostatic energy – see, Eq. [2.30].

Between the adjacent domains the spin direction does not in general change discontinuously but rather there is a gradual change within the same plane over a certain spatial extension (for Fe typically over 300 unit cells). This transient boundary is called a Bloch wall or usually a domain wall. The domain wall energy can be expressed as the sum of the (Heisenberg) exchange energy (treated classically) and the anisotropy as

$$E = \left( \frac{\pi^2 JS^2}{la} \right) + Kl, \quad [2.37]$$

where  $J$  is the exchange constant,  $S$  is the spin quantum number,  $l$  is the wall width,  $K$  is the anisotropy constant and  $a$  is the cubic lattice constant. The energy minimization,  $\partial E/\partial l$  then determines the width of a Bloch wall to be,

$$l = \left( \frac{\pi^2 JS^2}{Ka} \right)^{1/2}. \quad [2.38]$$

The exchange constant  $J$  is usually difficult to get and Eq. [2.38] is often useful in empirically determining  $J$  for a given ferromagnet, when other parameters are well known.

If a ferromagnetic sample is in very thin, the Bloch wall configuration causes a large demagnetization normal to the film surface and then the spins within the wall tend to align parallel to the film surface resulting in another type of domain wall so called Néel wall.

### 2.3.4 Magnetization reversal of a single domain: Coherent rotation

Magnetization reversal processes are usually discussed within the framework of magnetic domain structures and include domain wall motion and domain wall nucleation. In fact domain wall motion can facilitate the magnetization reversal process under an applied field, because within the wall the delicate balance between the exchange and the anisotropy energies can be easily destroyed. However under the certain circumstances a ferromagnetic sample may consist of a single domain. A typical example can be found when a sample is magnetized to saturation with a sufficiently large field or when a sample is so small that the magnetization is uniformly homogeneous throughout, even without an external field. The latter is the main subject of further discussion of the section.

The magnetization process of such a single domain under the influence of an external magnetic field is unique in that magnetization reversal occurs via coherent rotation at a critical field without any domain wall motion. Coherent magnetization reversal in a small ferromagnetic object was first studied by Stoner and Wohlfarth<sup>8</sup> in 1948. In their simplified model study of an ellipsoid with a uniaxial anisotropy, they showed that the critical value of the normalized field ( $h$ ) required for magnetization reversal, where the magnetization jumps discontinuously, depends on the angle between the field and the easy axis as in Fig. 2.35.

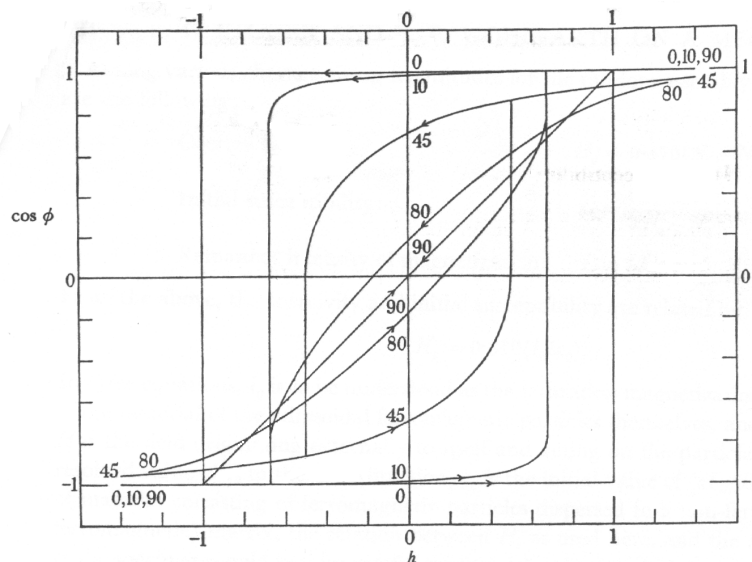


**Fig. 2.35.** The calculated M-H loops as a function of the angle between the field and the easy axis in the single domain of a prolate spheroid. (After Ref. [8].)

Later Slonczewski proposed a geometrical expression of the same problem in the two dimensional plane formed by the orthogonal easy and hard axis with the field direction as the main variable. It is known as the critical asteroid curve.<sup>9</sup> Recently Thiaville<sup>10</sup> explored further theoretical consideration in more complex anisotropy and in a three-dimensional case. Recent experimental observations of a microscopic ferromagnetic object were reported to be consistent with the models.<sup>11</sup> The basic features of such critical asteroid curves can be summarized as follows.

The uniform magnetization ( $\mathbf{M}$ ) of a small ferromagnet in a magnetic field,  $\mathbf{H}$  is given in the relation of

$$E_{\text{tot}}(\mathbf{H}) = -\mathbf{H} \cdot \mathbf{M} + E_K(\theta), \quad [2.39]$$

and in a static equilibrium the magnetization direction is governed by the minimum energy condition of  $\partial E / \partial \theta = 0$  and  $\partial^2 E / \partial \theta^2 > 0$ , where  $E_{\text{tot}}$  is the total magnetic energy density,  $\theta$  is the relative orientation of magnetization as in Fig. 2.36, and  $E_K$  is the anisotropy energy density. In the case of uniaxial anisotropy, the anisotropy energy to a simple second order is given by

$$E_K(\theta) = -K \cdot \sin^2(\theta). \quad [2.40]$$

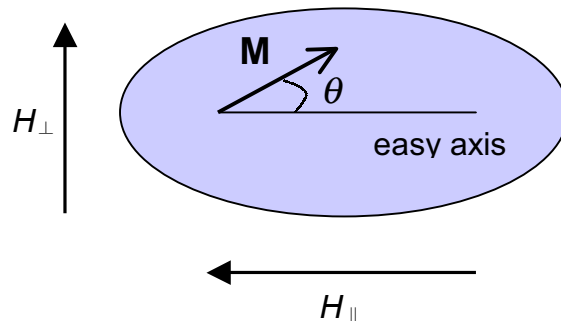


**Fig. 2.36.** An ellipsoidal, uniaxial particle in an external magnetic field that has been decomposed into parallel and perpendicular (with the easy axis) components.

Eq. [2.39] can be rewritten with the reduced field components as

$$E_{\text{tot}}(\mathbf{H}) = -(H_{\parallel} M \cos \theta + H_{\perp} M \sin \theta) - K \cdot \sin^2(\theta) \quad [2.41]$$

where  $H_{\parallel}$  and  $H_{\perp}$  are the parallel and perpendicular components of the field. The discontinuous jump of magnetization occurs at

$$\partial E / \partial \theta = H_{\parallel} M \sin \theta - H_{\perp} M \cos \theta + 2K \sin(\theta) \cos(\theta) = 0 \quad [2.42]$$

and

$$\partial^2 E / \partial \theta^2 = H_{\parallel} M \cos \theta + H_{\perp} M \sin \theta + 2K \{ \cos^2(\theta) - \sin^2(\theta) \} = 0. \quad [2.43]$$

When the normalized critical field,  $h$  (the switching field) is defined as

$$h = \left( \frac{HM}{2K} \right), \quad [2.44]$$

combining Eq. [2.42] and Eq. [2.43] gives a set of solutions of the  $\{H_{\parallel}(\theta), H_{\perp}(\theta)\}$ :

$$h_{\parallel}(\theta) = -\cos^3(\theta) \text{ and } h_{\perp}(\theta) = \sin^3(\theta), \quad [2.45]$$

and they satisfy an asteroid curve of

$$\{h_{\parallel}(\theta)\}^{2/3} + \{h_{\perp}(\theta)\}^{2/3} = 1 \quad [2.46]$$

as shown in Fig. 2.37.

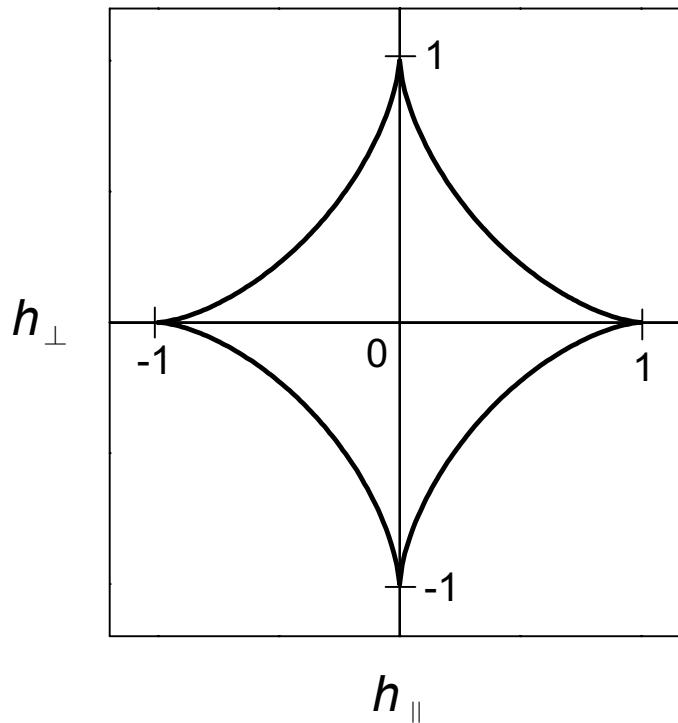


**Fig. 2.37.** An critical asteroid curve of a single domain particle described in Fig. 2.36. When the external field crosses the boundary, discontinuous magnetization reversal occurs.

In principle the same rationale can be applied to the systems where the anisotropy contains

---

higher order terms or is more complicated, as long as the differential equations are analytically soluble.<sup>12</sup>

Experimentally such asteroid curves can be constructed by magnetic measurements performed using two orthogonal fields or angular measurements. The deviation from the ideal asteroid can be discussed to include other effects beyond the coherent rotation.<sup>13</sup>

---

**REFERENCES**

- 
- <sup>1</sup> For example, see J.C. Slonczewski, *Phys. Rev.* **B 39**, 6995 (1989).
- <sup>2</sup> D. Craik, *Magnetism: Principles and Applications*, pp. 92-95, John Wiley and Sons, Chichester (1997).
- <sup>3</sup> W.H. Meiklejohn and C.P. Bean, *Phys. Rev.* **102**, 1413 (1956).
- <sup>4</sup> B. Dieny, V.S. Speriosu, S.S.P. Parkin, B.A. Gurney, D.R. Wilhoit and D. Mauri, *Phys. Rev.* **B 43**, 1297 (1991).
- <sup>5</sup> W.J. Gallagher, S.S.P. Parkin, Y. Lu, X.P. Bian, A.C. Marley, K.P. Roche, R.A. Altman, S. Rishton, C. Jahnes, T.M. Shaw and G. Xiao, *J. Appl. Phys.* **81**, 3741 (1997).
- <sup>6</sup> J Nogués and Ivan K. Schuller, *J. Mag. Mag. Mater.* **192**, 203 (1999).
- <sup>7</sup> L.D. Landau and E. Lifshitz, *Phy. Z. Sowjetunion* **8**, 153 (1935).
- <sup>8</sup> E.C. Stoner and E.P. Wohlfarth, *Phil. Trans. Roy. Soc. A* **240**, 599 (1948).
- <sup>9</sup> J.C. Slonczewski, Research Memo No. 003.111.224, IBM Research Center, Poughkeepsie, NY (1956) (unpublished).
- <sup>10</sup> A. Thiaville, *J. Mag. Mag. Mater.* **182**, 5 (1998).
- <sup>11</sup> O. Fruchart, J.-P. Nozieres, W. Werndorfer, D. Givord, F. Rousseaux and D. Decanini, *Phys. Rev. Lett.* **82**, 1305 (1999) and E. Bonet, W. Werndorfer, B. Babara, A. Benoit, D. Mailey and A. Thiaville, *Phys. Rev. Lett.* **83**, 4188 (1999).
- <sup>12</sup> C.-R. Chang, *J. Appl. Phys.* **69**, 2431 (1991).
- <sup>13</sup> Y. Lu, P. L. Trouilloud, D.W. Abraham, R. Koch, J. Slonczewski, S. Brown, J. Bucchignano, E. O'Sullivan, R.A. Wanner, W.J. Gallagher and S.S.P. Parkin, *J. Appl. Phys.* **85**, 5267 (1999) and A. Anguelouch, B. D. Schrag, Gang Xiao, Yu Lu, P. L. Trouilloud, R. A. Wanner, W. J. Gallagher, and S. S. P. Parkin, *Appl. Phys. Lett.* **76**, 622 (2000).
-

---

## CHAPTER 3

# Experimental Methods

---

### 3.1 Deposition of heteroepitaxial structures

#### *Pulsed laser deposition*

Heteroepitaxial oxide-film growth in the dissertation work was carried out with a pulsed laser deposition (PLD) method. The PLD is a non-equilibrium thin film growth from the plasma plume ablated from the stoichiometric target by a high power laser radiation. The most unique characteristics of the PLD may be the decoupling of the evaporation power source and the high vacuum component unlikely in other vacuum deposition processes. Thus in general it is a very simple and low-cost process. More importantly in the PLD, the stoichiometry of the target can be easily retained in the deposited films. This is mainly the result of the extremely high heating rate of the target surface ( $10^8\text{K/s}$ ) at the laser ablation, which leads to the congruent evaporation of the target irrespective of the evaporating point of the constituent elements or compounds of the target. It is thus very flexible for the choice of versatile materials growth, ranging from elemental metals to complex multi-components oxides. Particularly it has been widely adopted for the prototypical growth of new materials or complex materials such as such as high  $T_C$  superconductors and mixed valence manganites. Nevertheless the PLD also has some disadvantages: one major drawback is the micron sized particulates deposited on the film surface from a splashing from the target and another shortcoming is a narrow angular distribution of the plume, which limits its use in the thin film growth with a large area uniformity.

Figure 3.1 shows a schematic feature of the PLD set-up in this study. The KrF laser (248nm excimer laser) is focused onto rotating targets (the maximum six targets can be

---

accommodated). The substrate sits on the heater (the Fe-Cr-Al alloy foil) underneath the plume generated from the laser irradiation. The target-substrate distance was maintained to 4cm.

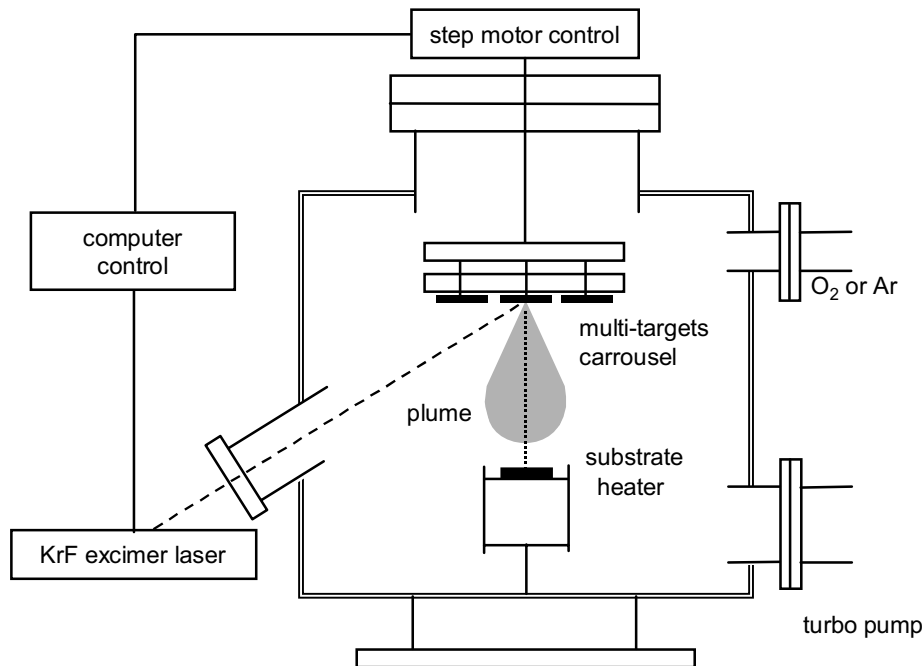


**Fig. 3.1.** A schematic feature of the PLD system in the study.

Contrary to the simplicity of the system set-up, the physical principle of the PLD is a rather complex involving the physical process of the laser-target interaction as well as the chemical and thermodynamic processes such as

- (1) the plasma plume formation of highly energetic atomic species,
- (2) the transfer of the ablated species to the substrate,
- (3) the nucleation on the substrate surface.

#### *Heteroepitaxy and Tunnel barriers*

The prerequisites for the growth of the heteroepitaxial trilayer, which would be subsequently micro-fabricated into tunnel devices, are extremely stringent. First of all, the

perfect heteroepitaxy should be established throughout the multilayers to preserve the bulk-like half-metallicity of the manganite films to the very interfaces, which tends to couple to local crystal deformation due to lattice-mismatch with the barriers or the substrates. Secondly, but most importantly, the tunnel barrier must be well defined in the atomic scale: typically in the junction geometry in this study, the (oxide) barriers of 3-5 nm thickness with the lateral uniformity (of few  $\mu\text{m}$  order) must be established with minimum defects and impurities. The heteroepitaxial film growth was then optimized to mainly meet those two criteria. Although all stages in the film growth of (1) – (3), the film nucleation stage is particularly important for *the layer-by-layer growth*, which can ensure both the crystallinity and the atomically smooth interfaces. In the early stage of the thesis work, much of the time and efforts were devoted to meet the requirements. The typical parameters for the optimum heteroepitaxial film growth are summarized in Table 3.1.

Table 3.1 Typical parameters for the optimum heteroepitaxial film growth.

Stages	Substrate Temperature	Background Gas	Laser	Duration	ETC
substrate cleaning	Ultrasound cleaning in acetone (SrTiO <sub>3</sub> or NdGaO <sub>3</sub> )				
pre-annealing	~700 °C	vacumm*	.	60min	.
		O <sub>2</sub> 15kPa		10min	
deposition	~700 °C	O <sub>2</sub> 15kPa	<ul style="list-style-type: none"> <li>· pulse rate: 1Hz</li> <li>· beam density: 2-3 J/cm<sup>2</sup></li> <li>· no laser intermittence between layers</li> </ul>	deposition rate: 0.23Å/pulse	layer-by-layer growth
post-annealing	~700 °C	O <sub>2</sub> 50kPa	.	60min	.
cooling	.	O <sub>2</sub> 50kPa	.	40min	rapid cooling

\*Base pressure  $\sim 3 \times 10^{-7}$  mbar.

### 3.2 Device Microfabrication

The microfabrication of tunnel junctions devices from the bare multilayers is processed with a four-masks process in the Group's clean room. The masks are designed to produce 10 micron-scale mesa junctions ( $6\times 6$ ,  $8\times 8$ ,  $8\times 16$  and  $20\times 30\mu\text{m}^2$ ) per chip using AutoCAD<sup>TM</sup>. The microfabrication involves a conventional UV photolithography, ion milling, silica insulation and Au metallization. A typical process for the junction fabrication is schematically illustrated in Fig. 3.2.

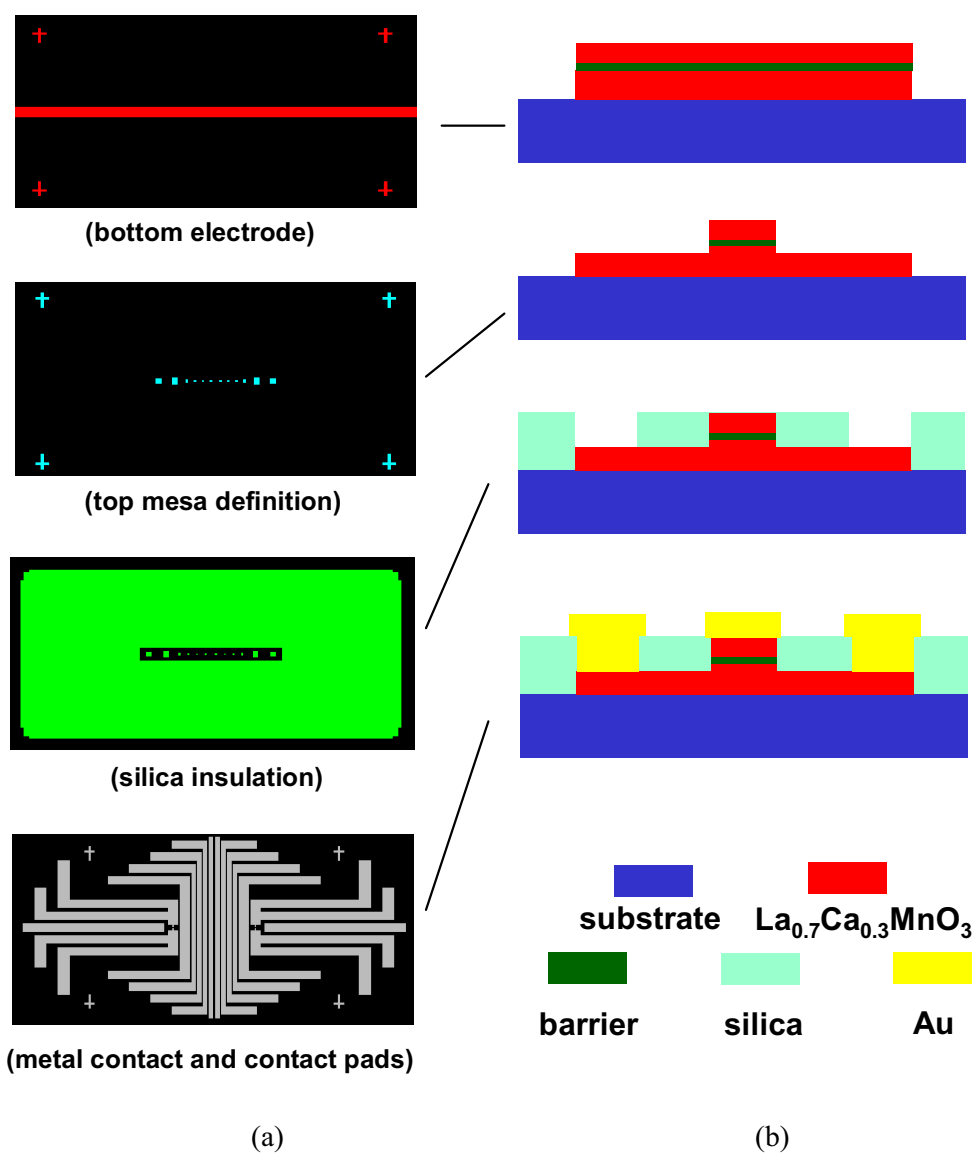


**Fig. 3.2.** (a) The four-masks used in the microfabrication process for the tunnel junction devices and (b) the schematic cross-sectional view of the junction.

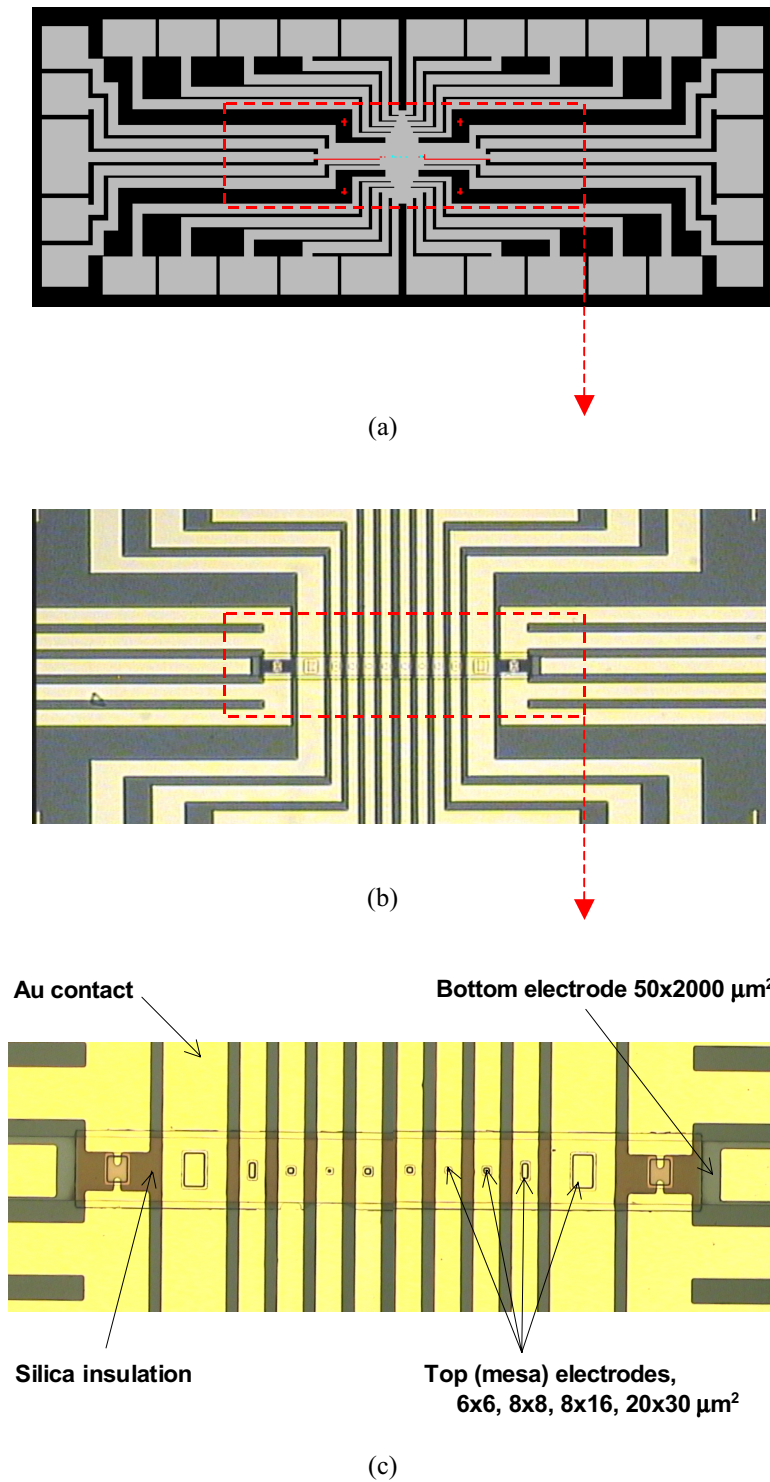


**Fig. 3.3.** The plane-views of the tunnel junction in this study. **(a)** the whole chip of  $10 \times 5 \text{mm}^2$ , **(b)** the center area of the chip and **(c)** the active area with the junctions.

Of overall processes, two particular steps deserve to be mentioned here: (1) the pre-deposition of the thin Au overlayers on the trilayers and (2) the side-wall re-deposition as a by-product during the ion milling.

(1) In each successive step of the microfabrication, the spinning, patterning and post-removal of the photo-resist (PR) are always engaged and this repeated PR processes inevitably tend to leave a very thin residue behind, particularly when the PR patterns involved high-temperature processes. For example in the silica deposition process, the duration of the 30-60min's heat radiation from a RF plasma accumulates intensive heat on the devices. The substrates,  $\text{SrTiO}_3$  or  $\text{NdGaO}_3$  substrates, have very low thermal conductivities and consequently the accumulating heat can scorch the PR on the top electrode. Then even after the silica lift-off, a small silica window ( $4 \times 4 \mu\text{m}^2$ ) is effectively blocked by a very thin scorched PR layer and makes it difficult to form ohmic contact to the top electrode with post-deposited Au layers. This can be avoided with the deposition of a thin Au over-layer on the unpatterned trilayers prior to any process presumably due to the effective thermal dissipation through the Au. Then, a reliable electrical contact to the top electrodes is then much more feasible to achieve even through the residual PR layer, if any.

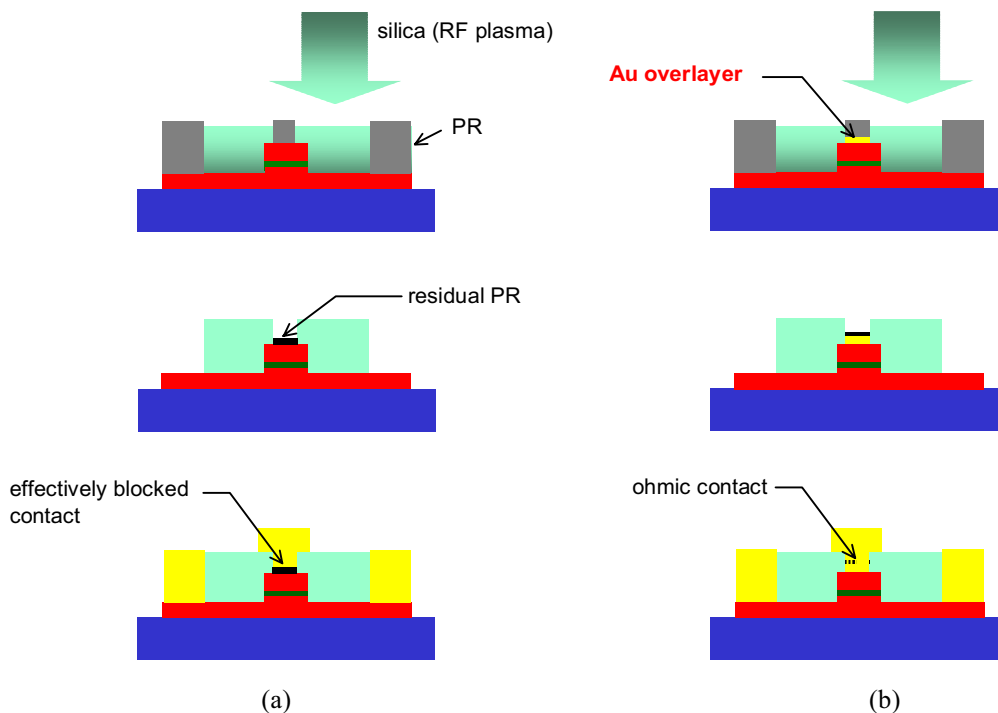


**Fig. 3.4.** The residual PR layer formation during the silica lift-off process. (a) electrical contact to the top electrode is effectively blocked. (b) a thin Au over-layer can facilitate the ohmic contact formation even through the residual PR.

(2) Because the ion milling process is a pure physical etching process, as opposed to reactive ion etching which involves a chemical process as well, etched materials are not so volatile and tend to be re-deposited on any surface where they come into contact, i.e. the side-wall of the wanted features or the PR as seen in Fig. 3.5.

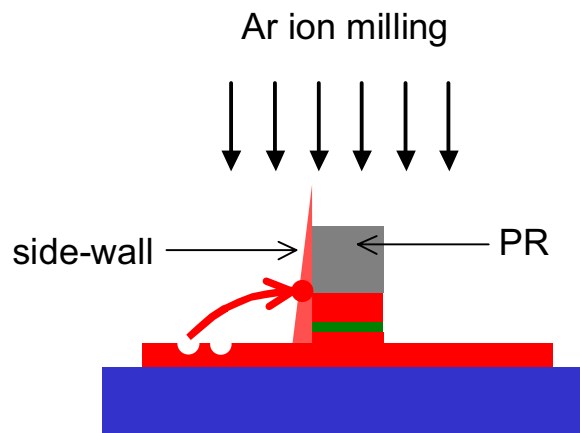


**Fig. 3.5.** A side-wall formation during the Ar milling process.

This side-wall can be sometimes as high as  $1\ \mu\text{m}$  and often resides around the edge of the milled features even after the PR removal. This is critically detrimental for the successive fabrication processes causing major failures in the junction performance such as an electrical short between the top and bottom electrode and the disruption of Au wiring. This effect can be minimized by slow the out-of-plane rocking of the sample holder by few degrees with respect to incident ions along with the constant in-plane rotation of the sample during the milling. When the film is fairly rigid enough, the formed side-wall can be also removed by gentle scrubbing with a soft cotton bud in the acetone solution.

### 3.3 Characterizations and Measurements

#### 3.3.1 Structural characterizations

---

*X-ray  $\theta$ - $2\theta$  diffraction, X-ray rocking curve*

X-ray diffraction scans the reciprocal space to extract microstructural information from the epitaxial films. In the scattering vector ( $q$ ) space, the measurement can probe the population of a certain plane as a function of interplanar spacings (the  $\theta$ - $2\theta$  scan) or as a function of the orientation of the planes (the  $\omega$ -scan or the rocking curve). In the  $\theta$ - $2\theta$  scan, the sample and the detector are rotated by the fixed  $\theta/2\theta$  ratio and it is commonly used to probe out-of plane lattice parameters such as lattice constants, the chemical modulation length and the structural coherency in the multilayers. One limitation is the diffraction scan cannot be easily distinguished when there is a close (out-of plane) lattice-matching. In the  $\omega$ -scan the detector is set at a fixed  $2\theta$  while the sample is rocking by a small degree. A small change ( $\Delta\theta$ ) in the incident angle leads to a change in the parallel component of the scattering vector and it is often used to probe the spread of the in-plane crystal orientation in the film plane.

*Atomic Force Microscopy (AFM)*

The AFM derives topographic images from the measurements of the interaction between a microfabricated tip and the sample surface. The force between the atoms on the sample surface and those on the tip, can be either repulsive<sup>1</sup> or attractive<sup>2</sup>. This causes the tip to deflect and the magnitude of the deflection depends upon the separation between the surface atoms, and the tip atoms and upon the atomic forces between them (Van der Waals forces or Pauli Exclusion forces, etc). This deflection can be recorded via voltage differences measured by a piezoelectric transducer and a feedback loop. The voltage signal is used to map the surface topography of samples with a depth resolution down to atomic-scale and with a lateral resolution up to micron-scale. This very advantage of the AFM makes it uniquely useful in the structural characterization of tunnel barriers of the atomic scale thickness and the micron scale lateral uniformity. An example of the AFM scan is demonstrated in Fig. 3.6, which shows the initial film-growth stage of  $\text{La}_{0.7}\text{Ca}_{0.3}\text{MnO}_3$  on an  $\text{NdGaO}_3$  (001) substrate; the nominal film thickness is 0.2nm, a half unit-cell height. The image consists of the regularly spaced steps and terraces with the step height of 0.4 nm, which corresponds to one unit cell of the pseudocubic  $\text{NdGaO}_3$  perovskite due to the vicinal feature of oxide-substrates: the perovskites-substrates commercially available usually exhibit the off-cut angle of  $0.1 \sim 1^\circ$ . It shows that the film growth proceeds by the nucleation of sub-unit-cell islands on the terraces at step-edges, i.e. the layer-by-layer growth.

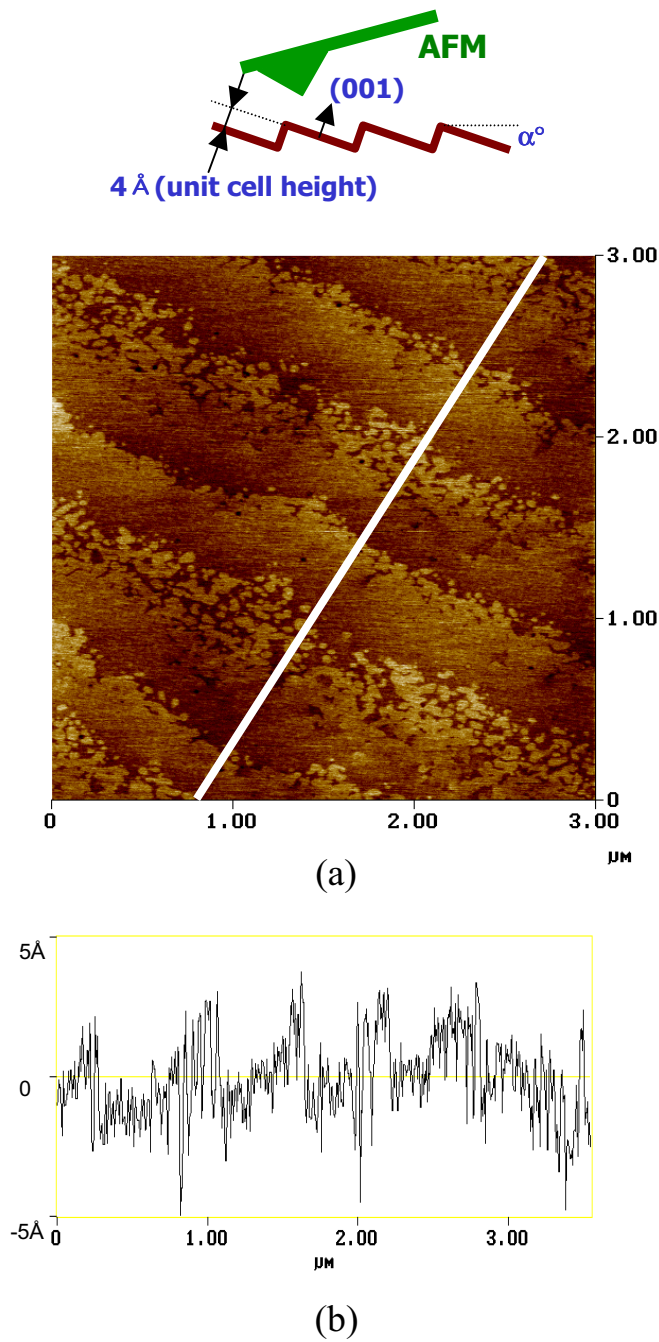


**Fig. 3.6.** (a) The initial growth stage of a  $\text{La}_{0.7}\text{Ca}_{0.3}\text{MnO}_3$  thin film on an  $\text{NdGaO}_3$  (001) substrate; the nominal film thickness is 0.2nm, a half unit cell height. (b) the cross-sectional line profile (the white line in (a)) shows that each step height corresponds to one unit-cell (0.4nm) of the pseudocubic  $\text{NdGaO}_3$  perovskite with the vicinal angle  $\alpha$ .

---

*Transmission electron microscopy (TEM)*

High resolution TEM characterizations have been done on several trilayer samples to structurally and chemically investigate the interfaces with ultimate resolution ( $\sim 0.2\text{\AA}$ ) by collaborators, D. Ozkaya and A. K. Petford-Long in Oxford University.

### 3.3.2 Magnetic measurements

Magnetic measurements in the study were done with a superconducting quantum interference device (SQUID, Quantum Design MPMS<sup>TM</sup>) magnetometer and sometimes with a vibrating sample magnetometer (VSM, Princeton<sup>TM</sup>). The VSM is a gradiometer measuring the difference in magnetic induction between regions of space with and without the sample in the AC pick-up coils and gives a direct measure of the magnetization. It is easy of operation and quick in data acquisition, however, the sample size for the measurement is rather small (as large as  $5\times 5\text{mm}^2$ ) and thus one needs to consider the demagnetization effect. The SQUID magnetometer utilizes the Josephson (the weak link) effect in a superconducting ring, where the flux passing through the weak link is quantized. The voltage change in the pick-up coil occurs by a tiny discrete amount, thus the resolution of the measurement can be down to  $10^{-14}\text{T}$ . Although it generally requires a long time for each measurement and involves a He cryogenic, it gives fairly stable performances particularly for high field (up to 7T) scans and temperature dependent scans (4.2K – 300K), which is crucial to the thesis study. Therefore for the magnetic measurement, the SQUID magnetometer was primarily used.

### 3.3.3 Electrical transport measurements

*Temperature dependent resistance measurements*

The structural properties and the chemical stoichiometry of mixed valence manganites films are very sensitive to the film resistivity and thus can uniquely be reflected in the Temperature dependent resistance measurement as discussed in the Chapter 2.2. For example, the substrate-induced strain or the oxygen deficiency can be explicit in the residual low resistivity at low temperature, the metal-insulator transition temperatures and temperature

---

coefficients of resistance. Usually the temperature dependent resistance measurement is quick and non-destructive, and thus it was often used as a routine indicator for the crystal and chemical qualities of the deposited films. For the measurement an unpatterned film is loaded on the custom-built 4-points probe with spring loaded pogo pins and inserted into a liquid He<sup>4</sup> dewar. The cooling and heating rate in the dewar during the measurement is controlled not to cause a thermal lag by a LabView program via a heater underneath the sample.

#### *Junction magnetoresistance measurements*

The tunnel magnetoresistance (TMR) of the SPT junctions were measured with the four probe a.c. measurement as described in Fig. 3.7 in the custom-built probes. For the TMR measurement the sample-engaged probe is inserted into a liquid N<sub>2</sub> flask, which is mounted in-between a Helmholtz pair (the maximum field flux is 4kOe).

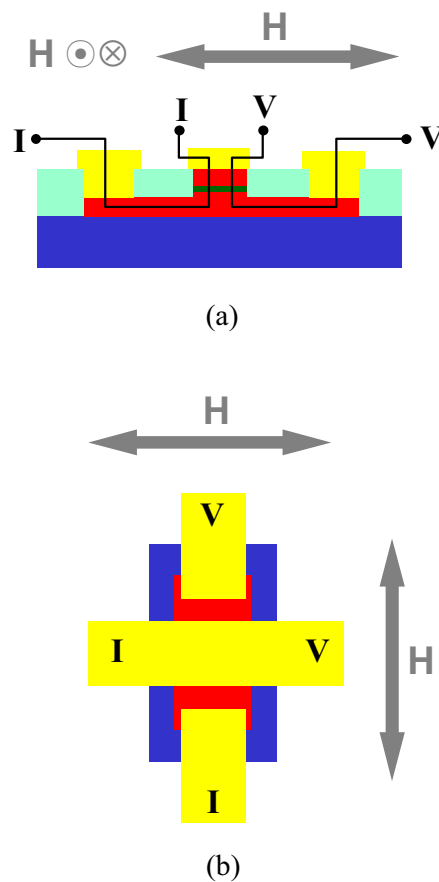


**Fig. 3.7.** The TMR measurement geometry in this study (a) the cross-sectional view and (b) the plane view. Gray arrows represent magnetic fields applied during the measurements.

The probes are especially designed for both in-plane and out-of-plane angular rotation measurements. The cooling and heating rate and the magnetic field ramping rate were controlled by computer-based LabView<sup>TM</sup> programs (designed by lab colleagues, Gavin Burnell and Neil Todd).

**REFERENCES**

- 
- <sup>1</sup> G. Binnig, C.F. Quate and Ch. Gerber, *Phys. Rev. Lett.* **56**, 930 (1986).
- <sup>2</sup> T.R. Albrecht, P. Grütter, D. Horne and D. Rugar, *J. Appl. Phys.* **69**, 668 (1991).

---

## CHAPTER 4

# Interfacial Magnetism in Manganite Heterostructures: Implication for Spin Polarised Tunnelling

---

*I have investigated the electrical transport properties of heteroepitaxial  $\text{La}_{0.7}\text{Ca}_{0.3}\text{MnO}_3$  (LCMO)/ $\text{SrTiO}_3$  (STO) multilayers; as the LCMO layer thickness was varied from 25nm to 2.5nm, the metallic transition was suppressed and enhanced magnetoresistance extended to low temperatures. The results of transport and magnetic measurements imply a vertically inhomogeneous magnetic structure in the LCMO layers, with magnetically disordered interfaces. This work had implications for barrier optimization in SPT junctions: it suggested a strong electron-lattice coupling and inhomogeneous interfacial magnetic order due to significant lattice-mismatch. The heteroepitaxial growth of the LCMO films on lattice-matched  $\text{NdGaO}_3$  suggested that by appropriate materials engineering the intrinsic high polarisation of half-metallic materials can be fully utilized for the spin polarised tunnelling.*

## 4.1 Motivations

The electronic and magnetic structure at surfaces or interfaces in mixed valence manganites have received demanding interests of active research, particularly with direct relevance to spin-polarised tunnelling. Previous studies of ultra-thin manganite films have shown strong suppression of ferromagnetism as the thickness is reduced.<sup>1,2</sup> Heteroepitaxial multilayer structures can be useful tools to investigate interface magnetism as well as to artificially tailor their electronic properties. In this chapter I report a study of the electrical transport and magnetic structure of manganite multilayers. I chose an insulating layer, SrTiO<sub>3</sub> (STO) as an interlayer in a series of La<sub>0.7</sub>Ca<sub>0.3</sub>MnO<sub>3</sub>(LCMO)/STO multilayers, mainly because it is most commonly used as a insulating tunnel barrier (the band gap  $\sim 3\text{eV}$ ) in perovskite-based oxides electronic devices.

## 4.2 Lattice-mismatched heteroepitaxial La<sub>0.7</sub>Ca<sub>0.3</sub>MnO<sub>3</sub>/SrTiO<sub>3</sub> multilayers

LCMO/STO multilayers were grown *in-situ* by pulsed laser deposition using stoichiometric targets on STO (100) substrates at 700°C in 15Pa oxygen atmosphere. Subsequently they were annealed at 700°C in 50kPa oxygen for an hour and cooled down to room temperature. A series of multilayers were deposited with the individual LCMO layer thickness of 2.5, 5, 8.3, 12.5, 25 nm with different numbers of layers ranging from 10 to 1 (keeping the total LCMO thickness at 25 nm) with the individual STO layer thickness of 7 nm in each case. Electrical transport and magnetoresistance were measured using a four points probe, where spring loaded needle-contacts were made to the multilayers to assure the uniform current distribution through all LCMO layers in the multilayers.

Sharp interfaces and uniformly continuous layers in multilayers were confirmed by transmission electron microscopy as in Fig. 4.1. X-ray  $\theta$ -2 $\theta$  diffraction scans around the LCMO (002) peak of several multilayers are shown in Fig. 4.2. Satellite peaks adjacent the main peaks arising from chemical modulation of multilayer structures indicate sound heterostructure growth. Gradual broadening of the first order (002) lines at larger LCMO layer thicknesses indicates that the misfit strain in the LCMO due to lattice-mismatch with STO (the lattice mismatch,  $\Delta a/a_{\text{STO}}$  is  $\sim 1.2\%$ , where  $a$  is a lattice parameter of pseudocubic perovskites) is progressively relaxed in part, possibly resulting in misfit dislocations.

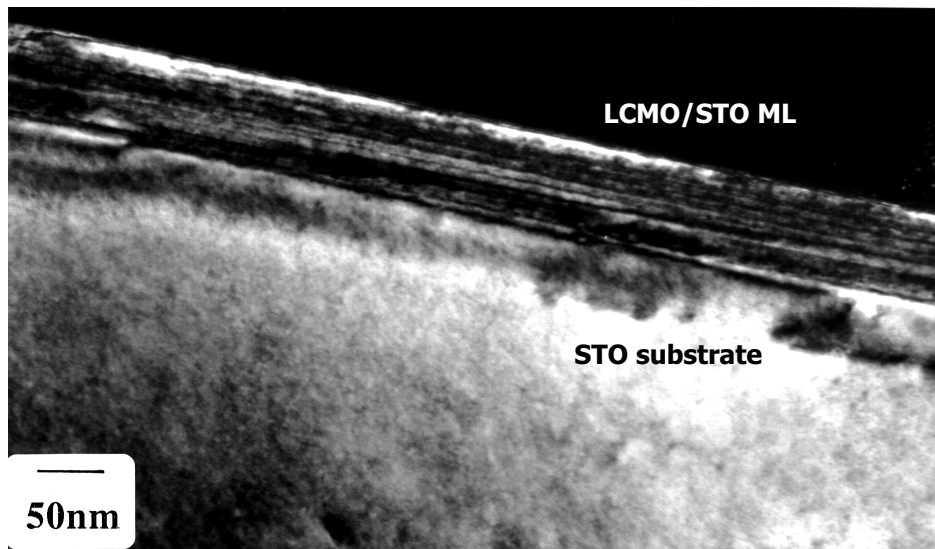


**Fig. 4.1.** A cross-sectional TEM image of the  $(\text{LCMO/STO})_n: (2.5\text{nm}/7\text{nm})_{10}$  multilayer.  
(Courtesy by S. Newcomb.)

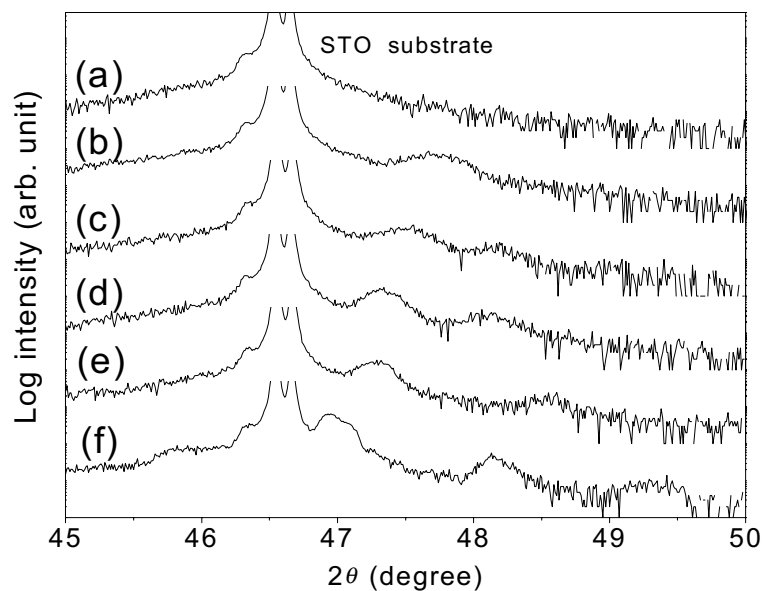


**Fig. 4.2.** The  $\theta$ - $2\theta$  XRD scans for (a) a STO bare substrate, (b) a 25nm-thick LCMO film, (c)  $(\text{LCMO/STO})_n: (12.5\text{nm}/7\text{nm})_2$ , (d)  $(8.3\text{nm}/7\text{nm})_3$ , (e)  $(5\text{nm}/7\text{nm})_5$ , and (f)  $(2.5\text{nm}/7\text{nm})_{10}$  respectively. Sample (b) of a plain LCMO film showed out-of plane lattice parameter of 0.382nm (that of bulk LCMO is 0.386nm).

### 4.3 Inhomogeneous transport of the $\text{La}_{0.7}\text{Ca}_{0.3}\text{MnO}_3$ multilayers

Figure 4.3 shows the zero-field temperature ( $T$ ) dependence of the resistance ( $R$ ): with reducing individual LCMO layer thickness the peak resistance temperature ( $T_p$ ) is monotonically lowered and the breaths of metal-insulator transitions broaden. Despite the substantial changes in low temperature properties, the resistivity above  $T_p$  is almost unaffected by the change in individual layer thickness: Fig. 4.3(b) ~ (e). The inset shows that the maximum temperature coefficient of resistance, a measure of the sharpness of the metallic transition<sup>3</sup>, decreases with lower  $T_p$  for thinner multilayers.

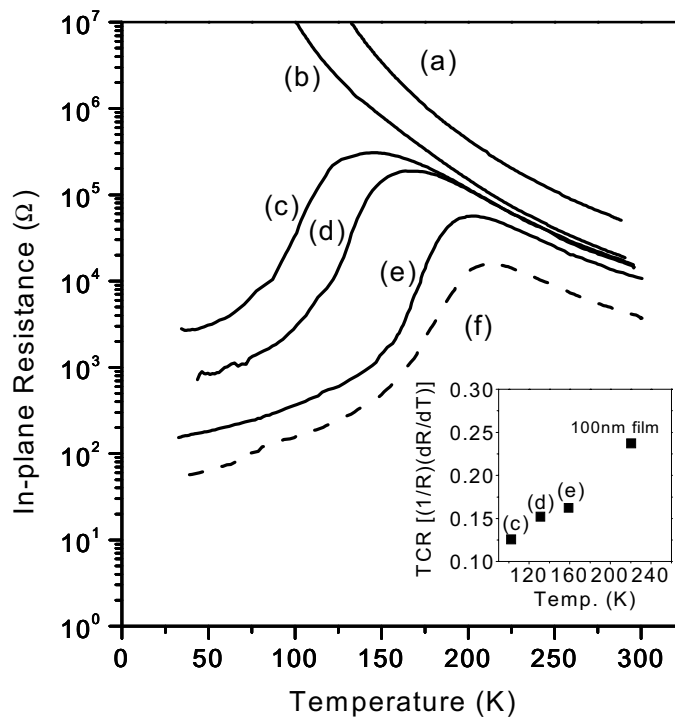


**Fig. 4.3.** Temperature dependent resistance of multilayers for (a)  $(\text{LCMO}/\text{STO})_n$ ;  $(2.5\text{nm}/7\text{nm})_{10}$ , (b)  $(5\text{nm}/7\text{nm})_5$ , (c)  $(8.3\text{nm}/7\text{nm})_3$ , (d)  $(12.5\text{nm}/7\text{nm})_2$ , and (e) 25nm thick LCMO film and (f)  $(17\text{nm}/16\text{nm})_3$ , respectively. It should be noted that the total LCMO thickness in (f) is twice that of the other samples. In the inset, the maximum temperature coefficients of resistance were presented for several multilayers along with 100nm thick plain LCMO film. The resistances of the sample (a) and (b) at low temperatures are beyond our experimental set-up.

In mixed valence manganites, it is known that strong electron-lattice coupling due to the Jahn-Teller distortion or internal pressure by cation exchange with different ionic size can alter the charge transfer interaction between Mn ions.<sup>4,5</sup> As a consequence of the superlattice structure the strain field of the LCMO layers in the heteroepitaxial structure is rather difficult to measure directly from the XRD plots, nevertheless it can be reasonably postulated that larger strain is accommodated in thinner multilayers.<sup>1,2</sup> It seemed that the observed  $R(T)$  behavior of heteroepitaxial multilayers is related to pronounced tensile strain in the LCMO layers from the lattice mismatched STO layers. However, in a further investigation on the strain effect with multilayers of the same layer thickness ratio (thus presumably with the same strain), LCMO/STO of 8.3nm/7nm in (c) and 16nm/15nm in (f), the transition temperature returned back to higher temperature in the multilayer with thicker LCMO layer. This finding suggested that the metallic transition is rather directly parameterized with the LCMO thickness than the strain of the LCMO in the multilayers.

Figure 4.3 shows the temperature dependent magnetoresistance,  $MR(T)$  of the multilayers. As the LCMO layer thickness decreases (25nm to 8.3nm), the MR, defined as  $[R(0)-R(H)]/R(0)$ , is enhanced and extended to a lower temperature range ( $T < T_p$ ). However, it should be noted that on decreasing the strain in the LCMO layers by reducing the STO layer thickness from 7nm to 3.5nm, the  $MR(T)$  does not significantly alter.

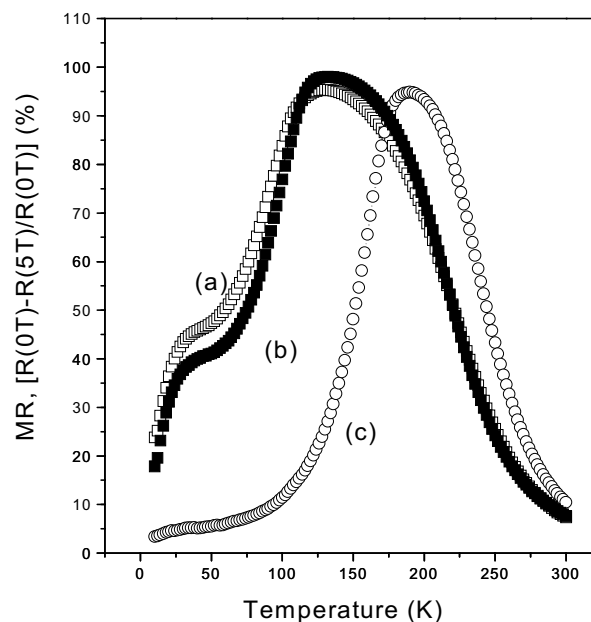


**Fig. 4.4.** Temperature dependent MR of multilayers for (a)  $(\text{LCMO/STO})_n$ : (8.3nm/3.5nm)<sub>3</sub>, (b) (8.3nm/7nm)<sub>3</sub>, and (c) 25nm thick LCMO film.

Based upon the rigid body fitting model in thin coherently strained multilayers, it seems reasonable to conclude that the lattice-mismatch induced strain is uniformly distributed to the constituent layers.<sup>6</sup> If strain alone was controlling the behavior, fine-period multilayers with the same LCMO layer thickness but different STO layer thickness would be expected to show different MR(T) behaviors. The similar MR(T) behavior of multilayers with different STO layer thickness indicates that the strain variation can not solely explain the transport properties mentioned above.

#### 4.4 Interfacial magnetism in the $\text{La}_{0.7}\text{Ca}_{0.3}\text{MnO}_3/\text{SrTiO}_3$ multilayers

High field magnetoresistance (HFMR) up to 7T is presented in Fig. 4.5. The plain LCMO film shows little negative MR at low temperatures; the multilayer of  $(8.3/7)_3$  shows a “hysteretic” MR of significant magnitude at low temperatures.<sup>2</sup>

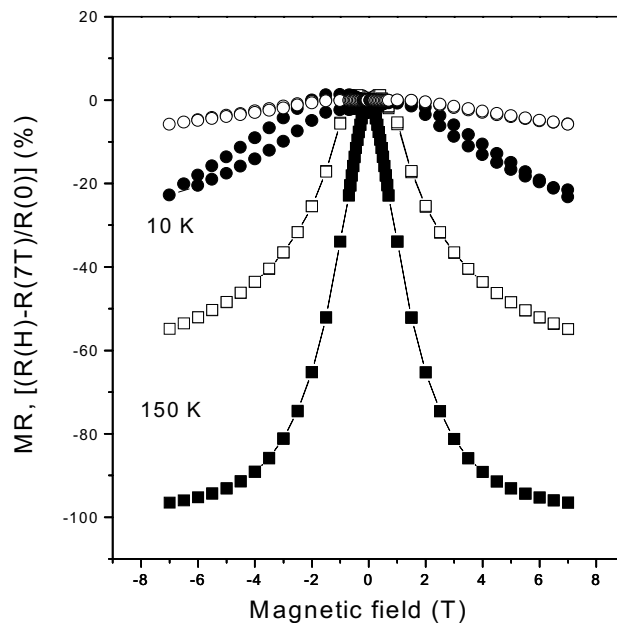


**Fig. 4.5.** The magnetic field dependent MR of  $(8.3\text{nm}/7\text{nm})_3$  multilayers (solid) and 25nm thick plain LCMO film (open) at 10K and 150K.

Negative HFMR in the multilayer continues to increase up to maximum field (7T) and reaches a value of 25%, defined as  $[R(0T)-R(H)]/R(0T)$ , at 10K although the magnetization appears essentially saturated at much lower field ( $H < 0.5T$ ) as seen in Fig. 4.6. This can be related to an extrinsic contribution to transport at low temperature ( $T < T_c$ ) most likely from the spin disorder at the interfaces.<sup>7,8</sup> Another noteworthy feature is that whilst the saturation magnetization of the single 25nm LCMO layer is  $\sim 400\text{emu/cm}^3$ , which is comparable to the value of the typical epitaxial film,<sup>8</sup> that of the multilayer of  $(2.5/7)_3$ , reduced to only  $\sim 150\text{emu/cm}^3$ . The loss of the total magnetic moment in the thinnest multilayer implies appreciable magnetic frustration the interfaces. This is clearly related to the loss in low temperature conductivity observed in Fig. 4.3, while at high temperatures where the conductivity is dominated by thermally-induced magnetic disorder (paramagnetism) and rather independent of the layer thickness.

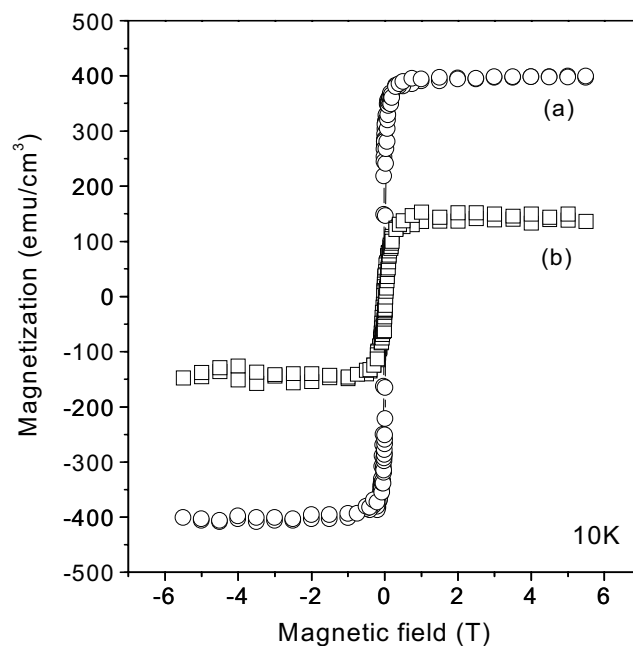


**Fig. 4.6.** Magnetic hysteresis loops measured at 10 K for (a) 25nm thick plain LCMO film and (b)  $(2.5\text{nm}/7\text{nm})_{10}$  multilayers.

Figure 4.7 shows the temperature dependence of the magnetization for three different samples. Whilst  $T_p$  is monotonically lowered as the LCMO layer thickness decreased (Fig. 4.2), the Curie temperature ( $T_c$ ) in (a) and (b) is reduced from the bulk value ( $T_c = \sim 250\text{K}$ ) by a much smaller amount.

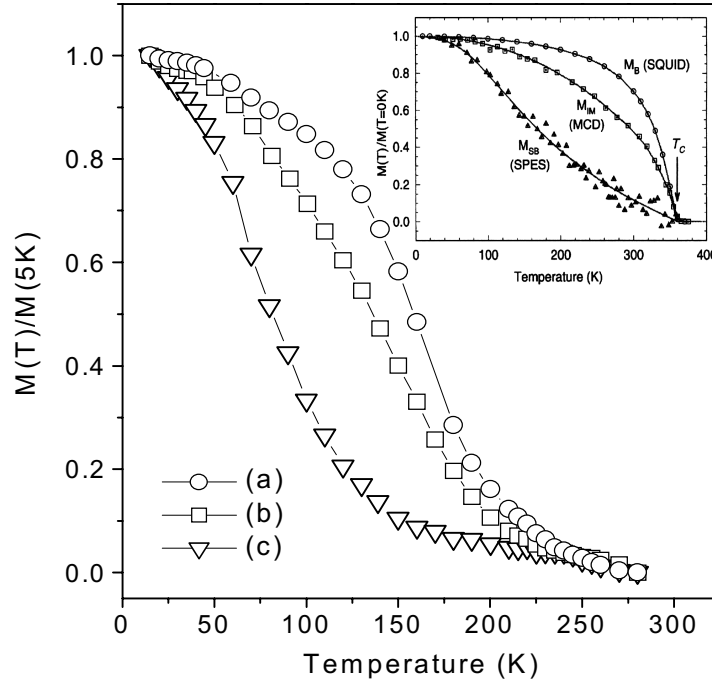


**Fig. 4.7.** Temperature dependence of magnetization of (a) a plain 25nm LCMO film, (b) (LCMO/STO)<sub>n</sub>: (8.3nm/7nm)<sub>3</sub>, and (c) (2.5nm/7nm)<sub>10</sub>, measured at 0.5 T after zero-field cooling in this study. The inset shows measured magnetizations of La<sub>0.67</sub>Sr<sub>0.33</sub>MnO<sub>3</sub> on different length scale, where  $M_B$ ,  $M_I$  and  $M_{SB}$  denote the bulk, the intermediate (~5nm) and the surface boundary (~0.5nm). (After Ref. [9].)

Even in the thinnest multilayer, although  $T_c$  is strongly suppressed, ferromagnetic behavior is still observed at low temperatures despite a monotonic increase in transport resistance with decreasing temperature. It should be noted that the  $M(T)/M(5K)$  of the multilayers decay much faster with increasing temperature and in particular the thinnest multilayer showed a similar behavior to the magnetization of the surface boundary in La<sub>0.7</sub>Sr<sub>0.3</sub>MnO<sub>3</sub> films measured by spin resolved photoemission as seen in the inset.<sup>9</sup>

The decoupling of  $T_p$  from  $T_c$ , which is verified in the comparison of Fig. 4.3 and Fig. 4.7, indicates a break-up of the one-to-one correlation between paramagnetic-ferromagnetic and insulating-metallic transitions implicit in double exchange interaction.<sup>10</sup> A magnetotransport studies in very thin manganite films imply the existence of magnetically inactive regions either

at interface or surfaces.<sup>11</sup> A similar rationale can be applied to the localized interface magnetism between LCMO/STO layers in this study, which implies a strong correlation between inhomogeneous transport and magnetically frustrated interfaces. The fact that the transport properties in multilayers are primarily dependent upon the LCMO layer thickness even under the different strain field cannot be solely explained by the electron-lattice coupling due to the lattice-mismatch induced strain. This strongly indicates the intrinsic existence of vertical inhomogeneity in the electrical and magnetic structure at interfaces. Recent both theoretical and experimental studies suggested that the ground states of mixed valence manganites tend to be inherently inhomogeneous, stabilizing multi-phase coexistence.<sup>12</sup> It has been also argued that the tendency to phase separation is further evolved under the influence of strain.<sup>13</sup> The results of this study suggest that the lattice-mismatch induced strain contributes to inhomogeneous magnetic order at interfaces.

#### **4.5 Lattice matched heteroepitaxy with NdGaO<sub>3</sub>**

The interfacial magnetic-disorder in which the role of strain was empirically verified above has serious implication for the optimisation of spin polarised tunnel junctions because electron tunnelling is inherently an interfacial phenomenon. Here I note that the growth of LCMO on STO usually leads to initial island-growth giving rise to layer non-uniformity and discontinuity. A similar discontinuous island growth was reported in the initial growth of La<sub>0.67</sub>Sr<sub>0.33</sub>MnO<sub>3</sub> thin films on LaAlO<sub>3</sub> (001) and NdGaO<sub>3</sub> (110), where the thickness of magnetic dead layers was inferred to be 5nm and 3nm respectively. In fact the principal role of strain in the heteroepitaxial systems can be associated with the structural coherence. The physical origins of the initial thin film growth modes are related to the surface free energy and its distribution. However in the presence of appreciable strain clamped from the lattice-mismatch substrate, strain can be a major driving force governing the film growth mode; strain field usually introduces surface roughening above a certain critical thickness resulting in the islands growth.<sup>14</sup> The three-dimensional island growth can be critically detrimental to junction performances, particularly when the size of islands reaches up to the thickness of tunnel barriers resulting in junction instability. The values of tunnel magnetoresistance (TMR) reported in half-metallic manganite junctions are usually well below those predicted on the basis of their polarisation even at low temperatures. Presumably it can be attributed to the interfacial structure-instability, where the formation of atomically sharp interfaces is suppressed due to the three islands growth driven by

strain.

There are a variety of choices in single crystalline substrate with perovskite-related structures. In most cases they can be regarded as pseudo-cubic in the “cube-on-cube” growth model. Table 4.1 summarized the crystalline parameters of those commercially available substrates.

Table 4.1. Lattice parameters of various pseudocubic perovskite substrates.

Substrates	In-plane lattice parameters ( $a, b$ )	Out-of-plane lattice parameters ( $c$ )	Lattice-mismatch with LCMO <sup>1)</sup> (in-plane)
SrTiO <sub>3</sub> (100)	$a=b= 3.911\text{\AA}$	$c= 3.911\text{\AA}$	1.17%
LaAlO <sub>3</sub> (100)	$a=b= 3.790\text{\AA}$	$c= 3.790\text{\AA}$	-1.98%
NdGaO <sub>3</sub> (110)	$a= 3.864\text{\AA}, b= 3.855\text{\AA}$	$c= 3.858\text{\AA}$	0.13%
NdGaO <sub>3</sub> (001)	$a=b= 3.864\sim 3.867\text{\AA}$	$c= 3.858\text{\AA}$	$\sim 0.05\%$
LSAT <sup>2)</sup> (100)	$a=b= 3.868\text{\AA}$	$c= 3.868\text{\AA}$	0.07%
LaGaO <sub>3</sub> (100)	$a=b= 3.896\text{\AA}$	$c= 3.894\text{\AA}$	0.80%
<b><math>La_{0.7}Ca_{0.3}MnO_3</math></b>	<b><math>a=b= 3.865\text{\AA}</math></b>	<b><math>c= 3.865\text{\AA}</math></b>	

<sup>1)</sup> Lattice mismatch is defined as  $(a_s - a_f)/a_s$ , where  $a_s$  and  $a_f$  are in-plane lattice parameters of substrates and films.

<sup>2)</sup> LSAT:  $(LaAlO_3)_{0.3}(SrAlTaO_6)_{0.7}$

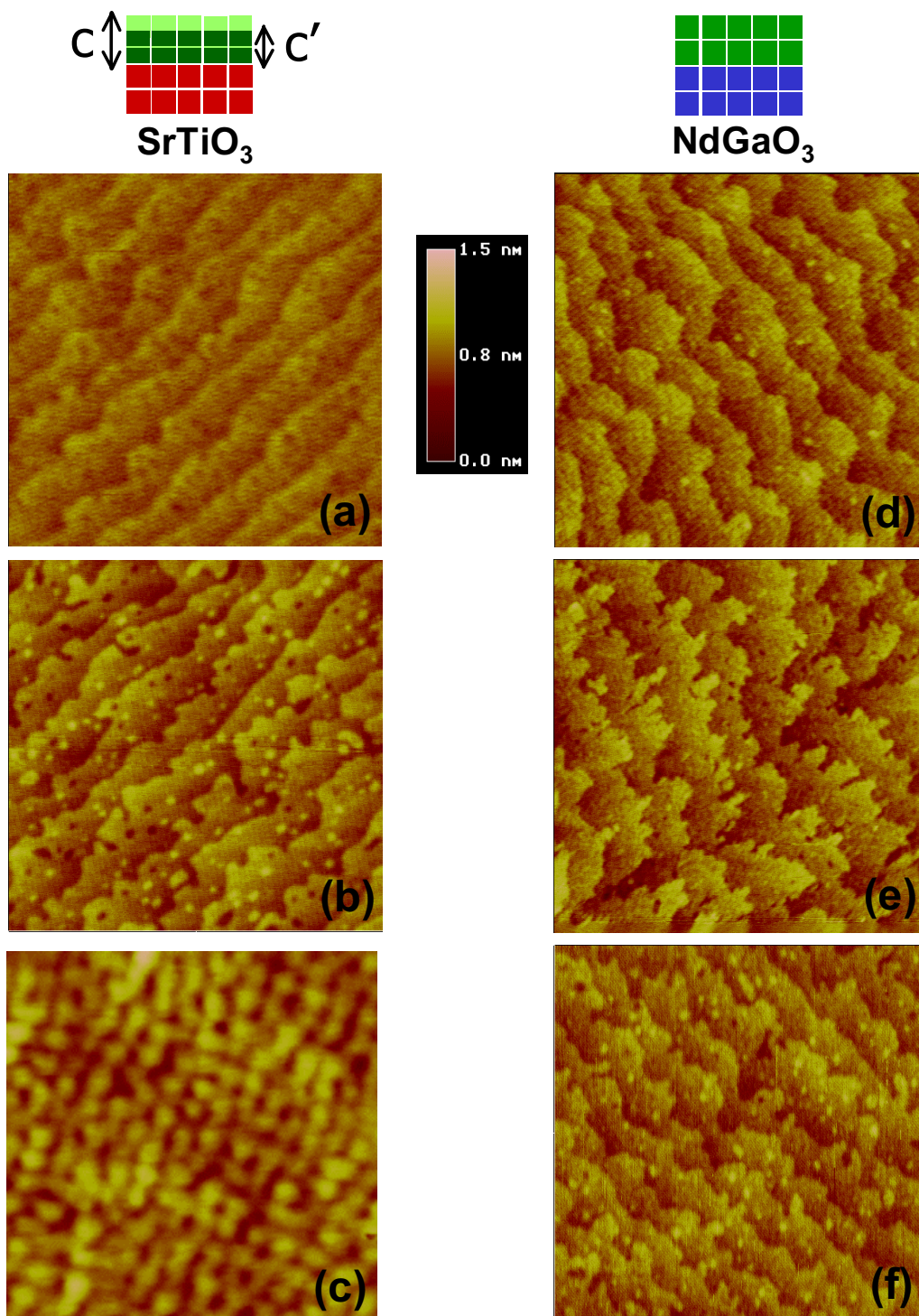
Amongst several candidates in Table 4.1, NdGaO<sub>3</sub> (001) shows minimal (in-plane) lattice-mismatch of 0.05% with LCMO. I thus further explored the heteroepitaxy of LCMO on NdGaO<sub>3</sub> (NGO). The crystal structure of NGO belongs to the orthorhombically distorted

perovskite structure (space group  $Pbn2_1$ ) and shows no significant structural transition between 2K and 300K.  $\text{Nd}^{3+}$  possesses a magnetic moment ( $J=9/2$ ) and it is known that there is an antiferromagnetic ordering at 0.97K. This material has long been used as a substrate for the growth of high  $T_C$  superconductors mainly because of close lattice match, i.e.  $\text{YBa}_2\text{Cu}_3\text{O}_x$  on NGO (110).

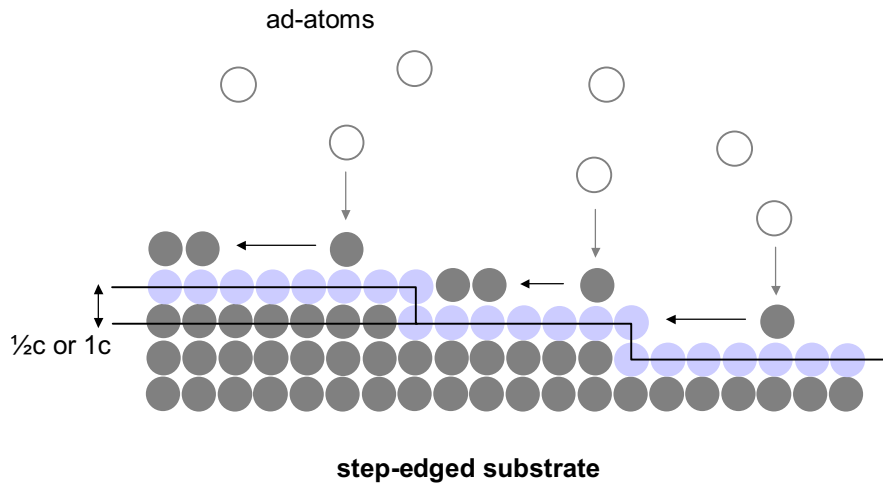
The series of AFM surface images of the LCMO film grown on STO (100) and NGO (001) revealing the evolution of the film growth mode are shown in Fig. 4.8. Surface morphology of bare STO (100) and NGO (001) substrates show the typical vicinal features – steps and terraces – where the step heights are either half ( $\sim 2\text{\AA}$ ) or one unit cell ( $\sim 4\text{\AA}$ ). The off-cut angle is usually  $<1^\circ$ . Since the step edges can serve as low-energy nucleation sites, one can facilitate a layer-by-layer growth when the coherent growth is optimized, i.e. step-flow growth mode as schematized in Fig. 4.9.

Figure 4.8 clearly demonstrates the role of strain induced from lattice mismatch in the coherent epitaxial film growth. Although both LCMO on STO and NGO shows the two-dimensional layer-by-layer growth mode in the very early stages, above the substantial thickness, i.e.  $\sim 70\text{nm}$ , the growth of the LCMO on STO transformed to the three-dimensional island growth whereas the growth on NGO still preserves the layer-by-layer growth.

As expected, the strain in the LCMO films grown on STO and NGO also makes difference in the transport behaviors as seen in Fig. 4.10 due to electron-lattice coupling. The LCMO on NGO exhibits the  $T_C$  of  $\sim 260\text{ K}$  that is very close to that of a bulk LCMO with much lower residual resistivity at low temperatures suggesting weak lattice-mismatch effects and possibly less interfacial disorder. Therefore I further explored the heteroepitaxial LCMO/NGO/LCMO trilayers grown on NGO (001) for the optimisation of tunnel junctions as will be discussed in the next Chapter.



**Fig. 4.8.** The AFM surface morphology of LCMO thin films ( $500 \times 500 \text{ nm}^2$ ). (a) a bare STO (b) 5nm thick LCMO on STO (c) 70nm-LCMO on STO, (d) a bare NGO (e) 5nm-LCMO on NGO (f) 70nm-LCMO on NGO.



**Fig. 4.9.** The layer-by-layer growth mode on the step-edged substrate.

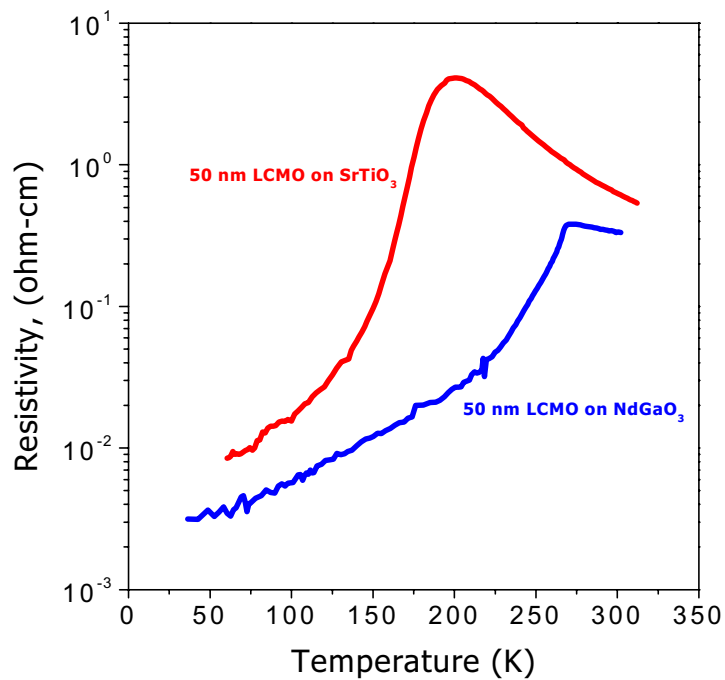


**Fig. 4.10.** The temperature dependent resistivity of 50nm-thick LCMO thin films grown on STO and NGO. The comparison demonstrates a strong electron-phonon interaction due to the lattice-mismatch induced strain in LCMO thin films.

---

*A part of this work is supported by the UK-Spain bilateral funding scheme “Acciones Intergrada” and I thank collaborators, M. Bibes and J. Fontcuberta for the high field measurements of manganites heterostructures during my stay in Campus Universitat Aut3noma de Barcelona in Spain.*

## REFERENCES

- 
- <sup>1</sup> J. Aarts, S. Freisem, R. Hendrix and H.W. Zandbergen, *Appl. Phys. Lett.* **72**, 2975 (1998).
  - <sup>2</sup> M.G. Blamire, B.-S. Teo, J.H. Durrell, N.D. Mathur, Z.H. Barber, J.L. McManus Driscoll, L.F. Cohen and J.E. Evetts, *J. Magn. Magn. Mater.* **191**, 359 (1998).
  - <sup>3</sup> T. Venkatesan, M. Rajeswari, Z.W. Dong, S.B. Ogale and R. Ramesh, *Philos.Trans. R. Soc. London, Ser. A* **356**, 1661 (1998).
  - <sup>4</sup> A.J. Millis, P.B. Littlewood and B.I. Shraiman, *Phys. Rev. Lett.* **74** 5144 (1995) and A.J. Millis, *Nature* **392**, 147 (1998).
  - <sup>5</sup> H.Y. Whang, S.-W. Cheong, P.G. Radaelli, M. Marezio and B. Batlogg, *Phys. Rev. Lett.* **75**, 914 (1995).
  - <sup>6</sup> A. Gupta, R. Gross, E. Olsson, A. Segmuler, G. Koren, and C. C. Tsuei, *Phys. Rev. Lett.* **64**, 3191 (1990).
  - <sup>7</sup> LI. Balcells, J. Fontcuberta, B, Martinez and X. Obradors, *Phys. Rev.* **B 58**, 14697 (1998).
  - <sup>8</sup> A. Gupta, G. Q. Gong, G. Xiao, P. R. Duncombe, P. Lecoeur, P. Trouilloud, Y. Y. Wang, V. P. Dravid and J. Z. Sun, *Phys. Rev.* **B 54**, 15629 (1996).
  - <sup>9</sup> J.-H. Park, E. Vescovo, H.-J. Kim, C. Kwon, R. Ramesh and T. Venkatesan, *Phys. Rev. Lett.* **81**, 1953 (1998).
  - <sup>10</sup> C. Zener, *Phys. Rev.* **82**, 403 (1951) and P.W. Anderson, H. Hasegawa, *Phys. Rev.* **100**, 67 (1955).
  - <sup>11</sup> J.Z. Sun, D.W. Abraham, R.A. Rao and C.B. Eom, *Appl. Phys. Lett.* **74**, 3017 (1999).
  - <sup>12</sup> A. Moreo, S. Yunoki and E. Dagotto, *Science* **283**, 2034 (1999) and the references therein.
  - <sup>13</sup> For example see, A. Biswas, R. Rajeswari, R.C. Strivastava, Y.H. Li, T. Venkatesan, R.L.Greene and A.J. Millis, *cond-mat/9910501*.
  - <sup>14</sup> Eds. Z. Zhang and M.G. Lagally, “Morphological organization in epitaxial growth and removal”, World Scientific, Singapore (1998).
-

---

## CHAPTER 5

# Lattice Engineered $\text{La}_{0.7}\text{Ca}_{0.3}\text{MnO}_3/\text{NdGaO}_3/\text{La}_{0.7}\text{Ca}_{0.3}\text{MnO}_3$ Tunnel Junctions

---

*Spin polarised tunnelling devices based upon a half-metallic manganite,  $\text{La}_{0.7}\text{Ca}_{0.3}\text{MnO}_3$  incorporating a novel barrier material,  $\text{NdGaO}_3$  were fabricated. These devices show unprecedentedly high tunnel magnetoresistance (TMR) values above 77K and coherent switching with a qualitatively different dependence of resistance on magnetic field to previous devices. The electron polarisation deduced from measurements at 77K is higher than the directly measured value at 4.2K, however the TMR is suppressed drastically with increasing temperature and does not persist close to the Curie temperature ( $T_C$ ). I suggest an active tunneling mechanism based on percolative phase separation to account for the general TMR temperature dependence in these materials.*

*The results in this work provide direct evidence for high spin polarisation of half-metallic materials at high temperatures and demonstrated the feasibility of maximizing TMR.*

## 5.1 Motivations

In half-metallic ferromagnets such as the optimally doped manganites the relatively narrow spin up and spin down conduction bands are completely separated leading to 100% polarisation at low temperatures<sup>1,2</sup> and thus these materials have been recognized for several years as being good candidates for the study of spin polarised tunnelling.<sup>3,4,5</sup> However, TMR devices incorporating such materials have yielded reproducible tunnel magnetoresistance (TMR) values only at the lowest temperatures, and even these values are well below those predicted on the basis of the independently measured polarisation (>75%).<sup>6</sup> The magnetic properties of these materials are highly sensitive to local crystal properties and the extrinsic strain fields induced by the lattice-mismatch with the substrates or tunnel barrier can be sufficient to severely degrade the ferromagnetic order in the surface layers that are critical for tunnelling.<sup>7</sup> In this chapter I describe devices based on a half-metallic manganite,  $\text{La}_{0.7}\text{Ca}_{0.3}\text{MnO}_3$  (LCMO) incorporating a novel barrier material,  $\text{NdGaO}_3$  (NGO) where the lattice-mismatch is minimized.

## 5.2 Lattice engineered $\text{La}_{0.7}\text{Ca}_{0.3}\text{MnO}_3/\text{NdGaO}_3/\text{La}_{0.7}\text{Ca}_{0.3}\text{MnO}_3$

In this study, NGO is selected for the substrate and tunnel barrier because of its small lattice-mismatch ( $\Delta a/a < 0.08\%$ ,  $a$  being the in-plane lattice parameter) with LCMO electrodes as described in the previous chapter. LCMO/NGO/LCMO trilayers were grown *in-situ* by pulsed laser deposition using stoichiometric targets with layer thickness' scale of 80nm(bottom)/2.5-3nm/60nm(top). Heteroepitaxial trilayer growth on NGO substrate exhibits a typical layer-by-layer growth mode indicating the high quality of heteroepitaxial structure. As shown in Fig. 5.1, the surface of the trilayer consist of atomically flat terraces with one unit cell height ( $\sim 0.4$  nm) which is essentially the same feature of the original substrate with the off-cut angle of  $< 0.6^\circ$ .

Cross-sectional transmission electron microscopy (TEM) images of the trilayer heterostructure are shown as in Fig. 5.2. Bright field images of the barrier region as in Fig. 5.2.(a) and (b) show atomically sharp interfaces and the chemical mappings from Nd  $M_5$  energy loss edge profiles in Fig. 5.2. (c) and (d) also confirm the minimum chemical mixing at the interfaces.

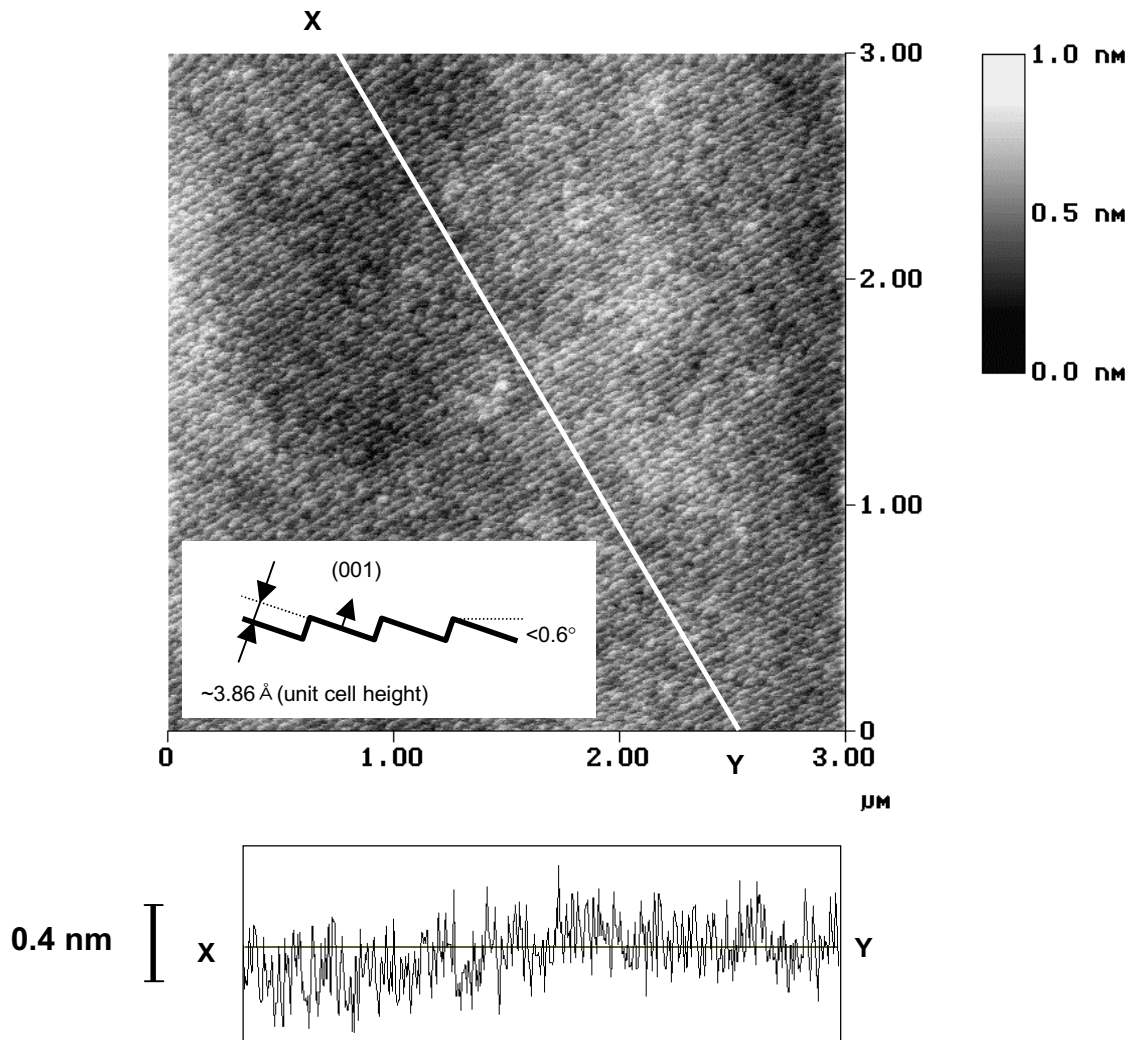


**Fig. 5.1.** AFM image of the LCMO/NdGaO<sub>3</sub>/LCMO trilayer (3x3 $\mu\text{m}^2$ ). The cross-sectional line profile shows that each step height corresponds to one unit cell thickness of the pseudocubic perovskite in a given heterostructure.

The resistance of the common base electrode could be independently measured; generally this showed a Curie temperature ( $T_C$ ) of 265K, which is similar to that of unpatterned epitaxial single films. The base electrode sheet resistance at low temperatures was several orders of magnitude lower than the junction resistance, which ensures the uniform current distribution across the barrier and thus any possible geometrical MR enhancement can be eliminated.<sup>8</sup>

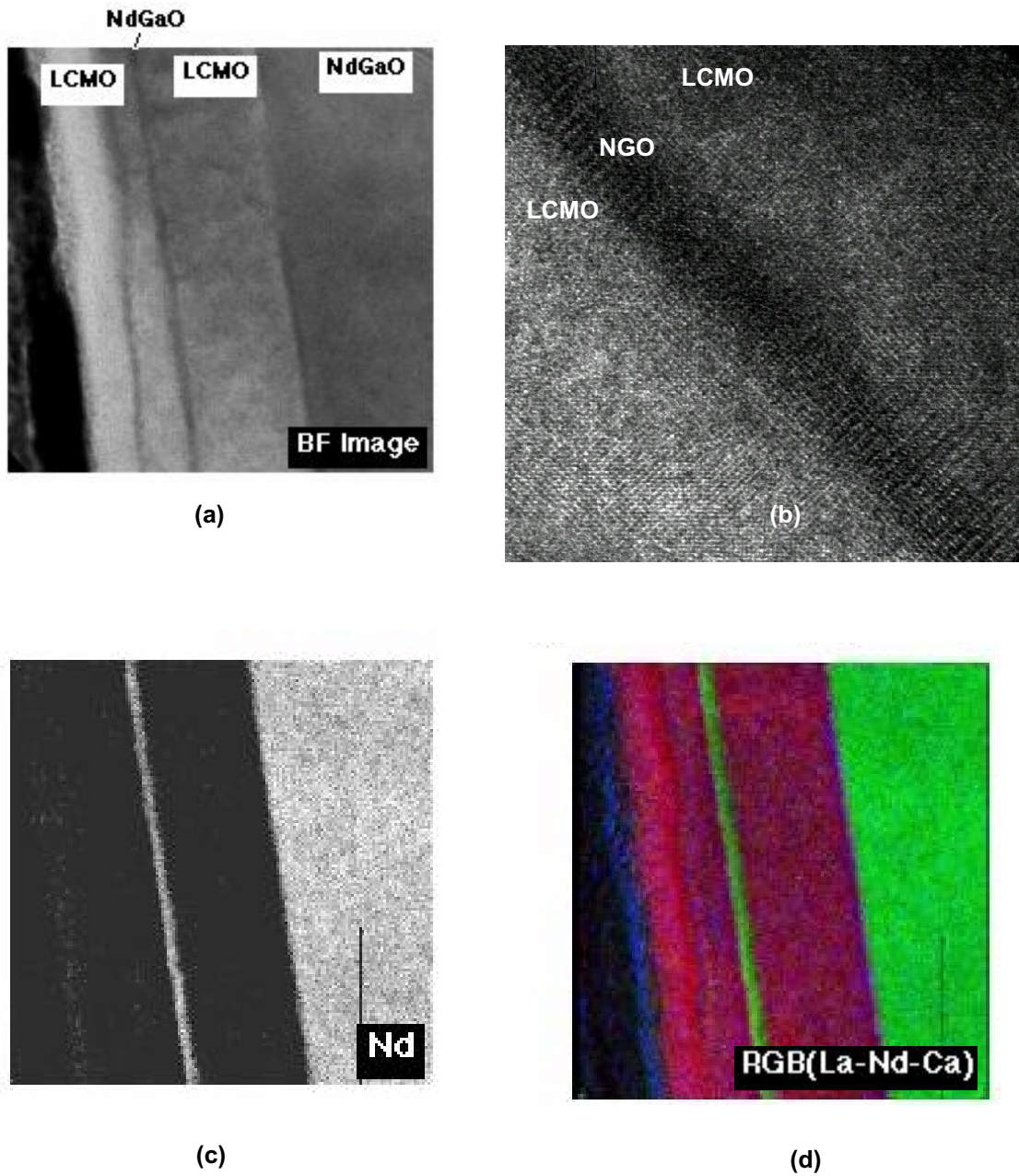


**Fig. 5.2.** (a) Bright field TEM image of the cross-sectional LCMO/NdGaO<sub>3</sub>/LCMO trilayer, (b) the chemical composition map for the Nd  $M_5$  energy loss edge of (a), (c) the colour (red-green-blue) mapping of (c) and (d) the high resolution lattice image at the interface. (Collaboration with by D. Ozkaya and A. K. Petford-Long at University of Oxford)

### 5.3 Very high magnetoresistance and coherent switching

All the devices measured showed very large magnetoresistance at low temperatures, with extremely sharp switching between the low and high resistance states which is assumed to correspond to parallel and anti-parallel alignment of the magnetizations of the two LCMO electrodes. Figure 5.3(a) shows the resistance at 77K versus magnetic field of a  $6 \times 6 \mu\text{m}^2$  junctions. Two striking characteristics are evident: firstly, the measured TMR  $\{(R_{ap} - R_p)/R_{ap}\}$  is up to 86%;  $\{i.e. a factor of 7.3 \text{ between the parallel } (R_p) \text{ and antiparallel } (R_{ap}) \text{ resistance states, } (R_{ap} - R_p)/R_p = 630\%\}$ ; secondly, the switching between these states is extremely sharp  $\{R^{-1}(dR/dH) > 400\%/Oe\}$ . The distinct binary resistance states and switching points in the  $R(H)$  curves, which were stable and reproducible for both magnetic history and thermal cycles, are qualitatively different from any previous magnetic tunnel junction. The reproducible TMR values are higher, and have been achieved at a much higher temperature, than in any previous device.

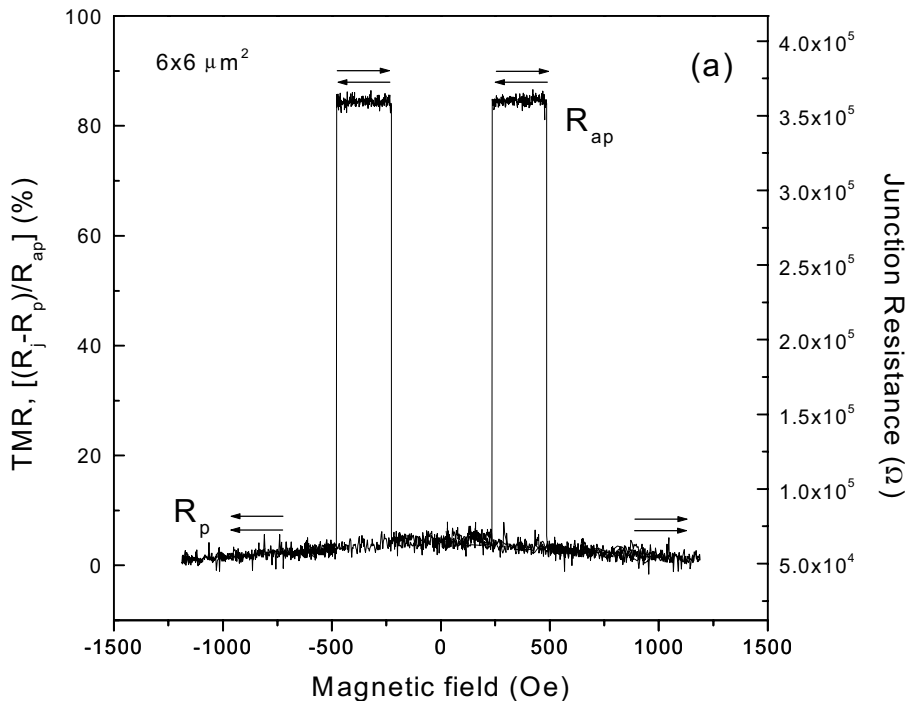


**Fig. 5.3. (a)** The tunnel magnetoresistance, defined as  $(R_j - R_p)/R_{ap}$ , at 77K for the  $6 \times 6 \mu\text{m}^2$   $\text{La}_{0.7}\text{Ca}_{0.3}\text{MnO}_3/\text{NdGaO}_3/\text{La}_{0.7}\text{Ca}_{0.3}\text{MnO}_3$  junction, showing a maximum change of a factor of 7.3 between parallel ( $R_p$ ) and anti-parallel resistances ( $R_{ap}$ ) and the coherently sharp switching at two well-defined fields.

Figure 5.3(b) shows the resistance at 77K versus magnetic field of all the devices on the same chip – See, Fig. 3.2(d). The TMR magnitudes tend to decrease with increasing junction sizes while the junction resistance ( $R_p$ ) - area products of the junctions are more or less unvaried. This indicates that at larger junctions there are some degree of deviation from ideal anti-parallel alignment of the magnetizations between the top and the bottom electrode. Switching fields of various junctions, particularly the higher switching fields,  $H_{c2}$  varies whilst the lower switching field  $H_{c1}$  remains relatively unchanged. The value of  $H_{c1}$  agrees well with the coercive field of a plain LCMO film measured using a SQUID magnetometer. This suggests that  $H_{c1}$  is associated with the switching of the common base electrode, whereas devices whose top electrodes are of different sizes and aspect ratios show different values of the higher coercive field. The coherent switching in the R-H curve was qualitatively unaltered by varying the field direction in the plane of the substrate, although the variation of the coercive fields shows indicates in-plane anisotropy and it will be further discussed in chapter 7.

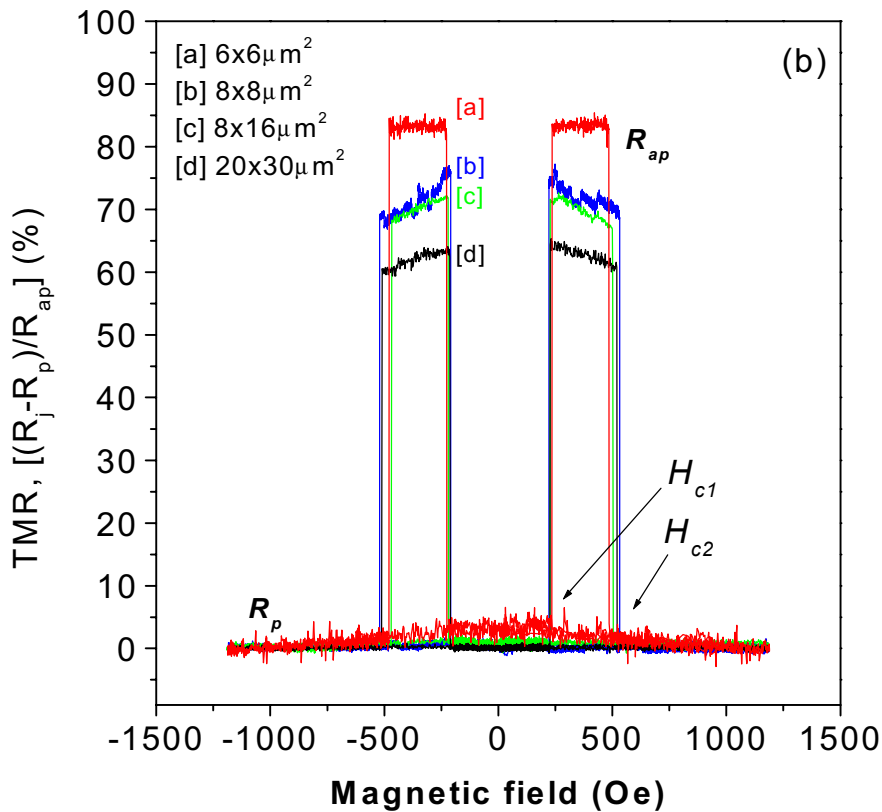


**Fig. 5.3. (b)** The TMR, defined as  $(R_{ap} - R_p)/R_{ap}$ , at 77K for four  $\text{La}_{0.7}\text{Ca}_{0.3}\text{MnO}_3/\text{NdGaO}_3/\text{La}_{0.7}\text{Ca}_{0.3}\text{MnO}_3$  junctions where junction areas are [a]  $6 \times 6 \mu\text{m}^2$ , [b]  $8 \times 8 \mu\text{m}^2$ , [c]  $8 \times 16 \mu\text{m}^2$ , [d]  $20 \times 30 \mu\text{m}^2$ .

## 5.4 Bias and Temperature dependence of the TMR

It is notoriously difficult to prove tunneling unambiguously.<sup>5</sup> However, the dynamic conductance ( $dI/dV$ ) versus voltage for  $R_p$  and  $R_{ap}$  states at different temperatures, shown in Fig. 5.4(a), can be accurately fitted by Simmons' model<sup>9</sup>. Irrespective of area, the antiparallel barrier resistance area product at 77K was between  $2 \times 10^{-6}$  and  $4 \times 10^{-5} \Omega \text{m}^2$ . The TMR effect is suppressed increasing bias voltage as in Fig. 5.4(b). This bias dependent TMR is commonly observed in magnetic tunnel junctions and several possible causes have been suggested such as the projection of the conduction  $d$ -band near the Fermi level, spin flip scattering and spin wave excitations at interfaces. In this study further experiments with higher bias at lower temperatures will be required for a clearer understanding beyond those speculations.

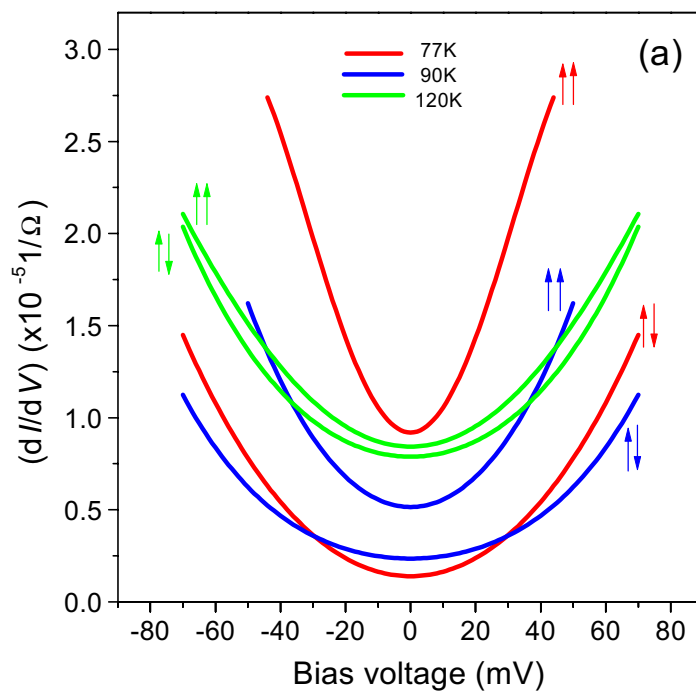


**Fig. 5.4 (a)** The dynamic conductance  $dI/dV$  of junction [a] from Fig. 5.3(b) versus bias voltage for parallel (1000Oe) and anti-parallel (350Oe) spin states at different temperatures. All curves can be accurately fitted by a function of the form  $dI/dV = A + BV^2$  where A and B are constants which dependent on the temperature and magnetisation alignment.

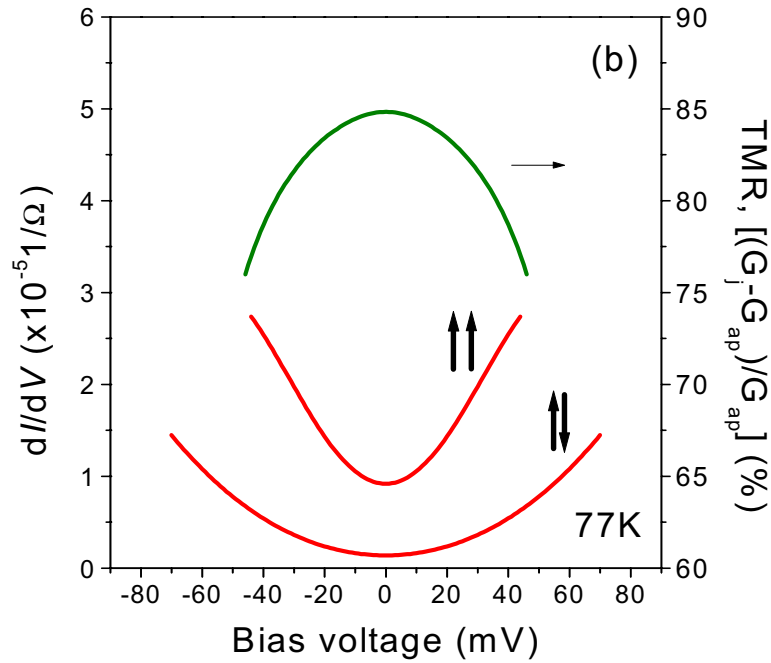


**Fig. 5.4. (b)** The TMR and the dynamic conductance  $dI/dV$  of junction [a] from Fig. 5.3(b) versus bias voltage for parallel (1000Oe) and anti-parallel (350Oe) spin states at 77K.

The temperature dependence of the resistance and TMR is presented in Fig. 5.5. By 100K, the TMR is suppressed to about 40% and a measurable TMR disappears above 150K, although the coherent field switching of the resistance state persists whilst there is a measurable MR. A decrease of TMR with increasing temperature is universal in all magnetic tunnelling junction systems, but appears particularly drastic in manganite half metallic systems.<sup>3-5</sup> Above 120K the temperature dependence of the junction resistance indicates the development of an thermally activated conductance (Fig. 5.5), which can be attributed to the presence of shunting resistance due to defective states in the  $\text{NdGaO}_3$  barrier. However the significant change of the TMR occurs below 120K and thus shunting alone cannot explain the temperature dependent junction resistance. It is also very interesting to note that the temperature-dependence of the junction resistances is significantly different for the parallel magnetization ( $R_p$ ) and for the anti-parallel magnetization ( $R_{ap}$ ). The  $R_{ap}$  shows the maximum around 100K, and then falls off at lower temperatures whilst the  $R_p$  monotonically increases with decreasing temperature. This bifurcation is indeed responsible for the observed large TMR at low temperatures ( $T > 77\text{K}$ ).

A convincing model for spin tunnelling was first formulated by Jullière<sup>10</sup>. This model is based only on the effective spin polarisation at the Fermi energy ( $E_F$ ) so that for identical electrodes the zero bias conductance is given by

$$R_p^{-1} = M(D_{\uparrow}^2(E_F) + D_{\downarrow}^2(E_F)), R_{ap}^{-1} = 2MD_{\uparrow}(E_F)D_{\downarrow}(E_F), \quad [5.1]$$

where  $D_{\uparrow}(E)$  and  $D_{\downarrow}(E)$  are the spin up and spin down density of states and  $M$  is the tunnelling probability. Thus the TMR is given by

$$\Delta R / R_{ap} = (R_{ap} - R_p) / R_{ap} = 2P^2 / (1 + P^2), \quad [5.2]$$

where  $P$  is the spin polarisation given by  $P = \{D_{\uparrow}(E_F) - D_{\downarrow}(E_F)\} / \{D_{\uparrow}(E_F) + D_{\downarrow}(E_F)\}$ .

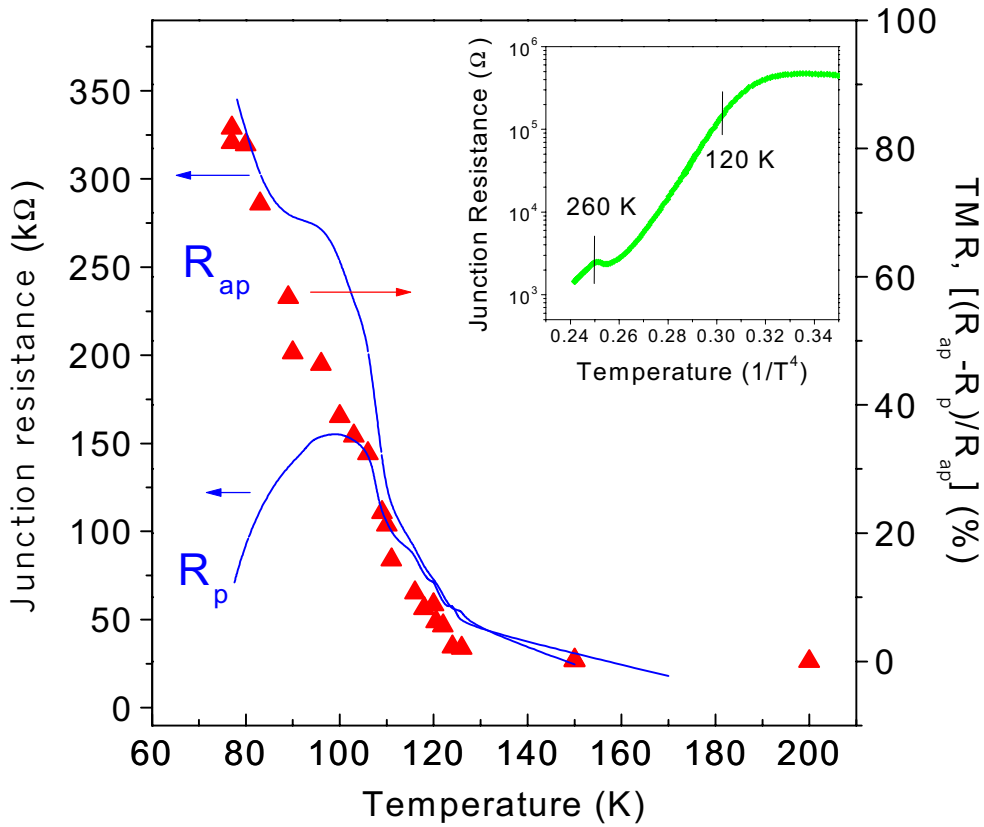


**Fig. 5.5.** The temperature dependence of the junction resistance in parallel (1000Oe) and anti-parallel (350Oe) spin configurations (continuous lines) and the corresponding temperature dependent tunnel magnetoresistance for two different junctions (symbols). The inset shows that the junction resistance scales with  $T^{-4}$  above 120K.

Using Eq. 5.2, the apparent polarisation is plotted as a function of temperature in Fig. 5.6. The maximum polarisation in the LCMO electrodes from the data in Fig. 5.3(a) was 0.86 at 77K. Although the band structure of  $\text{La}_{1-x}\text{Ca}_x\text{MnO}_3$  has been calculated and predicted to be essentially half-metallic at low temperatures,<sup>1,2,11</sup> the value in this study is very much higher than any other report for manganite tunnel junctions at this temperature<sup>3-5</sup>. In Fig. 5.6, the polarisation measured by Park *et al.*<sup>12</sup> by spin-polarised photoemission is also shown. Their data is normalised to the lowest temperature (10K) value, and so the curve represents an upper bound to the actual polarisation. From the comparison, it is evident that the two curves cross, and that in the lowest temperature range to which I could measure, the value of this study is unexpectedly above even this upper bound. Indeed, our inferred spin polarisation at 77K is more than the value of 78-80% in  $\text{La}_{0.7}\text{Sr}_{0.3}\text{MnO}_3$  measured directly by Andreev reflection at 4.2K by Soulen *et al.*<sup>6</sup> and Osofsky *et al.*<sup>13</sup>

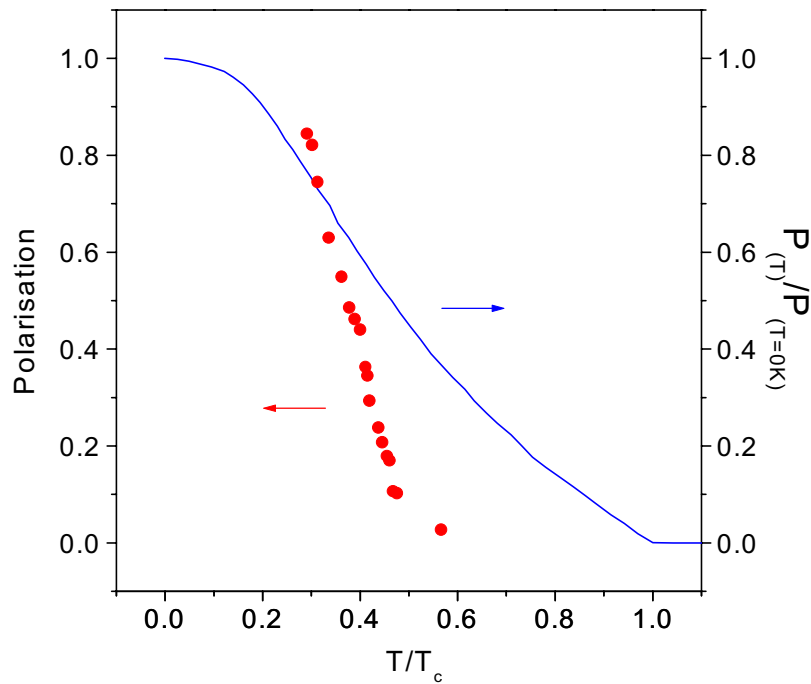


**Fig. 5.6.** The temperature dependent polarisation derived from the observed TMR using Eq. 5.2 is compared to the spin anisotropy of a  $\text{La}_{0.7}\text{Sr}_{0.3}\text{MnO}_3$  thin film measured by spin-polarised photoemission. (After Ref. [12].)

## 5.5 Surface and interface of manganites

The temperature dependence of the TMR (and also the inferred polarisation), which falls off rapidly with increasing temperature even well below  $T_C$  as aforementioned above, is rather disappointing. The temperature dependence of TMR must be related to the temperature dependent surface magnetization. Park *et al.* investigated of a  $\text{La}_{0.7}\text{Sr}_{0.3}\text{MnO}_3$  thin film inferred from spin-resolved photoemission measurements; thus the spin anisotropy in Fig. 5.6 represents the temperature dependent surface magnetization. They found that the surface magnetization decay much faster with increasing temperature ( $T < T_C$ ) than the bulk magnetization.<sup>12</sup> Calderón *et al.* analysed the surface electronic and magnetic states of doped manganites in terms of the loss of cubic symmetry around the Mn ions and they also observed a similar temperature dependent surface magnetization.<sup>14</sup> The suppression of TMR with increasing temperature is commonly observed in magnetic tunnel junctions and it is often attributed to inelastic tunnelling processes such as hopping through defective states in the barrier or interfacial spin scattering. In Fig. 5.7 the normalized MR for various tunnel junction systems are plotted as a function of the

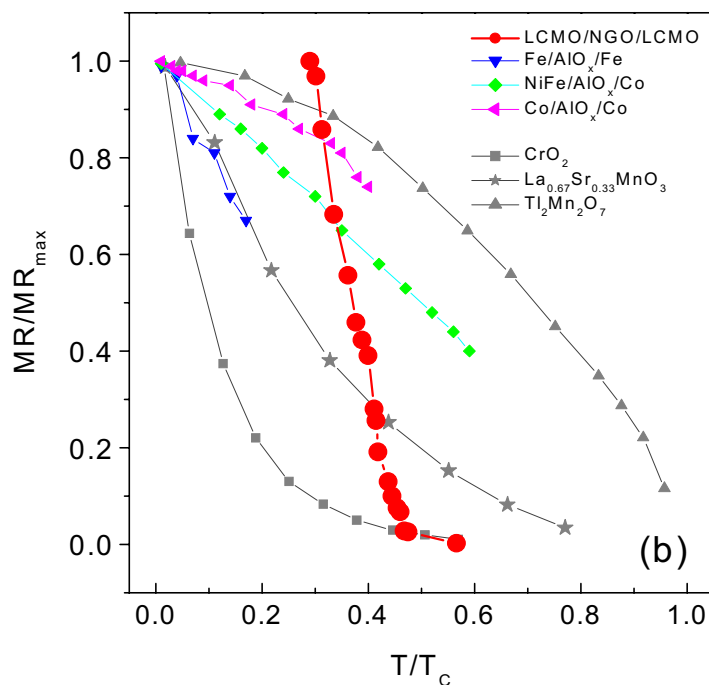


**Fig. 5.7.** The  $\text{MR}/\text{MR}_{\text{max}}$  ratio in this study is also compared to those reported from other ferromagnetic systems. Grey data represent the inter-granular TMR in polycrystalline oxides at the high field measurements. (Reproduced from Ref. [15].)

normalized temperature. The drastic suppression of the TMR in this study is clearly noticeable while the other junctions show a rather weak dependence.

From Fig. 5.6 and 5.7, it is evident that the temperature dependent decay of the TMR in the present junction is much more faster than that of the surface magnetization and its origin must be qualitatively different from a conventional understanding based on inelastic tunnelling components.

In Jullière's model for the calculation of polarisation, it is assumed that the magnetic order in the ferromagnetic electrodes is uniform and thus (spin-polarised) tunnelling is spatially homogeneous within the electrodes. In the following section I discuss the potential role of phase-inhomogeneity to account for the observed temperature dependence of the TMR.

## 5.6 The role of phase-separation

Transport measurements of manganite thin films and multilayers suggest a reduced  $T_C$  associated with lattice-mismatch and the existence of a magnetically inactive surface layer.<sup>16</sup> However, the magnetic measurements of LCMO thin films and multilayers grown on  $\text{SrTiO}_3$  in the previous chapter demonstrate that within such surface layers there are regions that are highly ordered, but that these regions must be electrically discontinuous. This spatial inhomogeneity is reminiscent of phase separation<sup>17</sup> for which there is direct evidence in a number of manganite systems.<sup>18,19</sup> In a tunnel junction, since significant tunnelling can only occur between both metallic and magnetically ordered regions, the extent and distribution of the ferromagnetic regions will critically affect the total tunnel current. Static conductivity contrast images of strained LCMO films taken by Fäth *et al.*<sup>18</sup> in Fig. 5.8 show that metallic regions grow both with decreasing temperature and increasing field. It was also found that some insulating regions still persist even at low temperatures well below  $T_C$ .

Here I suggest a phenomenological tunnelling mechanism based on percolative phase separation playing a dominant role accounting for the general TMR temperature dependence in these materials. If there is inhomogeneous multiphase coexistence in the LCMO, where its relative distribution would depend on temperatures and magnetic fields in a percolative manner, significant tunnelling at low temperatures ( $T < T_C$ ) will only occur with the growth of the ordered ferromagnetic (FM) surface phase. This is illustrated schematically in Fig. 5.9. Since the parallel

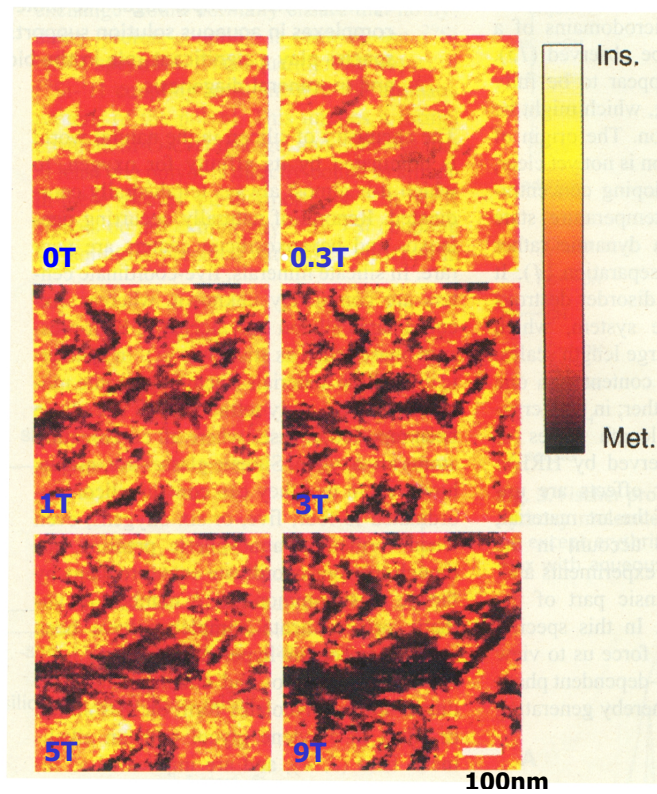


**Fig. 5.8.** Conductivity contrast images of a thin  $\text{La}_{0.7}\text{Ca}_{0.3}\text{MnO}_3$  film on  $\text{SrTiO}_3$  just below  $T_C$  as a function of magnetic fields. Bright yellow and dark black color mapping represent spatial distribution of insulating and metallic regions. (After Ref. [18].)

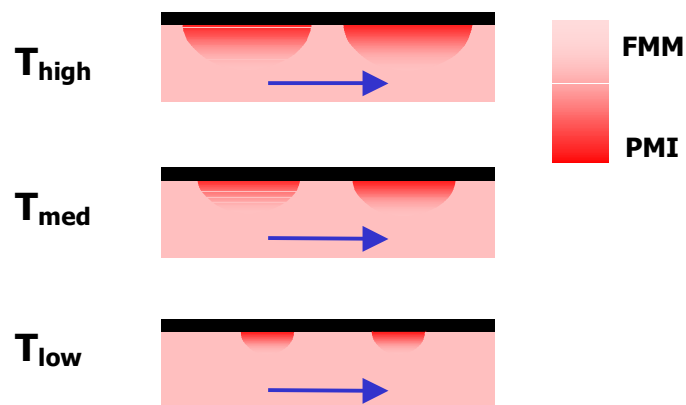


**Fig. 5.9.** A phenomenological model of spin polarised tunnelling based on percolative phase separation between ferromagnetic metal (FMM) regions and paramagnetic insulating (PMI) regions.

configuration has a low resistance-area product, the percolative growth of FM regions provides

---

an immediate explanation of the rapid fall in  $R_p$  with decreasing temperature beyond a certain (percolation) threshold temperature of around 100K. Since the degree of strain, and hence surface  $T_C$  suppression, is much smaller in the present devices with  $\text{NdGaO}_3$  barriers one would expect generally higher MR values than those with lattice-mismatched barriers.<sup>3-5</sup>

The inhomogeneous magnetic state in both electrodes of a tunnel junction raises the question of their mutual alignment. If the relative alignment of the FM regions across the barrier were sensitive to the macroscopic magnetic alignment of the electrodes, then the effective area of the junction would be different in the parallel and antiparallel states; a larger effective tunnel area when the moments were aligned would enhance the MR and hence the inferred polarisation could be substantially increased - as observed in this study. This is particularly critical at high temperatures when the FM area is relatively small, and provides a further reason for the rapid decay in MR with increasing temperature. Nevertheless a further experiment on the sensitivity of phase separation to magnetic-field strength, particularly in the low field range will be needed in order to more qualitatively address the question on the mutual alignment varying to the magnetic field.

## REFERENCES

- 
- <sup>1</sup> J.Y.T. Wei, N.-C. Yeh, and R.P. Vasquez, *Phys. Rev. Lett.* **79**, 5150 (1997).
- <sup>2</sup> Y. Okimoto, K. Katsufuji, T. Ishikawa, A. Urushibara, T. Arima and Y. Tokura, *Phys. Rev. Lett.* **75**, 109 (1995).
- <sup>3</sup> Y. Lu, X. W. Li, G. Q. Gong, Gang Xiao, A. Gupta, P. Lecoeur, J. Z. Sun, Y. Y. Wang and V. P. Dravid, *Phys. Rev. B.* **54**, R8357 (1996) and J.Z. Sun, *Phil. Trans. Roy. Soc. A* **356**, 1693 (1998).
- <sup>4</sup> M. Viret, M. Drouet, J. Nassar, J.P. Coutour, C. Fermon, and A. Fert, *Europhys. Lett.* **39**, 545 (1997).
- <sup>5</sup> T. Obata, T. Manako, Y. Shimakawa and Y. Kubo, *Appl. Phys. Lett.* **74**, 290 (1999).
- <sup>6</sup> R. J. Jr. Soulen, J.M. Byers, M.S. Osofsky, B. Nadgorny, T. Ambrose, S.F. Cheong, P.R. Broussard, C.T. Tanaka, J. Nowak, J.S. Moodera, A. Barry and J.M.D. Coey, *Science* **282**, 85 (1998).
- <sup>7</sup> M.-H. Jo, N.D. Mathur, J.E. Evetts and M.G. Blamire, *Appl. Phys. Lett.* **75**, 3689 (1999).
- <sup>8</sup> R.J.M. van der Veerdonk, J. Norwak, R. Meservey, J.S. Moodera, and W.J.M. de Jonge, *Appl. Phys. Lett.* **71**, 2839 (1997).
- <sup>9</sup> J.G. Simmons, *J. Appl. Phys.* **34**, 1793 (1963).
- <sup>10</sup> M. Jullière, *Phys. Lett. A* **54**, 225 (1975).
- <sup>11</sup> J.Y. Wei, N.-C. Yeh, R. P. Vasquez, and A. Gupta., *J. Appl. Phys.* **83**, 7366 (1998).
- <sup>12</sup> J.H. Park, E. Vescovo, H.-J. Kim, C. Kwon, R. Ramesh and T. Venkatesan, *Nature* **392**, 794 (1998) and J.H. Park, E. Vescovo, H.-J. Kim, C. Kwon, R. Ramesh and T. Venkatesan,, *Phys. Rev. Lett.* **81**, 1953 (1998).
- <sup>13</sup> M.S. Osofsky, B. Nadgorny, R. J. Soulen, Jr., P. Broussard, M. Rubinstein, J. Byers, G. Laprade, Y.M. Mukovskii, D. Shulyatev, and A. Arsenov, *J. Appl. Phys.* **85**, 5567-5569 (1999)
- <sup>14</sup> M.J. Calderón, L. Brey and F. Guinea, *Phys. Rev. B.* **60**, 6698 (1999).
- <sup>15</sup> for Fe/AlO<sub>x</sub>/Fe, T. Miyazaki and N. Tesuka, *J. Magn. Magn. Mater.* **139**, 231 (1995); for NiFe/AlO<sub>x</sub>/Co, Y. Lu, X.W. Li, G. Xiao, R.A. Altman, W.J. Gallagher, A. Marley, K. Roche and S.S.P. Parkin, *J. Appl. Phys.* **83**, 6515 (1998); for Co/AlO<sub>x</sub>/Co, C.H. Shang, G.P. Berera and J.S. Moodera, *Appl. Phys. Lett.* **72**, 605 (1998); for CrO<sub>2</sub> H.Y. Hwang and S.-W. Cheong, *Science* **278**, 1607 (1997); for La<sub>0.67</sub>Sr<sub>0.33</sub>MnO<sub>3</sub> H.Y. Hwang, S.-W. Cheong, N.P. Ong and B. Batlogg, *Phys. Rev. Lett.* **75**, 3336 (1995); for Tl<sub>2</sub>Mn<sub>2</sub>O<sub>7</sub> H.Y. Hwang and S.-W. Cheong, *Nature* **389**, 942 (1997).
-

- <sup>16</sup> J.Z. Sun, D.W. Abraham, K. Roche and S.S.P. Parkin, *Appl. Phys. Lett.* **74**, 3017 (1999).
- <sup>17</sup> A. Moreo, S. Yunoki and E. Dagotto, *Science* **283**, 2034 (1999).
- <sup>18</sup> M. Uehara, S. Mori, C.H. Chen and S-W. Cheong, *Nature* **399**, 560 (1999).
- <sup>19</sup> M. Fäth, S. Freisam, A.A. Menovski, Y. Tomioka, J. Aarts and J.A. Mydosh, *Science* **285**, 1540 (1999).

## CHAPTER 6

## Spin and Charge Modulated Tunnel Junctions:

 $\text{La}_{0.7}\text{Ca}_{0.3}\text{MnO}_3/\text{La}_{0.45}\text{Ca}_{0.55}\text{MnO}_3/\text{La}_{0.7}\text{Ca}_{0.3}\text{MnO}_3$ 

*I have fabricated spin polarised tunnel junctions of all mixed-valence manganites,  $\text{La}_{0.7}\text{Ca}_{0.3}\text{MnO}_3/\text{La}_{0.45}\text{Ca}_{0.55}\text{MnO}_3/\text{La}_{0.7}\text{Ca}_{0.3}\text{MnO}_3$ , in which the ground states of the  $\text{La}_{0.7}\text{Ca}_{0.3}\text{MnO}_3$  (LCMO) and  $\text{La}_{0.45}\text{Ca}_{0.55}\text{MnO}_3$  ( $L_{0.45}C_{0.55}MO$ ) are a ferromagnetic metal and an antiferromagnetic insulator respectively. Although the junction conductance is likely to be influenced by the potential coexistence of mesoscopic metallic and insulating phases in the  $L_{0.45}C_{0.55}MO$  barrier, the tunnel magnetoresistance (TMR) of the device shows a maximum 16.7% with coherent switching at low temperatures. Interestingly the TMR persists up to a higher temperature ( $T/T_C \leq 0.75$ ) compared equivalent non-manganite barrier junctions ( $T/T_C \leq 0.5$ ). Systematic investigation of interface magnetism such as asymmetric magnetization reversal and enhanced coercivity demonstrates the existence of a magnetic coupling at the LCMO/ $L_{0.45}C_{0.55}MO$  interface, which serves as an additional stabilization of the interfacial magnetic order in the LCMO electrode.*

## 6.1 Motivations

The mixed valence manganites,  $\text{La}_{1-x}\text{Ca}_x\text{MnO}_3$  exhibit diverse magnetic and electronic features over the entire range of doping ( $0 \leq x \leq 1$ ) as a result of the intricate interplay among their spin, charge, orbital and lattice degree of freedoms as discussed in the chapter 2.2. In the doping range of ca.  $0.2 \leq x \leq 0.5$ , the ground state of  $\text{La}_{1-x}\text{Ca}_x\text{MnO}_3$  is a ferromagnetic (FM) metal, which can be qualitatively explained by double exchange interaction.<sup>1,2</sup> In the higher doping regimes of  $x \geq 0.5$ , the charges become localized by the ordering of  $\text{Mn}^{3+}$  and  $\text{Mn}^{4+}$  cations on specific lattice sites which suppresses double exchange and promotes an antiferromagnetic (AFM) interaction.<sup>1</sup> The optimally doped  $\text{La}_{0.7}\text{Ca}_{0.3}\text{MnO}_3$  (LCMO) is regarded as a good subject for the study of spin polarised tunnelling because of its high spin polarisation.<sup>3,4</sup> Indeed spin polarised tunnel (SPT) junctions incorporating LCMO have yielded reproducibly large tunnel magnetoresistances (TMR) at low temperatures: however the TMR is suppressed drastically with increasing temperature and does not persist close to the Curie temperature ( $T_C$ ). A probable explanation can be found in the interfacial electronic- and magnetic-structure of LCMO, both of which are critical for spin-polarised tunnelling. For example, local strain at interfaces<sup>4</sup> or a broken bulk-crystal symmetry around the interfacial Mn ions<sup>5</sup> can suppress the bulk-like FM order in LCMO. Furthermore the instability of the electronic and magnetic phase homogeneity appears to be more pronounced at surfaces and interfaces.<sup>6,7,8</sup>

Here in this study I describe an all-manganite trilayer LCMO/ $\text{La}_{0.45}\text{Ca}_{0.55}\text{MnO}_3$ /LCMO junction. The chosen barrier material,  $\text{La}_{0.45}\text{Ca}_{0.55}\text{MnO}_3$  ( $\text{L}_{0.45}\text{C}_{0.55}\text{MO}$ ) is *macroscopically* an antiferromagnetic (AFM) insulator in the ground state (Néel temperature,  $T_N \sim 210\text{K}$ ) via a charge ordered insulator phase from a paramagnetic insulator at higher temperatures as shown in Fig. 6.1. Although the AFM structure of  $\text{L}_{0.45}\text{C}_{0.55}\text{MO}$  in the microscopic level has not been fully characterized, I note that the  $\text{La}_{1-x}\text{Ca}_x\text{MnO}_3$  at  $x=0.5$  has been known to be a CE-type antiferromagnet, i.e. both the charges and the spins of  $\text{Mn}^{3+}$  and  $\text{Mn}^{4+}$  are ordered and the AFM ordering between the Mn ions prevails along the  $x$ ,  $y$  and  $z$  (orthorhombic) crystallographic directions.<sup>9,10</sup>

Overall, across the heteroepitaxial structure, the electrical and magnetic structure is modulated only by the different mixed valence ratio of  $\text{Mn}^{3+}/\text{Mn}^{4+}$ , i.e. a FM metal - an AFM insulator - a FM metal. Thus the bulk crystal symmetry of the Mn ions in the LCMO can be quasi-coherently preserved at interfaces with a small-lattice mismatch ( $\Delta a/a < 0.3\%$  at room temperature), e.g. interfacial chemical bonds between LCMO and  $\text{La}_{0.45}\text{Ca}_{0.55}\text{MnO}_3$ .

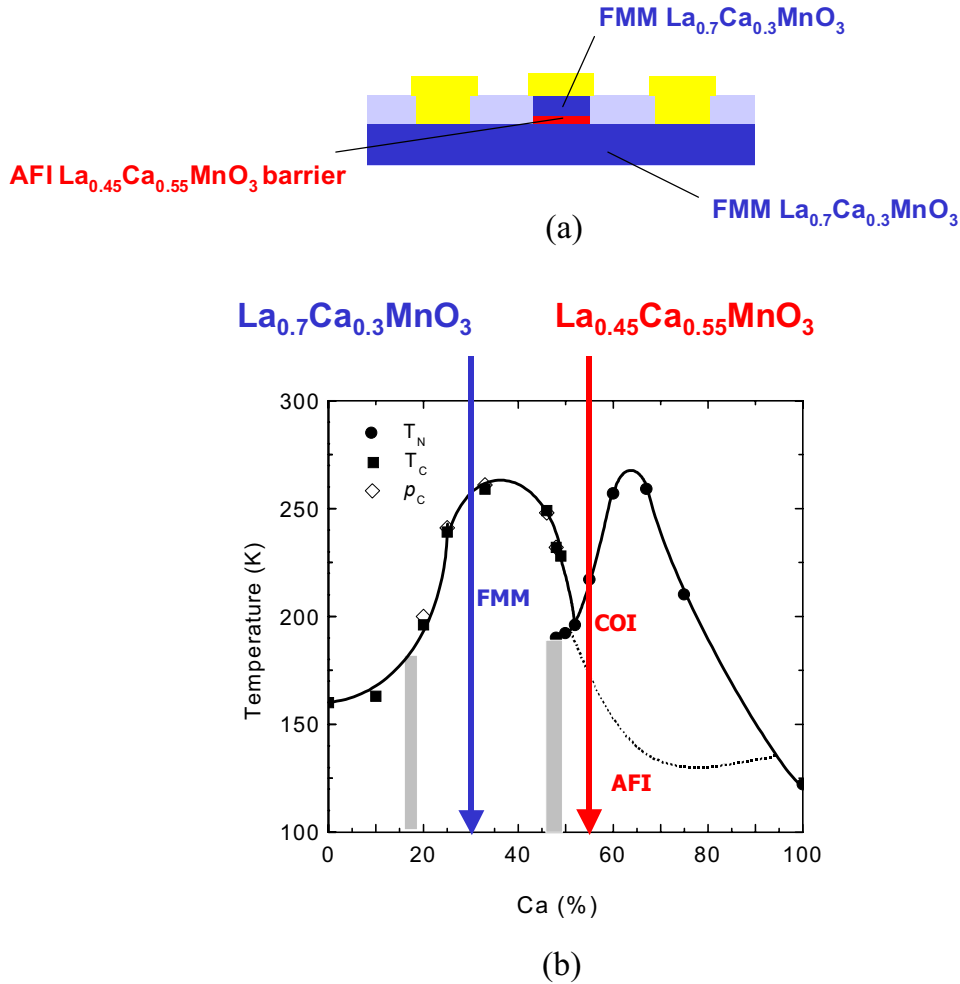
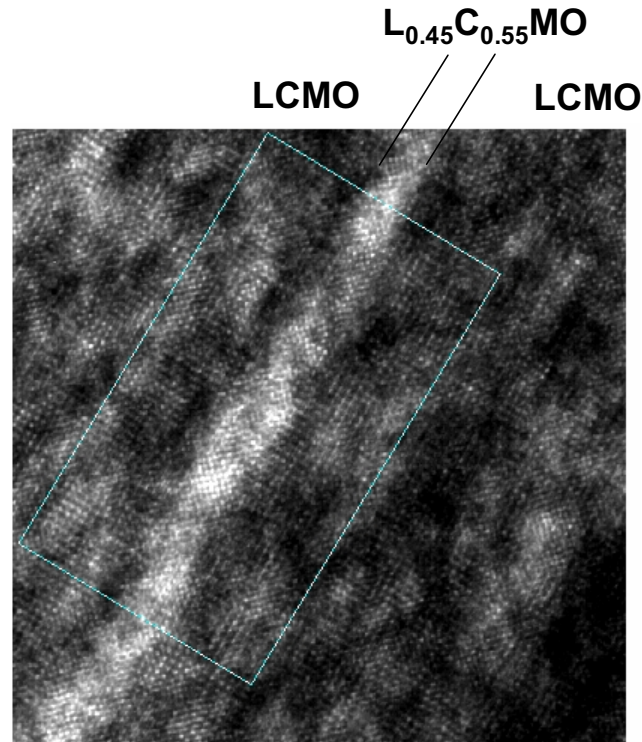


**Fig. 6.1.** (a) The magnetic and electrical structure of the trilayer structure in this study. FMM and AFI denote a ferromagnetic metal and an antiferromagnetic insulator as seen in (b) the phase diagram of  $\text{La}_{1-x}\text{Ca}_x\text{MnO}_3$  ( $0 \leq x \leq 1$ ).  $T_N$  and  $T_C$  are Néel temperature and Curie temperature, and  $\rho_C$  is the resistivity peak temperature. (After Ref. [11].)

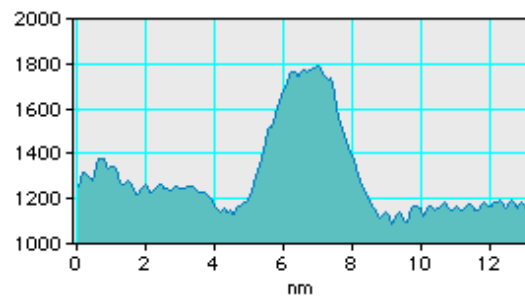
## 6.2 Heteroepitaxy of $\text{La}_{0.7}\text{Ca}_{0.3}\text{MnO}_3/\text{La}_{0.45}\text{Ca}_{0.55}\text{MnO}_3/\text{La}_{0.7}\text{Ca}_{0.3}\text{MnO}_3$

LCMO/ $\text{La}_{0.45}\text{Ca}_{0.55}\text{MO}$ /LCMO trilayers were *in-situ* grown on (001)  $\text{NdGaO}_3$  (NGO) by pulsed laser deposition (KrF laser, 248 nm) using stoichiometric targets with layer thickness of 60nm/3-6nm/80nm. In Fig. 6.2, a high resolution cross-sectional transmission electron

microscopy near the interface demonstrates a fairly good heteroepitaxial quality of the trilayer. The energy-filtered line profile (averaged over 400 lines in the box) of Ca  $L_{2,3}$  energy loss edge across the barrier reveals the appropriate chemical modulation of the Ca ions at the interface. The surface atomic force microscopy scan of the trilayer in Fig. 6.3 also shows a typical layer-by-layer growth mode confirming atomically flat interfaces.



(a)



(b)

**Fig. 6.2.** (a) The cross-sectional high resolution transmission electron microscopy image of the LCMO/ $L_{0.45}C_{0.55}MnO$ /LCMO trilayer and (b) the averaged energy-filtered TEM line profile (averaged over 400 lines in the box) of Ca  $L_{2,3}$  energy loss edge across the barrier. (Collaboration with D. Ozkaya and A. K. Petford-Long at University of Oxford).

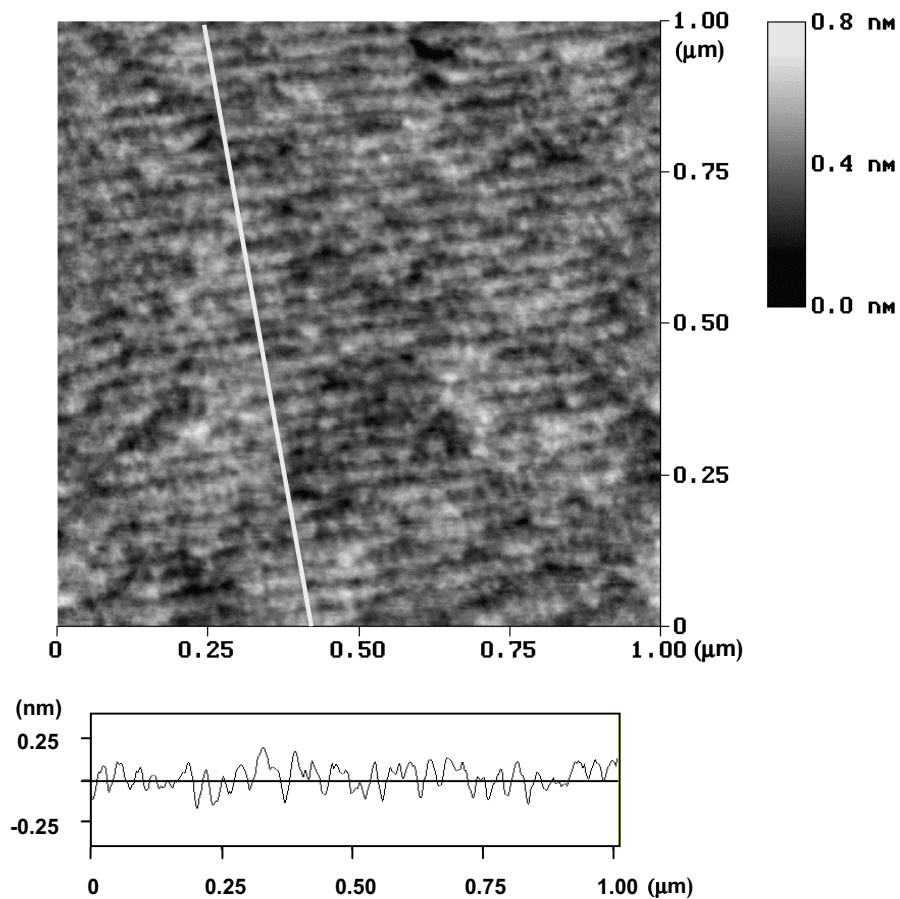


**Fig. 6.3.** The AFM surface image of the trilayer reveals a layer-by-layer growth maintaining a typical step and terrace feature of a pseudocubic perovskite.

Devices were patterned using optical lithography and Ar ion milling to produce micron-scale square mesas. Electrical measurements of the junctions were performed using four terminal AC measurements and magnetic measurements were done with a commercial SQUID magnetometer. For all the measurements in the study, the magnetic field was applied parallel to the plane of the samples.

### 6.3 TMR of $\text{La}_{0.7}\text{Ca}_{0.3}\text{MnO}_3/\text{La}_{0.45}\text{Ca}_{0.55}\text{MnO}_3/\text{La}_{0.7}\text{Ca}_{0.3}\text{MnO}_3$

Figure 6.4 shows the junction resistance of the  $6 \times 6 \mu\text{m}^2$  mesa in the present junction and the temperature dependent resistivity,  $\rho(T)$  of a plain  $\text{La}_{0.45}\text{Ca}_{0.55}\text{MO}$  film and the LCMO base layer. Note that the  $\rho(T)$  of the  $\text{La}_{0.45}\text{Ca}_{0.55}\text{MO}$  film was separately measured from the current-in-plane measurement of a plain 60nm-thick film between 8mm-apart electrical contacts and it exhibits a typical insulating behavior down to low temperature with thermal hysteresis near the  $T_N$ , which is consistent with the literature.<sup>12</sup>

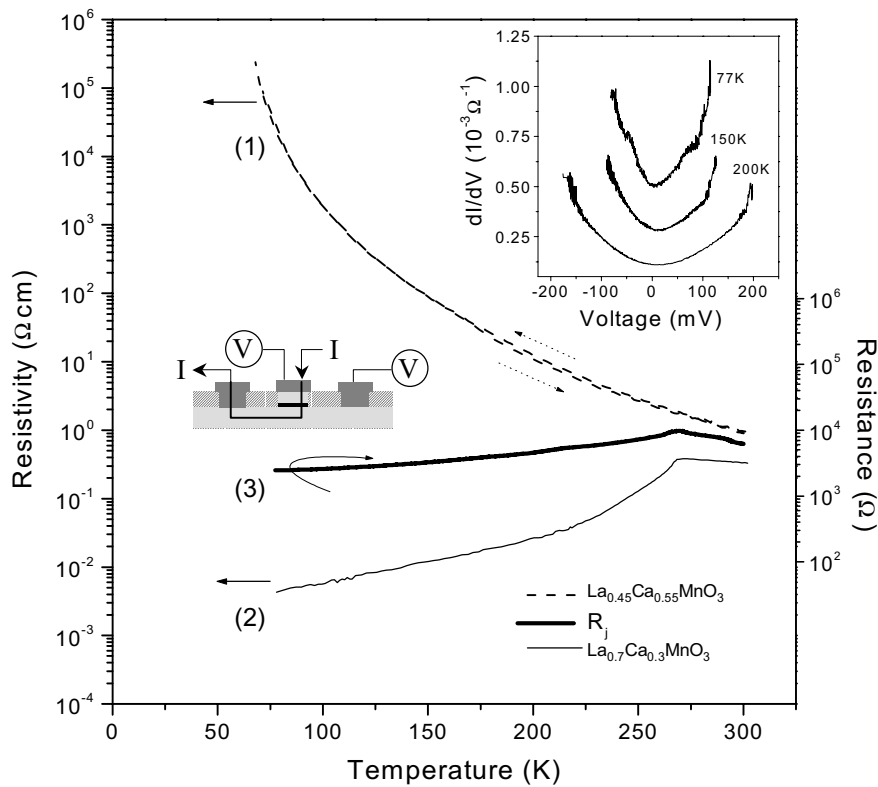


**Fig. 6.4.** The temperature dependent resistivity,  $\rho(T)$  of (1) the 60nm thick  $\text{La}_{0.45}\text{Ca}_{0.55}\text{MnO}_3$  film and (2) a LCMO bottom electrode and (3) the junction resistance of the  $6 \times 6 \mu\text{m}^2$  mesa ( $R_j$ ) of the present junction. The inset shows the dynamic conductance of the junction  $dI/dV$  versus bias voltage at zero field at various temperatures. All curves can be fitted by quadratic functions,  $dI/dV = A + BV^2$  where A and B are constants which dependent on the temperature.

I noticed that the junction resistance at low temperatures is relatively low ( $\sim k\Omega$ ) and its temperature dependence resembles the resistance in series of the electrode and the barrier. This is contrasted to the junction with non-manganite tunnel barriers such as  $\text{SrTiO}_3$  (STO) or  $\text{NdGaO}_3$  (NGO),<sup>6-10</sup> where the junction resistance is mainly governed by the highly insulating barrier ( $\sim M\Omega$ ) below  $T_C$ . It is also qualitatively different from the magnetic tunnel junctions containing magnetic impurities in the tunnel barrier, where spin exchange scattering results in even higher junction resistance.<sup>13</sup> The junction specific resistance (the product of resistance and the junction area) was approximately constant for the junction sizes from  $6 \times 6 \mu\text{m}^2$  to  $20 \times 30 \mu\text{m}^2$  and also systematically scales with barrier thickness of 3-6nm. The dynamic conductance ( $dV/dI$ ) of the junction versus bias voltage shows a quadratic dependence at all measured temperatures as shown in the inset of Fig. 6.4. Therefore it is not inconsistent with the view that the majority of the conduction of the junction is a tunnelling type process.

Figure 6.5 shows the magnetic field dependent tunnel magnetoresistance (TMR) measured at various temperatures above 77K.

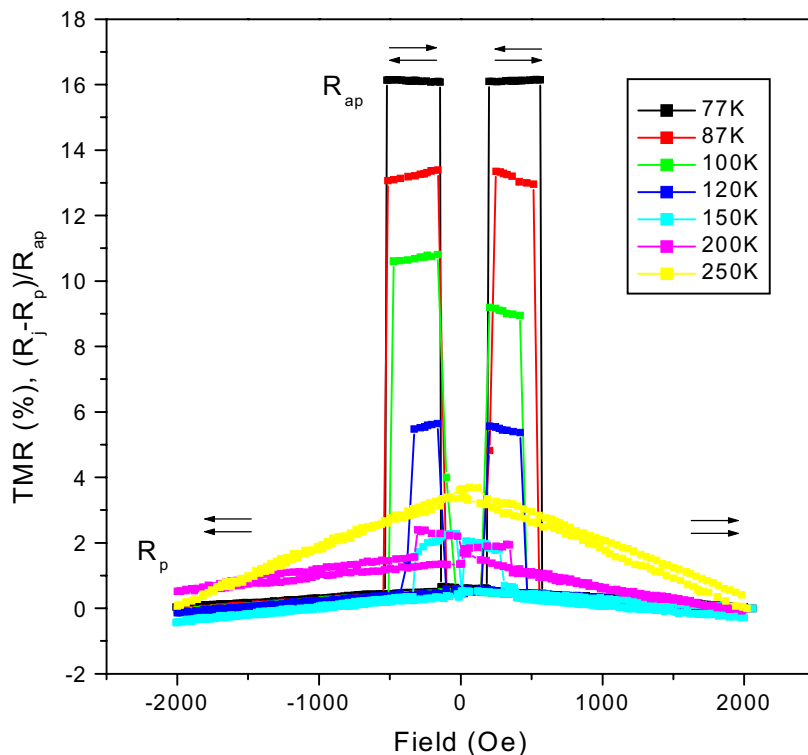


**Fig. 6.5.** The TMR of the LCMO/ $L_{0.45}C_{0.55}MnO$ /LCMO junction at various temperatures.

It displays distinct binary resistance states with sharp switching where the maximum TMR defined as  $(R_{ap} - R_p)/R_{ap}$  is 16.7% at 77K and is suppressed to about 1% at 200K.

$\text{La}_{1-x}\text{Ca}_x\text{MnO}_3$  at  $x \sim 0.5$ , which lies in the phase boundary between FM metallic state ( $x < 0.5$ ) and charge-ordered AFM insulating state ( $x > 0.5$ ) has received extensive interest partly because of the strong competition between dissimilar phases. Indeed the physical properties of  $\text{La}_{1-x}\text{Ca}_x\text{MnO}_3$  near  $x \sim 0.5$  are very sensitive to the slight variance of  $x$ , i.e.  $0.45 < x < 0.55$ .<sup>12,14</sup> More importantly recent experimental evidence on these compositions strongly suggested that the intrinsic multiphase-coexistence of FM metallic and charge-ordered AFM insulating phases in the microscopic level ( $\sim \text{nm}$ ) even at low temperatures.<sup>7</sup>

In this study it was verified that the 60nm-thick  $\text{L}_{0.45}\text{C}_{0.55}\text{MO}$  layer shows a *macroscopically* insulating behavior at low temperatures as seen in Fig. 6.4(1). Nevertheless the *mesoscopic* conductance across the finite length of such an inhomogeneous system must be qualitatively different. Particularly when the carrier conduction length is comparable to the size of chemically or electronically segregated phases in the nm-scale, i.e. the 3-6nm thick barriers in the present junctions, it is likely that the junction conductance is subject to multiphase-fluctuations along the conduction path. This may explain the temperature dependence of the junction resistance in Fig. 6.4(3). Consequently the junction conductance will noticeably deviate from an elastic tunnelling process across a pure insulator, giving rise to the lower junction resistance. When the tunnelling conductance involves significant inelastic components, the TMR can be expected as

$$\text{TMR} = \Delta R^{tot} / R_{ap}^{tot} = (G_p^{tot} - G_{ap}^{tot}) / (G_p^{tot}) = (G_p - G_{ap}) / (G_p + G_i), \quad [6.1]$$

where  $R_i^{tot}$  and  $G_i^{tot}$  are the total resistance and conductance at parallel and anti-parallel spin configurations and  $G_i$  is the inelastic tunnel components. The TMR is therefore reduced by inelastic terms such as the phase fluctuation in the present junction.

In Fig. 6.6, the measured TMR is compared to that of a junction with a NGO barrier<sup>10</sup> in which the TMR was found to be 86% (i.e. the spin polarisation is 0.86 by Jullière's model). Although the maximum TMR in the present study is much lower at 77K, it is surprising to note that the TMR decreases less steeply and persists up to higher temperatures compared with the NGO barrier junction: above 120K the TMR is actually higher, while it still retains a distinct MR effect with a binary switching up to 200K (Fig. 6.5).

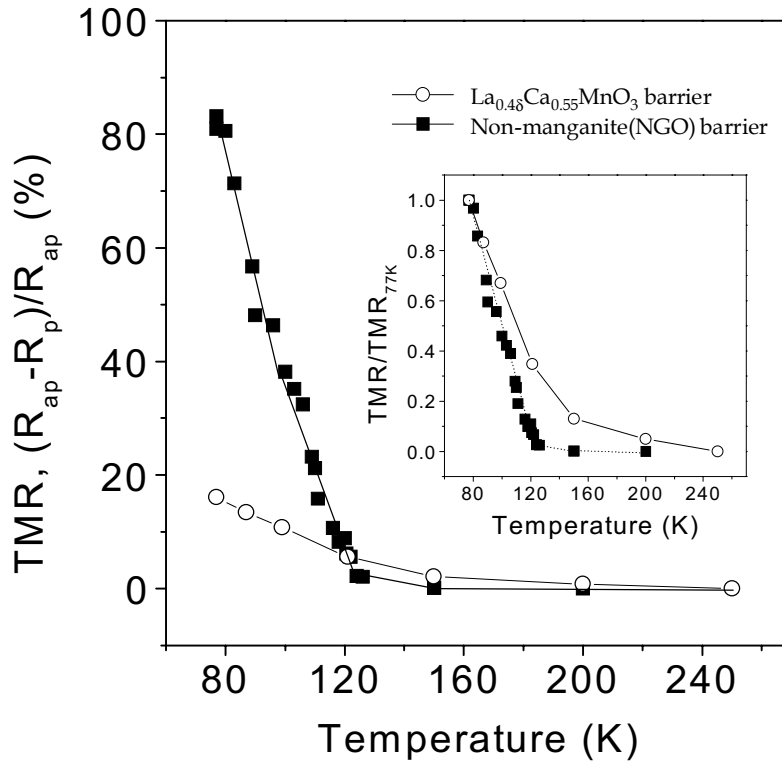


**Fig. 6.6.** The TMR versus temperature for the present junction (a manganite barrier) and a junction with a non-manganite barrier ( $\text{NdGaO}_3$ ) from Ref. [4]. Normalized TMR ( $\text{TMR}/\text{TMR}_{77\text{K}}$ ) data were shown in the inset.

#### 6.4 Interfacial magnetism of $\text{La}_{0.7}\text{Ca}_{0.3}\text{MnO}_3/\text{La}_{0.45}\text{Ca}_{0.55}\text{MnO}_3/\text{La}_{0.7}\text{Ca}_{0.3}\text{MnO}_3$

Interface magnetism in the  $\text{LCMO}/\text{L}_{0.45}\text{C}_{0.55}\text{MO}/\text{LCMO}$  junction, where the barrier is potentially magnetic, can be distinguished from an equivalent non-magnetic barrier junction. The magnetic properties of  $\text{L}_{0.45}\text{C}_{0.55}\text{MO}$ , measured with a plain 60nm-thick film in this study suggest that it is by and large a canted antiferromagnet at low temperatures: it shows an ordering peak at  $\sim 200\text{K}$  in the temperature dependent magnetization, and the magnetization-

field curves exhibits a feeble hysteresis with the saturation magnetic moment of the fraction of  $1.6 \times 10^{-2}$  of the same thickness of LCMO at 10K. Since a probable antiferromagnetism of the barrier material is suggested, I further investigated the mechanism by which interfacial magnetism affects the TMR across the magnetically active barrier based on a potential magnetic coupling between ferromagnetic electrodes and the antiferromagnetic barrier.

In order to investigate interfacial magnetism in LCMO/ $L_{0.45}C_{0.55}MO$ /LCMO trilayers, I chose unpatterned heteroepitaxial trilayers grown on STO (100) rather than ones on NGO (001) mainly because this avoids strong background paramagnetism from  $Nd^{3+}$  during the magnetic measurement. I first explored a possible exchange interaction between the FM electrodes and the AFM barrier by studying magnetization reversal upon an applied field ( $H_{FC}$ ) during the sample cooling to  $T < T_N < T_C$ . The measured magnetization (M) - field (H) hysteresis loops at 77K are shown in Fig. 6.7 and I note that magnetization reversal is asymmetric when the  $H_{FC}$  is zero or relatively small – see, for  $H_{FC} = 0.5kOe$  in Fig. 6.7: it shows dissimilar coercivity

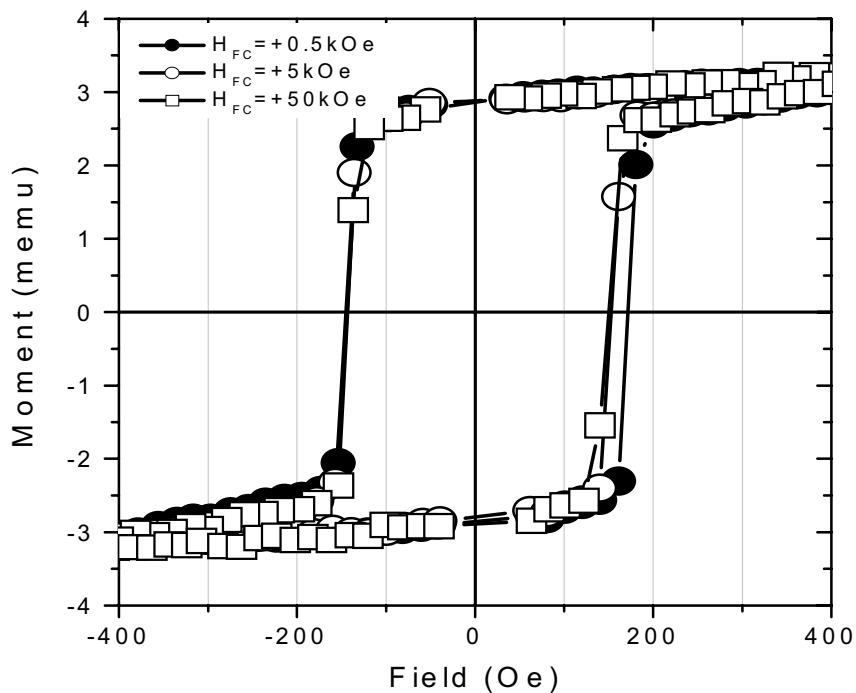


**Fig. 6.7.** Typical M-H loops of the unpatterned LCMO/ $L_{0.45}C_{0.55}MnO$ /LCMO trilayer at various cooling field,  $H_{FC} = +0.5kOe$ ,  $+5kOe$  and  $+50kOe$ . (measured at 77K).

( $H_c$ ) when the field is reversed from positive to negative ( $H_c^+$ ) and from negative to positive ( $H_c^-$ ). This asymmetry was reproducibly observed and persists up to high temperatures until the hysteresis disappears, i.e. up to near the  $T_C$  ( $\sim 260\text{K}$ ) of the FM LCMO.

It was revealed that the asymmetry  $\{\Delta H_{ex} \equiv (H_c^+ + H_c^-)/2\}$  is strongly dependent on the  $H_{FC}$  – see, for  $H_{FC} = 5\text{kOe}$  and  $50\text{kOe}$  in Fig. 6.7. A systematic variation of  $\Delta H_{ex}$  as a function of  $H_{FC}$  is shown in Fig. 6.8(a). However, it should be noted that the sign of the  $\Delta H_{ex}$  is not dependent

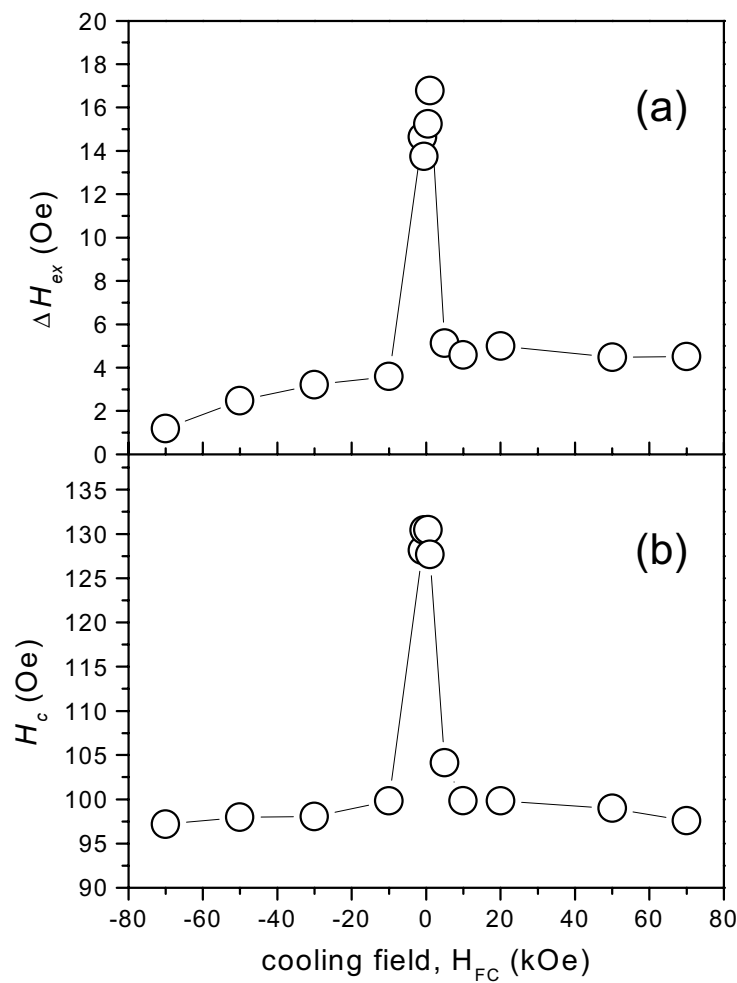


**Fig. 6.8.** (a) The shift in the M-H loops ( $\Delta H_{ex}$ ) and (b) the coercivity ( $H_c$ ) as a function of  $H_{FC}$  at 77K.

on the polarity of the  $H_{FC}$  but instead on the sample orientation with respect to the  $H_{FC}$ . It is qualitatively different from the normal exchange bias where the sign of the  $\Delta H_{ex}$  follows the polarity of the  $H_{FC}$ . It is also distinctive from the reported exchange bias in mixed valence manganites where only the normal exchange bias was observed.<sup>15</sup> The  $H_{FC}$  dependence of the coercivity  $H_c$ , defined as  $H_c \equiv (H_c^+ - H_c^-)/2$ , is shown in Fig. 6.8(b) and it exhibits an essentially the similar variation with the  $H_{ex}$  suggesting a common physical basis. Similar measurements have been done on a plain LCMO film and the  $H_c$  is only weakly dependent on the  $H_{FC}$  as expected from a conventional ferromagnet.

Therefore it is clear that the observed  $H_{FC}$  dependence of  $\Delta H_{ex}$  and  $H_c$  is due to the presence of the AFM  $L_{0.45}C_{0.55}MO$  barrier. The temperature dependent  $H_c$  measured on the LCMO/ $L_{0.45}C_{0.55}MO$ /LCMO along with a LCMO/ $SrTiO_3$ /LCMO and a plain LCMO film are shown in Fig. 6.9 and it distinctively exhibits a strong enhancement of the  $H_c$  at  $\sim 200K$ , which is close to the  $T_N$  of  $L_{0.45}C_{0.55}MO$ .

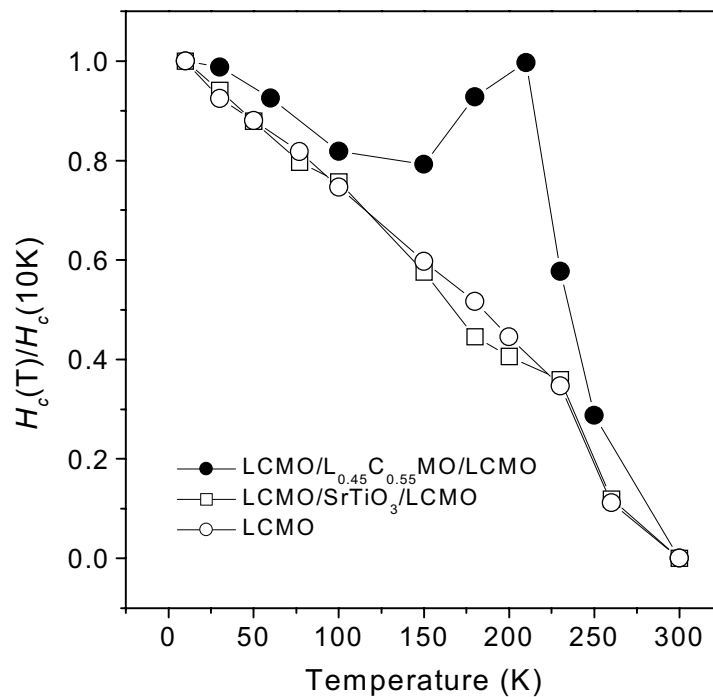


**Fig. 6.9.** The temperature dependent  $H_c$  in an unpatterned LCMO/ $L_{0.45}C_{0.55}MnO$ /LCMO trilayer, an unpatterned LCMO/ $SrTiO_3$ /LCMO trilayer and a plain LCMO film, respectively.

This further corroborates the magnetization reversal of the LCMO/L<sub>0.45</sub>C<sub>0.55</sub>MO/LCMO trilayer is strongly influenced by the presence of the AFM L<sub>0.45</sub>C<sub>0.55</sub>MO barrier. The observed magnetic features aforementioned such as asymmetric magnetization reversal and the  $H_c$  enhancement near the  $T_N$  can be further discussed particularly around the role of the AFM L<sub>0.45</sub>C<sub>0.55</sub>MO barrier.

In conventional *macroscopic* exchange bias systems, it is assumed that the AFM anisotropy is sufficiently large compared to the FM anisotropy and the interfacial exchange coupling constant ( $J_{INT}$ ), i.e.  $K_{AFM}t_{AFM} \gg K_{FM}t_{FM}$  and  $K_{AFM}t_{AFM} \gg J_{INT}$ , where  $K_i$  and  $t_i$  are the anisotropy constant and the thickness of the respective layers. However, if either the  $J_{INT}$  and/or the  $K_{FM}t_{FM}$  is comparable to the  $K_{AFM}t_{AFM}$ , i.e.  $t_{FM} \gg t_{AFM}$ , the magnetization reversal cannot be effectively exchange-biased in the *macroscopic* level. Instead the FM and AFM spins can be coupled, for example, they can be reversed together. Then the magnetization reversal of the system may be strongly influenced by the magnetic microstructures of the AFM, i.e. the domain structures<sup>16</sup> or crystal orientation<sup>17</sup> of the AFM. In fact, a direct observation of the *microscopic* features of an exchange bias system Co/LaFeO<sub>3</sub> reveals that the FM-AFM exchange bias can be a local domain-by-domain interaction; the FM spin directions are locally determined by the spin directions in the underlying AFM layers.<sup>18</sup> An asymmetric magnetization reversal was observed in Fe/MnO<sub>2</sub> bilayers and it was ascribed to the coupling between the magnetization of Fe and the twinned crystal structure of the AFM (110) MnO<sub>2</sub>.<sup>19</sup> It should be noted that in this study the sign of the  $\Delta H_{ex}$  was only dependent on the sample orientation with respect to the  $H_{FC}$ , not on the polarity of the  $H_{FC}$ . This strongly suggests that the similar origin related to the twinned crystal structure of the barrier, which is commonly observed in La<sub>1-x</sub>Ca<sub>x</sub>MnO<sub>3</sub> of  $x \sim 0.5$ ,<sup>20</sup> causes a similar asymmetric reversal in this study.

The magnetic structure of the L<sub>0.45</sub>C<sub>0.55</sub>MO tends to be a multi-phase mixture, i.e. nm-size FM clusters in the AFM matrix at the ground state<sup>21</sup> as discussed above, and this tendency towards phase separation is further pronounced near the phase transition temperature, i.e. the  $T_N$ . A similar coercivity enhancement as in this study was reported in an MnF<sub>2</sub>/Fe exchange-bias bilayer and it was attributed to be due to the interfacial frustration in the AFM MnF<sub>2</sub> driven by the  $H_{FC}$ , which effectively pin the propagating domain wall motions in the Fe.<sup>22</sup> Then the  $H_c$  enhancement of the LCMO near the  $T_N$  of the L<sub>0.45</sub>C<sub>0.55</sub>MO can be understood as the stabilization of the domain structure of the LCMO due to the local pinning torque originated from the maximum magnetic inhomogeneity or frustration in the AFM L<sub>0.45</sub>C<sub>0.55</sub>MO at its magnetic transition.

---

The LCMO- $L_{0.45}C_{0.55}MO$  interface in the present junctions is uniquely defined in that the quasi-continuous interfacial Mn-O-Mn bonds are preserved, while modulating the magnetic structures across them. Although the potential mesoscopic multi-phase coexistence in the  $L_{0.45}C_{0.55}MO$  causes a complex tunnelling process between LCMO layers, the structural and chemical coherence of the interface must be related to the enhanced interfacial FM order in the LCMO, particularly when the FM order is intrinsically inhomogeneous. Furthermore the FM domains pinning due to interfacial exchange interaction between the LCMO and  $L_{0.45}C_{0.55}MO$  seems to provide additional stabilization of the FM order. Particularly the observed enhanced interfacial exchange interaction, as manifest in the  $H_c$  enhancement at the  $T_N$  of the  $L_{0.45}C_{0.55}MO$ , can qualitatively explain the improved temperature dependence of the TMR over the junctions with non-magnetic barrier, i.e.  $SrTiO_3$  or  $NdGaO_3$ .

## REFERENCES

- 
- <sup>1</sup> C. Zener, *Phys. Rev.* **82**, 403 (1951).
- <sup>2</sup> P.W. Anderson and H. Hasegawa, *Phys. Rev.* **100**, 67 (1955).
- <sup>3</sup> J. O'Donnell, A.E. Andrus, S. Oh, V. Collar and J.N. Eckstein, *Appl. Phys. Lett.* **76**, 1914 (1999).
- <sup>4</sup> M.-H. Jo, N.D. Mathur, N.K. Todd and M.G. Blamire, *Phys. Rev. B.* **61**, R14905 (2000).
- <sup>5</sup> M.J. Calderón, L. Brey and F. Guinea, *Phys. Rev. B.* **60**, 6698 (1999).
- <sup>6</sup> M.-H. Jo, N.D. Mathur, J.E. Evetts and M.G. Blamire, *Appl. Phys. Lett.* **75**, 3689 (1999).
- <sup>7</sup> A. Moreo, S. Yunoki and E. Dagotto, *Science* **283**, 2034 (1999) and E. Dagotto, T. Hotta and A. Moreo, cont-mat/0012117 and *Phys. Rep.* to be published.
- <sup>8</sup> N.D. Mathur and P.B. Littlewood, cont-mat/01024238 and to be published in *Solid State Comm.*
- <sup>9</sup> G. Xiao, E.J. McNiff, G.Q. Gong, A. Gupta, C.L. Canedy and J.Z. Sun, *Phys. Rev. B.* **54**, 6073 (1996).
- <sup>10</sup> P.G. Radaelli, D.E. Cox, M. Marezio and S.-W. Cheong *Phys. Rev. B.* **55**, 3015 (1997).
- <sup>11</sup> P. Schiffer, A.P. Ramirez, W. Bao and S.-W. Cheong, *Phys. Rev. Lett.* **75**, 3336 (1995).
- <sup>12</sup> M. Roy, J.F. Mitchell, A.P. Ramirez and P. Schiffer, *J. Phys.: Condens. Matter.* **11**, 4843 (1999)
- <sup>13</sup> R. Jansen and J.S. Moodera, *Phys. Rev. B.* **61**, 9047 (2000).
- <sup>14</sup> Q. Huang, J.W. Lynn, R.W. Erwin, A. Santoro, D.C. Dender, V.N. Smolyaninova, K. Ghosh and R.L. Greens, *Phys. Rev. B.* **61**, 8895 (2000).
- <sup>15</sup> I. Panagiotopoulos, C. Christides, M. Pissas and d. Niarchos, *Phys. Rev. B.* **60**, 485 (1999), K.R. Nikolaev, I.N. Krivorotov, W.K. Cooley, A. Bhattacharya, E. D. Dahlberg and A.M. Goldman, , *Appl. Phys. Lett.* **76**, 478 (2000) and B. Pang, XX Zhang, Z. Xie, H.J. Tao, B. Xu, H. Jiu and B.R. Zhao, *Phys. Rev. B.* **61**, 8955 (2000)..
- <sup>16</sup> S.M. Zhou, K. Liu and C.L. Chien, *Phys. Rev. B.* **58**, 14717 (1998).
- <sup>17</sup> J. Noguees, T.J. Morgan, D. Lederman, Ivan K. Schuller and K.V. Rao *Phys. Rev. B.* **59**, 6984 (1999).
- <sup>18</sup> F. Nolting, A. Scholl, J. Stöhr, J.W. Seo, J. Fompeyrine, H. Siegart, J.-P. Locquet, S. Anders, J. Lünling, E.E. Fullerton, M.F. Toney, M.R. Scheinfein and H.A. Padmore, *Nature* **405**, 767 (2000).
- <sup>19</sup> M.R. Fitzsimmons, P. Yashar, C. Leighton, Ivan K. Schuller, J. Noguees, C.F. Majkrzak and J.A. Dura., *Phys. Rev. Lett.* **84**, 3986 (2000) and C. Leighton, M. Song, J. Noguees, M.C.
-

Cyrille and Ivan K. Schuller, *J. Appl. Phys.* **88**, 344 (2000).

<sup>20</sup> S. Mori, C.H. Chen, and S.-W. Cheong, *Nature* **392**, 473 (1998) and C.H. Chen and S.-W. Cheong, *Phys. Rev. Lett.* **76**, 4042 (1996).

<sup>21</sup> G. Allodi, R De Renzi, F. Licci and M.W. Pieper, *Phys. Rev. Lett.* **81**, 4736 (1998).

<sup>22</sup> C. Leighton, J. Nogues, B.J. Jönsson-Åkerman and Ivan K. Schuller, *Phys. Rev. Lett.* **84**, 3466 (2000).

---

## CHAPTER 7

# Magnetization Reversal Processes in Spin Polarised Tunnel Junctions

---

*Magnetization reversal processes in spin-polarized tunnel (SPT) junctions based on half-metallic  $\text{La}_{0.7}\text{Ca}_{0.3}\text{MnO}_3$  (LCMO) are studied with two-dimensional angular SPT measurements. A large tunnel magnetoresistance in the junctions was found to be highly sensitive to local magnetic fluctuations in the LCMO electrodes. This establishes a one-to-one correlation between the magnetization reversal and the SPT.*

*I have found two different magnetic anisotropies in the top and bottom LCMO electrodes. The large bottom electrode shows uniaxial crystalline anisotropy and the top electrode shows a combination of the uniaxial crystalline anisotropy and biaxial shape anisotropy. Coherent magnetization reversal of the top electrode was assessed within the Stoner-Wohlfarth coherent rotation model.*

*The systematic angular variations of the SPT features in the field dependent resistance curves reveal other important information about the magnetization reversal. Edge-domain pinning is suggested to play a crucial role in the magnetization reversal.*

## 7.1 Introduction

Spin-polarized tunnelling (SPT) exploits the dissimilar conductance between asymmetric spin sub-bands at the Fermi level ( $E_F$ ) in the two metallic ferromagnets across a tunnel barrier. It is commonly assumed that there is a direct correlation between the bulk magnetization-vector and the spin-quantized axis of conduction electrons. Thus it is important to understand the magnetization processes in the ferromagnet electrodes of the junctions under the external magnetic field. Jullière<sup>1</sup> first formulated a simple expression for the SPT between parallel and anti-parallel magnetizations in two ferromagnets. In general the tunnelling conductance has a certain functional form that depends on the relative angle of the two magnetization-vectors. For example Slonczewski<sup>2</sup> predicted the tunnelling conductance  $G$  to be a cosine function of the electronic polarisation and the relative angles ( $\theta$ ) at which the spin state is projected onto to the initial spin state through a spinor transformation (equivalently  $\theta$  being the relative angles of the magnetization between two ferromagnets from):

$$G(\theta) = G'(1 + P_1 P_2 \cos\theta), \quad [7.1]$$

where  $G'$  is a prefactor and  $P_i$  is the effective polarization at the interfaces.

The study of magnetization reversal in SPT junctions has mainly relied on the direct observation of magnetization processes using techniques based on electron transmission microscopy and magnetic force microscopy, in conjunction with magnetic measurements or micromagnetic simulations.<sup>3</sup> In principle it is also possible to establish a one-to-one correlation between the magnetization reversal and the SPT features during SPT measurements, provided that the SPT response to the external field is both simple and is sensitive enough to fully reflect the magnetization states in detail.<sup>4,5</sup> In many cases, however, the SPT junctions lack such sensitivity to local magnetic fluctuation, mainly due to complex magnetization reversal processes.

In the Chapter 5 of the thesis, I demonstrated an unprecedentedly large TMR in the  $\text{La}_{0.7}\text{Ca}_{0.3}\text{MnO}_3$ (LCMO)/ $\text{NdGaO}_3$ (NGO)/LCMO junctions.<sup>6</sup> Such a reproducibly large TMR establishes the distinct, sharp switching between binary junction-resistances. This highly sensitive SPT measurement enables one to probe the magnetic reversal processes. In this Chapter, I report comprehensive magnetic reversal in such junctions, as determined by two-dimensional angular measurements of the tunnel junction resistances: the magnetization reversal process was directly characterized by investigating systematic variations in the SPT features in the field dependent junction resistances during angular SPT measurements.

## 7.2 Two-dimensional angular TMR measurements

Figure 7.1 sketches the two-dimensional angular measurement geometry employed in this study, where each junction resistance ( $R_j$ ) - field (H) curve recorded at a certain angle was traced as a function of the in-plane rotation angle. The  $R_j$ -H curves were measured in four-terminal a.c. measurements and the typical sweep rate of the applied magnetic fields was at 0.5-5 Oe/s.

The uniform magnetization ( $\mathbf{M}$ ) of a small ferromagnet object under a magnetic field ( $\mathbf{H}$ ) is given by

$$E_{\text{tot}}(\mathbf{H}) = -\mathbf{H} \cdot \mathbf{M} + E_K(\theta), \quad [7.2]$$

where  $E_{\text{tot}}$ ,  $E_K$  are the total magnetic energy density and the total anisotropy energy density, and  $\theta$  is the orientation of magnetization. In a static equilibrium the magnetization direction follows the micromagnetic condition of  $\partial E / \partial \theta = 0$  and  $\partial^2 E / \partial \theta^2 > 0$ . In SPT junction measurements, the magnetization in the top and the bottom electrodes are coupled with the external field and their relative alignment can be reflected in the measured tunnel conductance. Therefore, conversely, by varying the coupling between  $\mathbf{H}$  and  $\mathbf{M}$ , the magnetization process can be studied via tunnel conductance measurements. A series of typical  $R_j$ -H curves for a  $6 \times 6 \mu\text{m}$  square mesa at various in-plane rotation angles is shown in Fig. 7.2. The angular dependence of the features of the  $R_j$ -H curves was investigated based on three criteria, namely, the angular variation of [1] the switching fields  $H_{c1}$  and  $H_{c2}$ , [2] the magnitude of the TMR,  $\Delta R / R^*_{ap}$  and [3] the slope of the top plateau  $\{R(H_{c1}) - R(H_{c2})\} / (H_{c1} - H_{c2})$  as indicated in Fig. 7.2. Note that the TMR is normalized with  $R^*_{high}$  which represents the average value of the  $R_{ap}$ , i.e.  $R^*_{ap} = \{R_{ap}(H_{c1}) + R_{ap}(H_{c2})\} / 2$ , as indicated in Fig. 7.2.

I first concentrate on the angular variation of the switching fields. In the  $R_j$ -H curve of the junction, the lower switching field  $H_{c1}$  and the higher switching field  $H_{c2}$  can be associated with the switching of the common base electrode and the top electrode respectively. This was verified from the fact that identical values of the  $H_{c1}$  were found in other devices of different mesa size and aspect ratio on the same chip, while the  $H_{c2}$  varies from junction to junction. Strong magnetostrictive anisotropy in manganites thin films (a change in the crystalline anisotropy under the lattice distortion by stress induced by lattice mismatch with substrates) can sometimes impose a spontaneous out-of-plane magnetization<sup>7</sup>, however I have not observed any sign of it, presumably because of the very small lattice-mismatch in the LCMO films on NGO substrates (less than 0.1%).

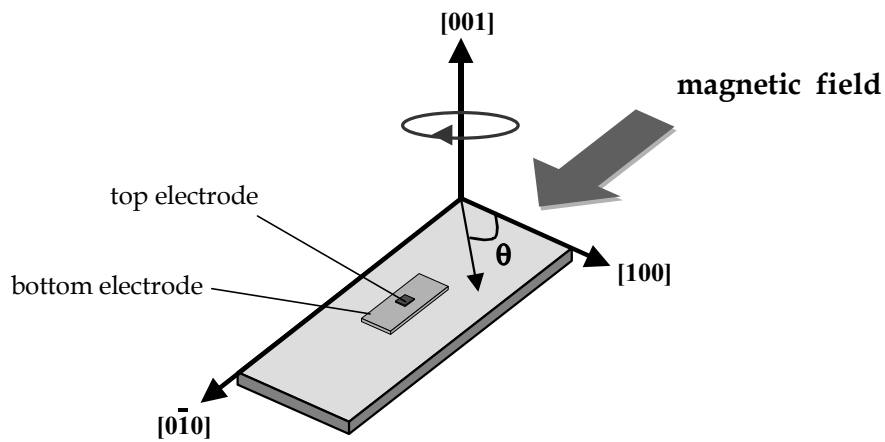


**Fig. 7.1.** The geometry of the two-dimensional angular measurement as described in the text. The crystallographic indices are written for the perovskite pseudocubic cell.

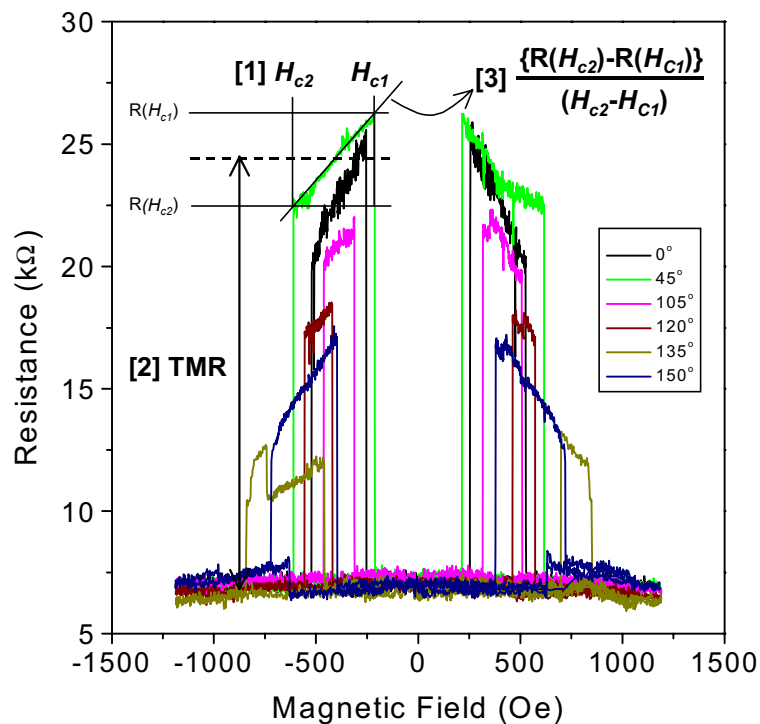


**Fig. 7.2.** Representative  $R_f$ - $H$  curves at various in-plane angles measured at 77K showing systematic variations of [1] the switching fields, [2] the tunnel magnetoresistance and [3] the slope of the top plateau as described in the text.

In Fig. 7.3, the variation of the switching fields for the top and the bottom electrodes were plotted as a function of the rotation angle. First one can see that the bottom electrode ( $50 \times 2000 \mu\text{m}$ ) exhibits an effective two-fold symmetry with a maximum switching field at around  $135^\circ$  and  $315^\circ$ . An independent magnetic anisotropy measurement of a plain LCMO films ( $1.5 \times 1.5 \text{mm}$ ) on NGO showed there to be uniaxial anisotropy with the  $[110]$  easy axis.<sup>8,9</sup> X-ray in-plane texture scans also confirmed that the  $[110]$  direction of the pseudocubic cell was aligned at  $135^\circ$  or  $315^\circ$  from the short edge of the sample (See Fig. 7.1). Therefore the maximum of the switching field at  $135^\circ$  and  $315^\circ$  can be explained by the intrinsic uniaxial crystalline anisotropy in the  $(001)$  plane of the bottom electrode. I note that the switching field of the bottom electrode oscillates with a offset field around  $300 \text{Oe}$ , for example even along the hard axis at  $45^\circ$  to  $[110]$  (or  $225^\circ$ ), the switching events are clearly observed as seen in Fig. 7.2. It signifies that the reversal process involves several other processes beyond coherent rotation alone.

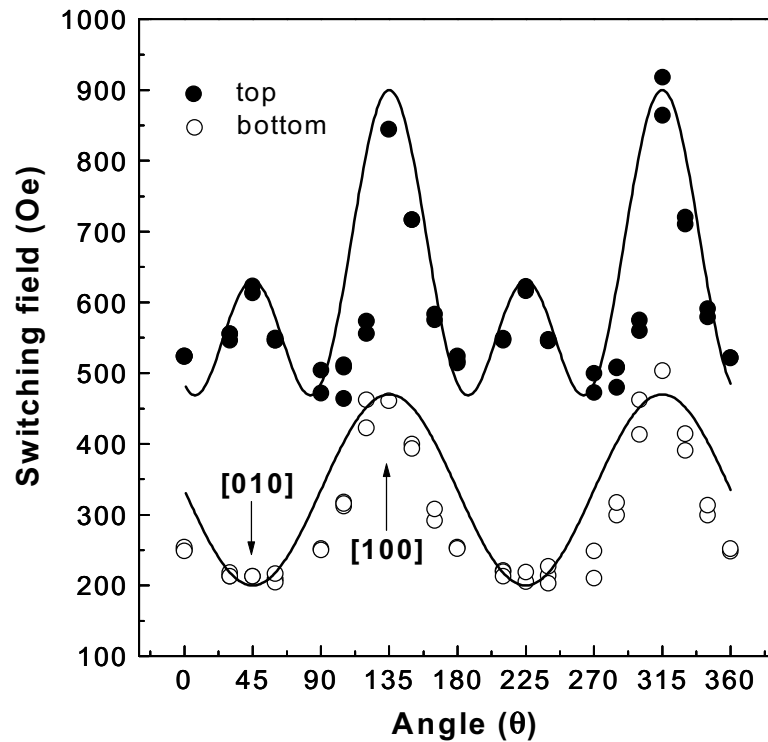
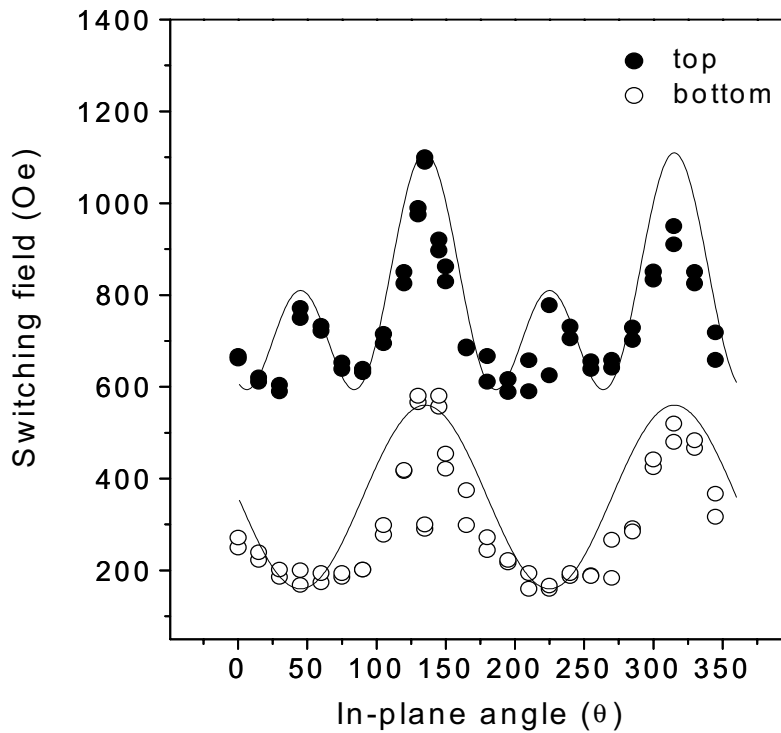


Fig. 7.3. The angular variation in the switching fields of the top and the bottom electrodes in the LCMO/NGO/LCMO junctions (measured at 77K). Solid sinusoidal oscillations show the effective two-fold symmetry,  $H_{c1} \sim K_{uni} \cdot \sin^2(\theta - \pi/4)$ , and the sum of the two- and four-fold symmetry,  $H_{c2} \sim K_{uni} \cdot \sin^2(\theta - \pi/4) + K_{bf}/4 \cdot \sin^2 2\theta$  for the bottom and the top electrode.

The angular dependence of the switching of the top ( $6 \times 6 \mu\text{m}$ ) electrode shows a sum of the two-fold and an additional four-fold symmetry component. The major two-fold orientation is the same as that in the bottom electrode, which indicates that the crystalline anisotropy still persists. The biaxial anisotropy is likely to be mainly due to the different size and shape of the top electrode. Maximum switching fields, and thus the easy axes, are found at  $45^\circ$ ,  $135^\circ$ ,  $225^\circ$  and  $315^\circ$  that correspond to the diagonal directions of the mesa square. Thus there is an effective biaxial symmetry.

The result of the same measurement on LCMO/La<sub>0.45</sub>Ca<sub>0.55</sub>MnO<sub>3</sub>/LCMO trilayer junctions is shown in Fig. 7.4, where the junction conductance is much lower due to inelastic tunnelling (Chapter 6). It shows the essentially same angular dependence as the junction shown in Fig. 7.3 and thus it can be assumed that the junction conductance does not affect magnetic reversal processes.



**Fig. 7.4.** The angular variation of the switching fields of the top and bottom electrodes in the LCMO/La<sub>0.45</sub>Ca<sub>0.55</sub>MnO<sub>3</sub>/LCMO junction. Solid sinusoidal oscillations show the effective two-fold symmetry  $H_{c1} \sim K_{umi} \sin^2(\theta - \pi/4)$ , and the sum of the two- and four-fold symmetry  $H_{c2} \sim K_{umi} \sin^2(\theta - \pi/4) + K_{bi}/4 \cdot \sin^2 2\theta$  for the bottom and the top electrodes.

Based on the symmetries observed above, the variations of the switching fields were fitted to simple second-order sinusoidal oscillations of  $H_{c1} \sim K_{uni} \cdot \sin^2(\theta - \pi/4)$  and  $H_{c2} \sim K_{uni} \cdot \sin^2(\theta - \pi/4) + (K_{bi}/4) \cdot \sin^2 2\theta$  for the bottom and top electrodes as in Fig. 7.3 and Fig. 7.4. I note that the fitted curve for the bottom electrode slightly deviates from the data. This indicates that the uniaxial anisotropy can be convoluted with a higher order transition, for example, higher order uniaxial terms are no longer negligible or the magnetization of the narrow and long bottom electrode is not uniform, resulting in a complex reversal process. I will concentrate on the switching of the top electrode for further discussion.

### 7.3 Coherent magnetization reversal processes

Coherent magnetization reversal of a small ferromagnetic object has been extensively studied for many years. Early theoretical work on the coherent switching of a single domain in the simplest uniaxial anisotropy case was performed by Stoner and Wohlfarth<sup>10</sup> and its geometrical expression in the two-dimensional plane formed by the two orthogonal easy and hard axes was proposed by Slonczewski as the so-called critical asteroid curve<sup>11</sup>. Further extended models in more complex anisotropy systems were explored by Thiaville.<sup>12</sup> Experimentally, the coherent rotation of mesoscopic ferromagnetic objects was recently studied with various techniques.<sup>13</sup> More recently the switching in exchange-biased metallic magnetic tunnel junctions of sub-micron size was studied with two orthogonal field measurements to investigate the coherent rotation.<sup>14,15</sup> Here in this study, I explored a possible coherent magnetic reversal of the top electrode (the  $6 \times 6 \mu\text{m}$  square mesa) with angular measurements by comparing with the ideal coherent rotation criteria as described below.

The uniform magnetization ( $\mathbf{M}$ ) of a small ferromagnet object under a magnetic field,  $\mathbf{H}$  is given as in Eq. [7.2]. If the switching of the top electrode satisfies the criterion of coherent rotation with a total second order anisotropy of

$$E_K(\theta) = -\{K_{uni} \cdot \sin^2(\theta - \frac{\pi}{4}) + \frac{K_{bi}}{4} \cdot \sin^2 2\theta\}, \quad [7.3]$$

Then Eq. (7.2) can be rewritten as

$$E_{\text{tot}}(\mathbf{H}) = -(H_{\parallel} M_s \cos\theta + H_{\perp} M_s \sin\theta) - \{K_{uni} \cdot \sin^2(\theta - \frac{\pi}{4}) + \frac{K_{bi}}{4} \cdot \sin^2 2\theta\}, \quad [7.4]$$

where  $H_{\parallel}$  and  $H_{\perp}$  are the parallel and perpendicular components of the field.

The switching event would occur at  $\partial E/\partial\theta = \partial^2 E/\partial\theta^2 = 0$ , which gives a solution of

$$\{H_{\parallel}(\theta), H_{\perp}(\theta)\}, \quad [7.5]$$

i.e. a modified asteroid curve. The measured switching fields ( $H$ ) of the junction at various in-plane angles were reduced into two orthogonal components  $H\cdot\cos\theta$  and  $H\cdot\sin\theta$ , and they were superimposed onto a solution of  $\{H_{\parallel}(\theta), H_{\perp}(\theta)\}$  as in Fig. 7.5. One can see that a set of ( $H_{\parallel}$ ,  $H_{\perp}$ ) with  $K_{uni}$  and  $K_{bi}$  are  $2.5\times 10^5$  erg/cm<sup>3</sup> and  $5\times 10^4$  erg/cm<sup>3</sup> can be reasonably fit to the actual switching of the top electrode. This strongly suggests that the magnetic reversal of the top electrode is mainly fulfilled by coherent rotation. This coherent reversal process can conversely justify the observed sharp switching of the present junctions.

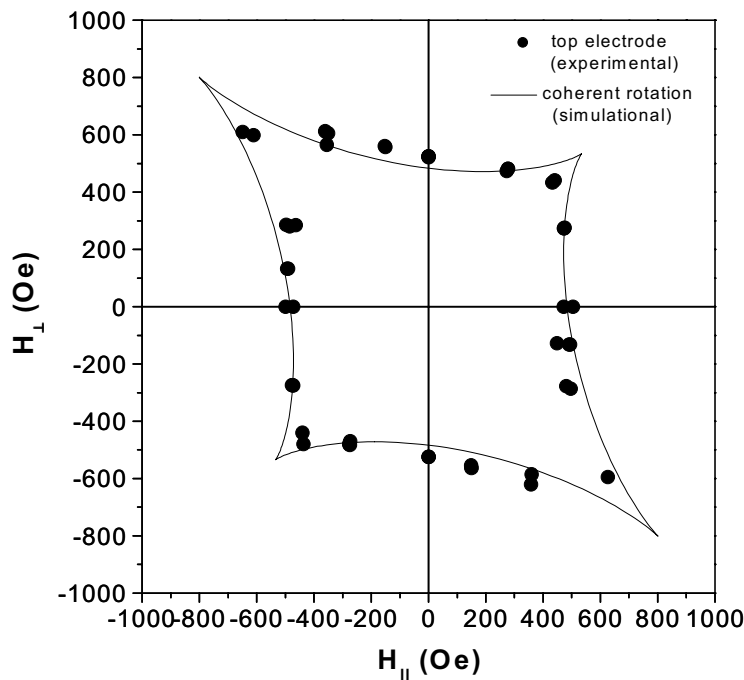


**Fig. 7.5.** The two-dimensional polar plot of the switching field of the top electrode in the ( $H_{\parallel}$ ,  $H_{\perp}$ ) plane. The solid curve is simulated for the coherent rotation model of a single domain with the symmetry given in Eq. [7.4].

Although the present junctions demonstrate that switching occurs mainly via coherent magnetic reversal, the question still remains whether it is essentially the switching of a single domain entity. The  $\text{La}_{0.65}\text{Ca}_{0.35}\text{MnO}_3$  film on  $\text{SrTiO}_3$  (where the film is tensile-stressed by  $\sim 1\%$  lattice-mismatch) showed a mean domain size of one micron or smaller,<sup>16</sup> which is rather

smaller than our junction mesas. The time-scale of the magnetization reversal in a soft magnet  $\text{Ni}_{60}\text{Fe}_{40}$  tunnel junctions is in the pico- or nano-second range<sup>17</sup> which is much shorter than that can be deduced from the field ramping rate maintained in our measurement.

## 7.4 Edge domains pinning effect

Following the angular dependent switching fields discussed above, I further looked into more detailed features on the magnetization reversal in Fig. 7.2. In Fig. 7.6, the angular variation of all three criteria, [1] the switching fields  $H_{c1}$  and  $H_{c2}$ , [2] the magnitude of TMR  $\Delta R/R^*_{high}$  and [3] the slope of the top plateau  $\{R(H_{c1}) - R(H_{c2})\}/(H_{c1} - H_{c2})$  are plotted together. Note that the slight deviation of sinusoidal oscillations from the experimental data is due to the order of anisotropy assumed for the fitting, thus it does not affect the major conclusions to be drawn. The variation of the TMR shown in Fig. 7.6(b) exhibits a rather complex angular dependence. It seems to be inversely dependent on the variation in the  $H_{c2}$ , i.e. the TMR is maximal when the switching of the bottom electrode occurs at the lowest field. It is also weakly related to  $H_{c1}$ . Thus it can be approximately fitted to  $-\{kH_{c1}(\theta) + lH_{c2}(\theta)\}$ , where  $k$  and  $l$  are constants for the fitting ( $k < l$ ). I note that this behavior is significantly different from the literature, where there is a simple  $\cos(\theta)$ -dependence.<sup>18</sup> In the magnetic reversal of a single domain of uniaxial anisotropy, an abrupt irreversible magnetization jump (as explicit in a square M-H loop) occurs when the field is applied along the easy axis, and results in the highest coercive field, while under the field applied along the hard axis the reversal occurs by a reversible continuous rotation showing no M-H hysteresis.<sup>10</sup> The observed angular dependence of the TMR, i.e. the minimum TMR at the highest coercivity indicates that the magnetic reversal process in the present junction is quite different from the free rotation of a single domain.

In magnetic tunnel junctions, there are several sources of magnetic coupling across the barrier between ferromagnetic layers in SPT junctions such as direct ferromagnetic coupling through pinholes in the barrier, dipolar interaction through the conformal roughness of the layers (Néel's "orange peel" coupling) and magnetostatic interaction.<sup>19</sup> It is noteworthy that among these possibilities only the magnetostatic origin can be angular-dependent. Another source of interlayer coupling, which can show angular dependence, is a quantum mechanical coupling between conduction electrons of different spin-angular momentums proposed by

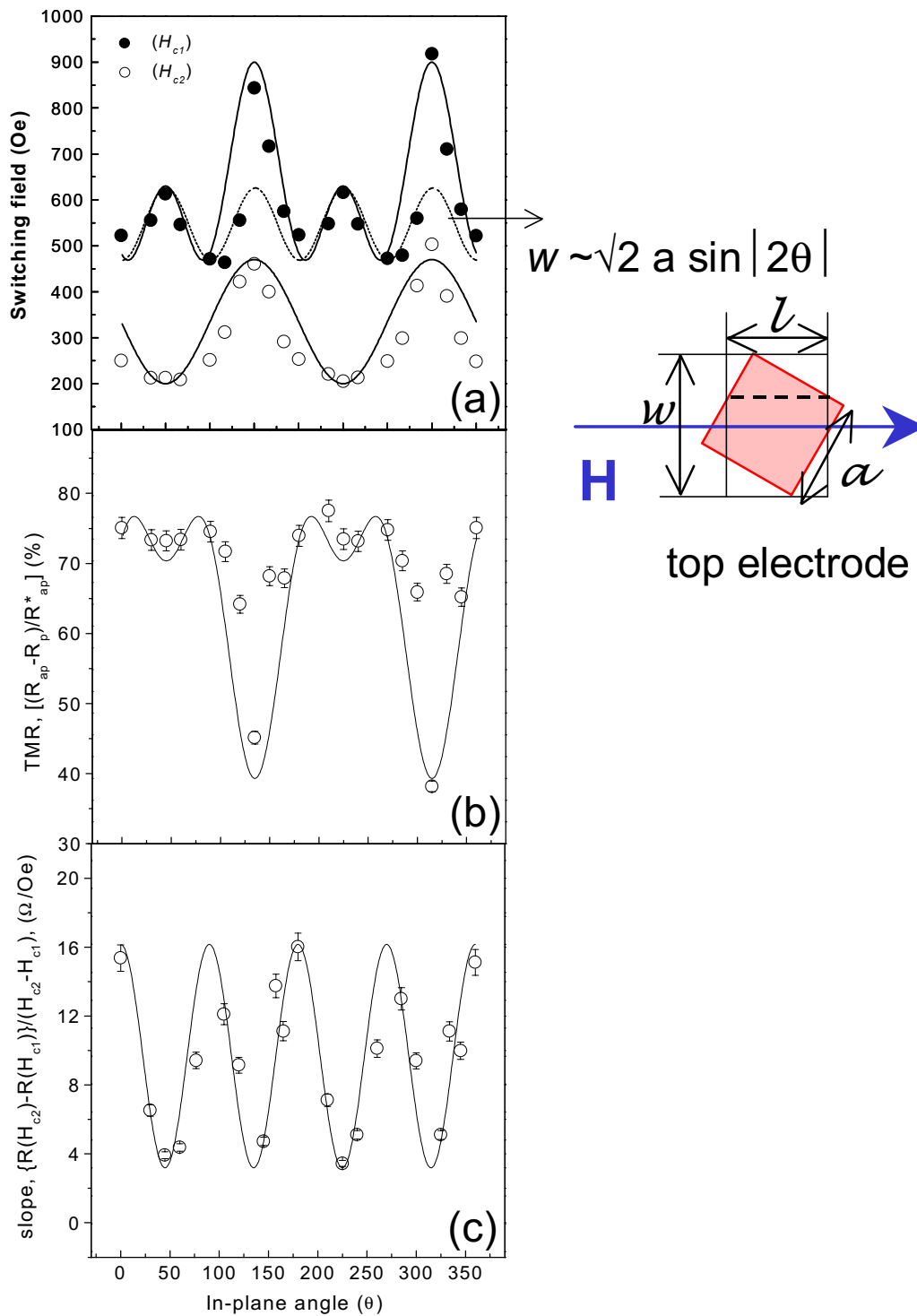


**Fig. 7.6.** The angular variation of (a) the junction switching fields, (b) the tunnel magnetoresistance and (c) the slope of the top plateau as defined in the Fig. 7.2.

Slonczewski.<sup>2</sup> However the calculated coupling field in the present junctions based on Slonczewski's proposal is several orders of magnitude too small. Thus it cannot explain the observed angular variation.

Then I focused on the magnetization reversal of the top electrode that seems to be intimately related to the variation of the TMR in terms of micromagnetics. It is first noted that the in-plane angular rotation establishes a different magnetic energy condition in the top electrode at each angle, for example at  $\theta = 0^\circ$  the effective shape of the top electrode with respect to the applied field direction (the shape of the top electrode projected onto the axis perpendicular to the field) is square (uniform  $l$ ), while it is rhombic at  $\theta = 45^\circ$  (non-uniform  $l$ ). The demagnetizing field ( $H_D$ ) for the square shape of the top electrode with an oblate ellipsoid approximation was calculated to be  $\sim 450\text{Oe}$ , which is an order lower than the actual observation and therefore it can be inferred that the shape anisotropy in the top electrode is not solely due to the internal demagnetization. In fact from further TMR measurements in which junction size and shape are varied, I have found that the switching field is weakly related to the length ( $l$ ) of the top electrodes (on which the  $H_D$  is strongly dependent) but strongly dependent on the width ( $w$ ) of the shape. Thus the origin of the four-fold shape anisotropy of the  $H_{c2}$  of Fig. 7.6(a) was inferred to be related to the angular dependence of the width  $w \sim \sqrt{2} a \sin|2\theta|$ .

The slope of the top plateau can be regarded as a degree of the reversal coherence, i.e. a partial parallel magnetization (a minor domain) in the top electrode during net anti-parallel alignment with that of the bottom electrode when  $H_{c1} < H < H_{c2}$ . The variation of the slope then reflects the evolution of such minor domains. Indeed the  $R_T$ - $H$  curve of a larger junction ( $8 \times 8 \mu\text{m}^2$ ) at a slower ramping rate showed typical Barkhausen steps as seen in Fig. 7.7, strongly suggesting a multiple domain process. Its angular variation is shown in Fig. 7.6(c), where it can be best fitted with  $\sim -\sqrt{2} a \sin|2\theta|$ , i.e. the negative of the functional form of  $w$ . The observation that the angular variation of the slope is proportional to  $-w$  indicates that the increase of  $w$  helps the reversal of the minor domains to be more coherent.

Overall, the observations discussed above suggest that the magnetization reversal process of the top electrode is not only governed by its own interaction with the external field such as crystalline anisotropy and demagnetization field, but is also coupled with other interactions. The strong dependences of the switching fields and the top-plateau slope on  $w$ , discussed above, suggest a possible role of the edge domains of the top electrodes. In fact, recent micromagnetic studies<sup>20,21,22</sup> on magnetic reversal of (sub-micron) patterned ferromagnet thin films revealed that trapped edge-domains due to edge-pinning effect are responsible for the reversal, i.e. the

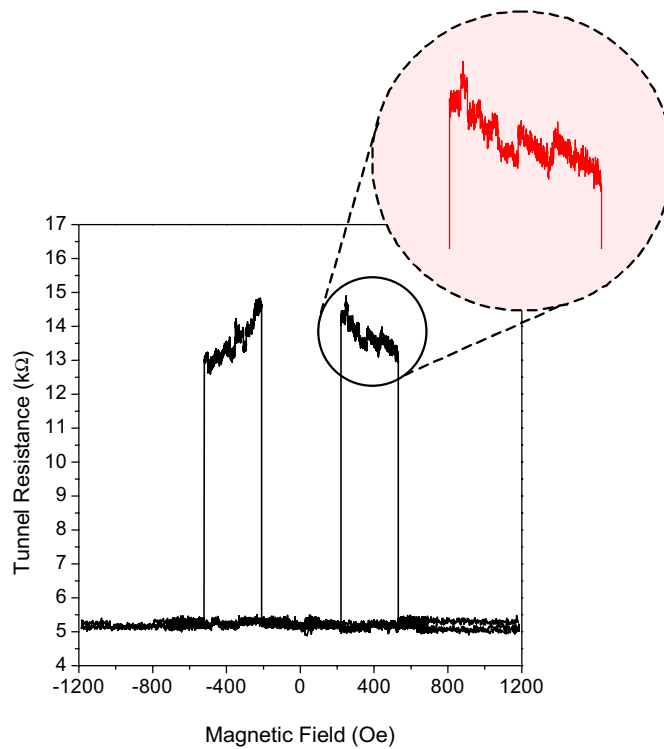


**Fig. 7.7.** Barkhausen steps in the spin polarised tunnelling conductance measured in the  $8 \times 8 \mu\text{m}^2$  mesa junction. Discrete steps are clearly seen in the net anti-parallel configuration.

switching involves de-pinning of the edge domains. Furthermore the switching field is found to be dependent on the effective shape of the sample edges, as similarly observed in this study, where this was attributed to different edge domain structures: an acicular element tends to be almost single domain due to micromagnetics and thus results in a higher switching field compare with a square shape that develops edge domain vortices.<sup>23</sup>

I will now propose a role of edge-domain pinning in the top electrodes for the observed magnetization reversal processes as described in Fig. 7.8 (Note that in the top electrode mesa fabrication stage, the ion milling usually leads to 10-20% of over-etching, thus partially penetrating the bottom electrode. Therefore the basal mesa that constitutes the bottom electrode is present beneath the top electrode). I first note that the magnetic structure of the top electrode is multi-domain and consists of major and minor domains, as discussed above. The minor domain structure is dependent on the orientation of the shape with respect to the applied field,

i.e. a square or a rhombus.<sup>23</sup> Nevertheless, from the fact that the major switching between the parallel and the anti-parallel resistances consistently occurs with a abrupt jump and only a minor variation of the slope of the top plateaus, the multi-domain break-up in the top electrodes must be very local, i.e. dominated from only at the edge of the top electrode. Then the amplitude of the pinning effect is proportional to effective width of the object, for example,  $w$  in Fig. 7.6.

At  $\theta = 45^\circ$  (or  $225^\circ$ ) the edge pinning ( $w = \sqrt{2} a$ ) is maximal and thus it can effectively pin the magnetization of the edge domains in the top electrode. It explains the (local) maximum  $H_{c2}$  and the lowest slope of the plateau as seen in Fig. 7.2. However, ironically, the inner domain can be broken up with the strongly pinned edge-domains, and then they can couple separately with the increasing reversed-field; at  $H_{c1}$  a part of the inner domain is already reversed and their magnetization is in parallel with the bottom electrode. Consequently there is a relatively lower TMR. Meanwhile at  $\theta = 0^\circ$  ( $90^\circ$ ,  $180^\circ$  and  $270^\circ$ ), the edge pinning is weakest ( $w = a$ ) and presumably the edge domain structure tends to be more complicated, i.e. edge vortices.<sup>23</sup> Thus the switching field is lower and the maximum slope is higher. Since the edge pinning is weak the reversal process can be much easily facilitated by domain wall motion without the significant coupling between the field and the inner domains. This results in a relatively higher TMR.

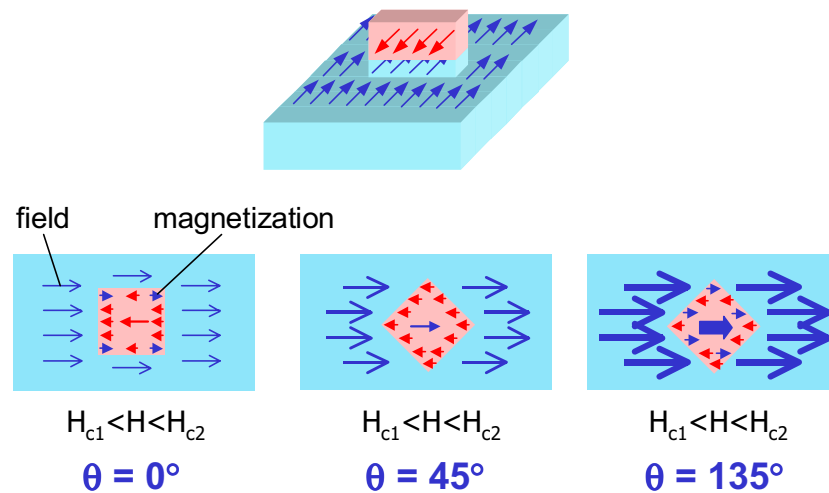


**Fig. 7.8.** Schematic representation of the edge domain pinning effect during magnetization reversal processes at various in-plane angles, as in this study. The widths of the arrows signify the strength of the external field or magnetization at anti-parallel configurations.

At  $\theta = 135^\circ$  (or  $315^\circ$ ) there is a peculiar behaviour, where the both easy axis in the crystalline anisotropy and the shape anisotropy (the edge pinning) coincide. This results in a maximum in both switching fields  $H_{c1}$  and  $H_{c2}$ , as seen in Fig. 7.6(a). At this angle the crystalline anisotropy that leads to  $H_{c1}$  is comparable to the edge pinning which can be roughly said to lead to  $\Delta(H_{c2}-H_{c1})$ . The overwhelmingly large external field required to overcome both anisotropies,  $H \geq \Delta(H_{c2}-H_{c1})$  can couple even with the edge domains as well as most of the inner domains and can reverse a significant part of the magnetization of the top electrode even before reaching the major switching field  $H_{c2}$ . As a result, the TMR will be strongly suppressed.

In summary, the origin of the magnetization reversal of the top electrode in this study can be understood as a combination of edge-domain pinning and the resultant multiple domain break-up. The measured TMR is then related to the coupling between the external field and the multiple domain structures, mediated by the edge pinning. The observed TMR was re-plotted in Fig. 7.9 as a function of the corresponding switching field taken from Fig. 7.2(a). It shows that

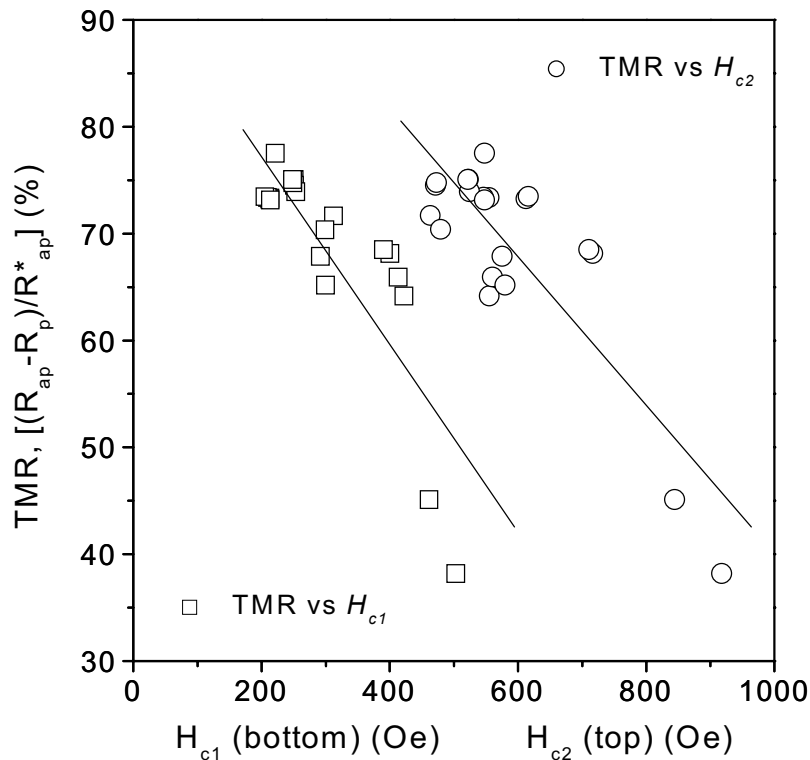


**Fig. 7.9.** The tunnelling magnetoresistance versus the corresponding switching fields of the top and the bottom electrodes measured in the two dimensional angular measurements. The solid lines are linearly fitted to the data.

---

the TMR decreases (roughly) linearly with increasing  $H_{c1}$  and  $H_{c2}$ . In the present junctions, the edge pinning effect in the top electrode due to the shape anisotropy increases the immobility of the edge domains. However at the same time, it also contributes to the multi-domain break-up between the edge-domains and the inner-domains, and their relative volume fractions. The TMR is largely dependent on the coupling between the external field and the major inner-domains that are in the majority at most of angles.

---

**REFERENCES**

- 
- <sup>1</sup> M. Jullière, *Phys. Lett. A* **54**, 225 (1975).
  - <sup>2</sup> J.C. Slonczewski, *Phys. Rev. B* **39**, 6995 (1989).
  - <sup>3</sup> For example, see X. Potier and A.K. Petford-Long, *Appl. Phys. Lett.* **76**, 754 (2000) and H. Arduin, J.N. Chapman, P.R. Aitchison, M.F. Gillies, K.J. Kirk and C.D.W. Wililson, *J. Appl. Phys.* **88**, 2760 (2000).
  - <sup>4</sup> C. Tiusan, T. Dimopoulos, K. Ounadjela, M. Hehn, H. A. M. van den Berg, V. da Costa and Y. Henry, *Phys. Rev. B.* **61**, 580 (2000).
  - <sup>5</sup> W.J. Gallagher, S.S.P. Parkin, Y. Lu, X.P. Bian, A.C. Marley, K.P. Roche, R.A. Altman, S. Rishton, C. Jahnes, T.M. Shaw and G. Xiao, *J. Appl. Phys.* **81**, 3741 (1997).
  - <sup>6</sup> M.-H. Jo, N.D. Mathur, N.K. Todd and M.G. Blamire, *Phys. Rev. B.* **61**, R14905 (2000).
  - <sup>7</sup> X.W. Wu, M.S. Rzechowski, H.S. Wang and Qi. Li, *Phys. Rev. B.* **61**, 501 (2000).
  - <sup>8</sup> N.D. Mathur, M.-H. Jo, J.E. Evetts and M.G. Blamire *J. Appl. Phys.* **89**, 338 (2001).
  - <sup>9</sup> K. Steenbeck and R. Hiergeist, *Appl. Phys. Lett.* **75**, 1778 (1999).
  - <sup>10</sup> E.C. Stoner and E.P. Wohlfarth, *Phil. Trans. Roy. Soc. A* **240**, 599 (1948).
  - <sup>11</sup> J.C. Slonczewski, Research Memo No. 003.111.224, IBM Research Center, Poughkeepsie, NY (1956) (unpublished).
  - <sup>12</sup> A. Thiaville, *J. Mag. Mag. Mater.* **182**, 5 (1999).
  - <sup>13</sup> O. Fruchart, J.-P. Nozieres, W. Werndorfer, D. Givord, F. Rousseaux and D. Decanini, *Phys. Rev. Lett.* **82**, 1305 (1999) and E. Bonet, W. Werndorfer, B. Babara, A. Benoit, D. Mailey and A. Thiaville, *Phys. Rev. Lett.* **83**, 4188 (1999).
  - <sup>14</sup> Y. Lu, P. L. Trouilloud, D.W. Abraham, R. Koch, J. Slonczewski, S. Brown, J. Bucchignano, E. O'Sullivan, R.A. Wanner, W.J. Gallagher and S.S.P. Parkin, *J. Appl. Phys.* **85**, 5267 (1999).
  - <sup>15</sup> A. Anguelouch, B. D. Schrag, Gang Xiao, Yu Lu, P. L. Trouilloud, R. A. Wanner, W. J. Gallagher, and S. S. P. Parkin, *Appl. Phys. Lett.* **76**, 622 (2000).
  - <sup>16</sup> Q. Lu, C.-C. Chen and A. de Lozanne, *Science* **276**, 2006 (1997).
  - <sup>17</sup> R.H. Koch, J.G. Deak, D.W. Abraham, P. L. Trouilloud, R.A. Altman, Yu Lu, W.J. Gallagher, R.E. Scheuerlin, K.P. Roche and S.S.P. Parkin, *Phys. Rev. Lett.* **81**, 4512 (1998).
  - <sup>18</sup> J.S. Moodera and L.R. Kinder, *J. Appl. Phys.* **79**, 4724 (1996).
  - <sup>19</sup> See, typical examples, C.L. Platt and M.R. McCartney, F.T. Parker and A.E. Berkowitz, *Phys. Rev. B* **61**, 9633 (2000) and L. Thomas, M.G. Samant and S.S.P. Parkin, *Phys. Rev. Lett.* **84**, 1816 (2000).
  - <sup>20</sup> J. Shi, S. Tehrani, T. Zhu, Y.F. Zheng and J.-G. Zhu, *Appl. Phys. Lett.* **74**, 2525 (1999).
-

- <sup>21</sup> A.F. Popkov, L.L. Savchenko, N.V. Vorotnikova, S. Tehrani and J. Shi, *Appl. Phys. Lett.* **77**, 277 (2000).
- <sup>22</sup> J. Shi and S. Tehrani, *Appl. Phys. Lett.* **77**, 1692 (2000).
- <sup>23</sup> K.J. Kirk, J.N. Chapman and C.D.W. Wilkinson, *Appl. Phys. Lett.* **71**, 539 (1997).

---

## CHAPTER 8

### Summary and Outlook

---

The most notable indicator of the potential applications of ferromagnets for magnetic tunnel junctions is the degree of electronic spin polarisation. In this dissertation I have described an experimental study on spin polarised tunnel (SPT) junctions based on a half-metallic manganite,  $\text{La}_{0.7}\text{Ca}_{0.3}\text{MnO}_3$  (LCMO).

The role of strain due to lattice-mismatch between LCMO thin films and substrates in the heteroepitaxial structures has been investigated and it suggested an inhomogeneous interfacial magnetic order, accompanied by three-dimensional islands growth. The coherent layer-by-layer growth of LCMO on lattice-matched  $\text{NdGaO}_3$  has been established and the grown LCMO films showed a weaker electron-lattice coupling.

The SPT devices incorporating the  $\text{NdGaO}_3$  barrier demonstrated the importance of high polarisation in magnetic tunnel junctions. It showed a very large tunnel magnetoresistance  $\{\text{TMR}, (\text{R}_{\text{ap}}-\text{R}_{\text{p}})/\text{R}_{\text{ap}}\}$  of 86% at 77K, and coherent switching. The electronic polarisation of the LCMO deduced from the TMR at 77K was 0.86 and this value is higher than the directly measured value at 4.2K. This study demonstrates that TMR in half-metallic systems can be qualitatively different in materials systems with optimized interfaces: using a better lattice-matched insulator, the TMR can be dramatically improved. I have proposed that phase separation at interfaces can provide an explanation for the rapid decay in the TMR in manganite tunnel junction. These results also raise the possibility of very high TMR in well-engineered half-metallic systems through the control over the scale and alignment of phase separated magnetic regions within devices.

A variety of the ground states in mixed valence manganites,  $\text{La}_{1-x}\text{Ca}_x\text{MnO}_3$  ( $0 < x < 1$ ) were exploited to construct an all-manganites SPT junction,  $\text{LCMO}/\text{La}_{0.45}\text{Ca}_{0.55}\text{MnO}_3/\text{LCMO}$ , where

---

the ground state of the  $\text{La}_{0.45}\text{Ca}_{0.55}\text{MnO}_3$  barrier is an antiferromagnetic insulator. It is found that the junction conductance is likely to be influenced by the potential coexistence of mesoscopic metallic and insulating phases in the  $\text{La}_{0.45}\text{Ca}_{0.55}\text{MnO}_3$ . Nevertheless the structural and chemical coherency and the exchange coupling at the LCMO/ $\text{La}_{0.45}\text{Ca}_{0.55}\text{MnO}_3$  interface serves to increase the stability of the interfacial ferromagnetic-order in the LCMO. Particularly this can qualitatively explain the improved temperature dependence of the TMR over the junctions with non-magnetic barriers.

I investigated magnetization reversal processes in the SPT junctions by two-dimensional angular SPT measurements. The highly sensitive TMR to local magnetic fluctuations in the LCMO in the resistance-field curves reveals important information about magnetization reversal. The large bottom electrode shows uniaxial crystalline anisotropy, and the top electrode shows a combination of the uniaxial crystalline anisotropy and biaxial shape anisotropy. The edge domain pinning is suggested to play a crucial role in the coherent magnetization reversal.

Although the very high TMR effects based on half-metallic manganites have been demonstrated in several recent studies, including this dissertation work, their practical applications at room temperature are by and large limited for several reasons. This is mainly due to the relatively low Curie temperatures ( $T_C$ ) of half-metallic manganites. There are several other half-metallic oxides with the relatively higher  $T_C$ , such as  $\text{Fe}_3\text{O}_4$ ,  $\text{CrO}_2$ ,  $\text{Sr}_2\text{FeMoO}_6$  and  $\text{Tl}_2\text{Mn}_2\text{O}_7$ . However reproducible TMR effects at room temperature have not been available yet. Recently the high MR effect at room temperature in magnetic oxides related to domain-wall scattering was demonstrated using nano-contacts in the break junctions; nevertheless the junction fabrications are not reproducible in a controllable manner.<sup>1</sup>

Another important issue that should be addressed on the performance of manganites junctions, particularly for low-frequency applications, can be a high noise level of manganites. In fact it is commonly observed in oxides-electronic devices: recent transport measurements on various magnetic oxides revealed a high level of  $1/f$  resistance, several orders of magnitude larger than the electrical noise typically observed in metallic films.<sup>2</sup> In manganites-based tunnel junctions, there may be additional sources of noises compared to metallic tunnel junctions<sup>3</sup> such as exceptionally large  $1/f$  noise from due to inhomogeneous (magnetic and polaronic) phase-fluctuation in manganites and mobile oxygen defects in oxide barriers.<sup>4</sup>

---

The intrinsic complexity of materials physics in mixed valence manganites as the result of intricate interplay among their electronic, magnetic and crystal structures also increases the complication of the spin-polarised transport study. Particularly in the heteroepitaxial tunnel junctions, the high sensitivity of the physical properties to local crystal structures, i.e. broken crystal-symmetry, strain and mesoscale phase-separation at interfaces, must be critical for tunnelling. It would be challenging to explore a possibility to manipulate such complexity of manganites by tuning a delicate balance in a controllable fashion. Interestingly, it was recently demonstrated that the multi-phase coexistence in manganite channels was exploited to give rise to an electric field-induced carrier-modulation through a ferroelectric gate.<sup>5</sup> A superior control of the junction fabrications, e.g. atomically flat interfaces with uniform chemical terminations or nano-patterning of the junction can address further important issues to be clarified. A further complete understanding of the manganite physics must be paralleled with the junction study.

Overall, the explicitly high spin-polarisation of conduction electrons in half-metallic manganites is very attractive for the fundamental study of spin transport: they can project the role as a spin-polarised electron source or detector beyond TMR effects. They can be utilized as spin-analyzers to probe the density of states at the Fermi level ( $E_F$ ) of other ferromagnets, e.g. the electronic polarisation.<sup>6,7</sup> Particularly, the common ground of the perovskite structure makes it feasible to incorporate manganites into the heteroepitaxial hybrid systems with other types of perovskite oxides such as high  $T_C$  superconductors and ferroelectric oxides. In the manganite/cuprates hybrids, the Cooper-pair breaking due to spin injection was investigated and the three-terminal devices based on the spin-injection can envisage a potential high-speed electronics.<sup>8</sup>

---

**REFERENCES**

- 
- <sup>1</sup> J.J. Verluijs, M.A. Bari and J.M.D. Coey, *Phys. Rev. Lett.* **87**, 026601 (2001).
- <sup>2</sup> B. Raquet, J.M.D. Coey, S. Wirth and S. von Molnar, *Phys. Rev. B* **59**, 12435 (1999) and the references therein.
- <sup>3</sup> S. Ingvarsson, Gang Xiao, S.S.P. Parkin, W.J. Gallagher, G. Grinstein and R.H. Koch, *Phys. Rev. Lett.* **85**, 3289 (2000).
- <sup>4</sup> P. Reutler, A. Bensaid, F. Herbstritt, and C. Höfener, A. Marx and R. Gross, *Phys. Rev. B* **62**, 11619 (2000) and the references therein.
- <sup>5</sup> T. Wu, S. B. Ogale, J. E. Garrison, B. Nagaraj, Z. Chen, R. L. Greene, R. Ramesh, T. Venkatesan and A.J. Millis, cond-mat/0001025.
- <sup>6</sup> J.M. De Teresa, A. Barthelemy, A. Fert, J.P. Contour, F. Montaigne and P. Seneor, *Science* **286**, 507 (1999).
- <sup>7</sup> D. C. Worledge and T. H. Geballe, *Phys. Rev. Lett.* **85**, 5182 (2000).
- <sup>8</sup> For example see, V.A. Vas'ko, V A. Larkin, P.A. Kraus, K.R. Nikolaev, D.E. Grupp, C.A. Nordman, and A.M. Goldman, *Phys. Rev. Lett.* **78**, 1134 (1997) and L. R. Tagirov, *Phys. Rev. Lett.* **83**, 2058 (1999).